University of Massachusetts Amherst

Self-Assembly of Block Copolymers by Solvent Vapor Annealing, Mechanism and Lithographic Applications

Item Type	dissertation
Authors	Gu, Xiaodan
DOI	10.7275/r957-fb71
Download date	2025-05-19 03:00:14
Link to Item	https://hdl.handle.net/20.500.14394/19941

SELF-ASSEMBLY OF BLOCK COPOLYMERS BY SOLVENT VAPOR ANNEALING, MECHANISM AND LITHOGRAPHIC APPLICATIONS

A Dissertation Presented

by

XIAODAN GU

Submitted to the Graduate School of the
University of Massachusetts Amherst in partial fulfillment
of the requirements for the degree of

DOCTOR OF PHILOSOPHY

February 2014

Polymer Science and Engineering

© Copyright by Xiaodan Gu 2014

All Rights Reserved

SELF-ASSEMBLY OF BLOCK COPOLYMERS BY SOLVENT VAPOR ANNEALING, MECHANISM AND LITHOGRAPHIC APPLICATIONS

A Dissertation Presented

by

XIAODAN GU

Approved as to style and content by:

_____
Thomas P. Russell, Chair

_____
Kenneth R. Carter, Member

_____
Mark Tuominen, Member

_____
David A. Hoagland, Department Head
Polymer Science and Engineering

DEDICATION

To my parents, Jianfei Gu and Caifeng Zhong.

ACKNOWLEDGMENTS

The work in this thesis was not possible without the efforts from my collaborators and coworkers.

First, my thesis advisor Prof. Thomas P. Russell deserves the credits for directing my research project, funding my work, and providing me collaboration resources through out my Ph.D. degree. Tom, as a pioneer in block copolymer self-assembly, showed me the beauty of the molecular self-assembly. Numerous times, Tom stimulates my interested in the polymer physics, provides me invaluable guidance, and nudges me in the right direction.

I also want to thank Prof. Mark Tuominen and Prof. Kenneth R. Carter to serve on my thesis committee and provide me valuable suggestions on the research proposal and thesis writing.

I also want to acknowledge my collaborators, especially Dr. Deirdre Olynick in the Molecular Foundry at Lawrence Berkeley National Lab (LBNL) and Paul Dorsey at Western Digital Inc. Deirdre's expertise in the plasma etching greatly facilitates the projects related to block copolymer lithography. Dr. Paul Dorsey, my supervisor at the Western Digital, gives me unique experiences to work at corporative environments and carry out cutting edge research projects.

I also want to thank all of the members in the Russell group for their assistance not only in lab but also in life during my stay in Amherst. I enjoyed working together with them for the past five years. I own a lot to the helps I received from the BCP self-assembly research team members, including Dr. Soojin Park, Dr. Donghyun Lee, Dr. Sungwoo Hong, Dr. Bokyung Kim, Dr. Yunxia Hu, Dr. Wei Chen, Dr. Ji Xu, Dr. Wei

Zhao, Dr. Weiyin Gu, Dr. Ilja Gunkel, Zhiwei Sun, Gajin Jeong. Especially, I want to thank Sungwoo and Ilja, both who I have been closely interacted with. Sungwoo, a very hard working person, is a role model for me to start my research career. Working with Ilja is an amazing thing in my Ph.D. Lots of research ideas were spackled from our lunch discussion at ALS. He made my stay in ALS not boring. I also own a lot for the assistances I received from Laurie Banes, who helped me with purchases of chemicals.

I would also like to thank Advanced Light Source at LBNL for providing the doctoral fellowship to me, and allow me to perform experiments using state-of-art synchrotron facility. Especially, thanks Dr. Alexander Hexemer to host me as a student researcher at the Advanced Light Source at LBNL in beamline 7.3.3 for the past years. His knowledge in X-ray science is very beneficial for the projects. He also showed me how to balance work and family and I enjoyed the BBQ parties in his house.

This project would have gone nowhere real fast without the assistance from the 7.3.3 and 11.0.1.2 staffs at the Advanced Light Source and Nano-fabrication facility in the Molecular Foundry in the LBNL. Thanks to Eric Schabile, who received my phone calls at midnight to ask for help on instrumental problems. I appreciate the help from beamline associates Steven Alvarez, Eumhee Lin, Polite Staward, Dr. Elaine Chan. I appreciate Dr. Cheng Wang's sincere help on the soft X-ray measurements and suggestions on project and career plan. I also would like to thanks knowledgeable and helpful staffs at the Molecular Foundry. The supports I received from Dr. Stefano Cabrini, Bruce Harteneck, Erin Wood, Dr. Scott Dhuey, Dr. Adam Schwartzberg, Dr. Zuwei Liu are very important for the block copolymer lithgraphy project.

I am proud and honored to stay at the world-renowned department of Polymer

Science and Engineering at University of Massachusetts at Amherst. I must express my thankfulness to the entire faculties, who curate the next generation polymer scientist, staffs, who keeps the department running smoothly, and 2008 PSE classmates, whom made my life in Amherst very entertaining.

At last, I am grateful to my family and friends for their supports throughout my study. Finally, thanks to Yuanyuan, your encouragement to me on my career and life. I am extremely lucky to meet you and have you in my life.

ABSTRACT

SELF-ASSEMBLY OF BLOCK COPOLYMERS BY SOLVENT VAPOR ANNEALING, MECHANISM AND LITHOGRAPHIC APPLICATIONS

FEBRUARY 2014

XIAODAN GU

B.S., NANJING UNIVERSITY

M.S., UNIVERSITY OF MASSACHUSETTS AMHERST

Ph.D., UNIVERSITY OF MASSACHUSETTS AMHERST

Directed by: Professor THOMAS P. RUSSELL

Block copolymers (BCP) are a unique class of polymers, which can self-assemble into ordered microdomains with sizes from 3 nm to about 50 nm making BCPs an appealing meso-scale material. In thin films, arrays of BCP microdomains with long-range lateral order can serve as ideal templates or scaffolds for patterning nano-scale functional materials and synthesizing nanostructured materials with size scales that exceed the reach of photolithography. Among many annealing methods, solvent vapor annealing (SVA) is a low-cost, highly efficient way to annihilate defects in BCP thin films and facilitates the formation of highly ordered microdomains within minutes. Directing the self-assembly of BCPs could, in principle, lead to the formation of domains with near perfect lateral ordering. The mechanism of SVA of BCPs, however, is still ill-understood, albeit it has been widely adopted in research laboratories around the world

for the past decade.

In the first part of this thesis, the ordering process of BCP thin films during annealing in neutral solvents was investigated mainly by *in situ* synchrotron X-ray scattering. Briefly, the solvent molecules impart mobility to the BCP and enable a marked improvement in the lateral ordering of the BCP microdomains. Both, BCP concentration in the swollen film and the rate of solvent removal play a key role in obtaining films with well-ordered microdomains. The amount of swelling in a BCP thin film during SVA depends on the chemical nature of the blocks, the quality of the solvent, and the molecular weight of the BCP. A high degree of swelling - still low enough to prevent solvent-induced mixing (disordering) of BCP microdomains,- provides a high chain mobility, and thus results in the formation of arrays of ordered microdomains with large grain sizes after SVA in neutral solvents.

The rate of solvent removal is another critical parameter for obtaining long-range lateral order in BCP thin films after SVA in neutral solvents. While in the swollen state ordered structures form with exceptional order, removal of the solvent results in a deterioration of order due to the confinement imposed to a BCP in a thin film by the rigid silicon substrate. It was found, however, that an instantaneous solvent removal can minimize disordering to preserve the order formed in the swollen state.

Self-assembled BCP microdomains also serve as ideal template to pattern other materials with exceptional lateral resolution. In this thesis, two examples of BCP lithography was also demonstrated. A reconstruction process was used to enhance the etch contrast between two organic blocks. In one example, a BCP pattern was transferred to a silicon substrate to form high aspect ratio, 5:1, sub-10nm silicon lines or holes with

high fidelity. While in a second example, I demonstrated the fabrication of silicon oxide dots with an areal density as high as 2 Tera dots per $inch^2$ by BCP templates, which has the potential to serve as etch mask for bit pattern media applications.

TABLE OF CONTENTS

Page

ACKNOWLEDGMENTS v

ABSTRACT..... viii

LIST OF TABLES..... xiv

LIST OF FIGURES xv

LIST OF SCHEMATICS.....xx

CHAPTER

1. BACKGROUND 1

1.1. Overview.....1
1.2. Introduction to block copolymers 2
1.3. Block copolymer thin film 5
1.4. Thermal annealing and solvent vapor annealing 11
1.5. Lithographic applications by BCP self-assembly 15
1.6. References.....20

2. IN SITU X-RAY SCATTERING INVESTIGATION OF BCP SELF-ASSEMBLY DURING THE PROCESS OF SOLVENT VAPOR ANNEALING 24

2.1. Introduction.....24
2.2. Experimental 29

2.2.1. Materials and sample preparation 29
2.2.2. Custom built solvent vapor annealing chamber.....31
2.2.3. Grazing incidence small angle X-ray scattering 32
2.2.4. Film thickness measurements by optical interferometry 34
2.2.5. Surface morphology characterization 34
2.2.6. Molecular weight characterization by GPC 35

2.3. Results and discussion 35

2.3.1. SVA of BCP thin films: the swelling process.....35
2.3.2. SVA of BCP thin films: the process of solvent removal 44
2.3.3. SVA of BCP thin films: the influence of the processing history.. 49
2.3.4. SVA of BCP thin films: the influence of molecular weights.....59

2.3.5. SVA of BCP thin films: comparison of SVA with thermal annealing 69
2.3.6. SVA of BCP thin films: grain size at different swell ratio 75

2.4. Conclusions 78
2.5. References 79

3. PATTERN TRANSFER FROM SELF-ASSEMBLED BLOCK COPOLYMER MICRODOMAINS TO SILICON WITH SUB-10NM RESOLUTION 83

3.1. Introduction 83
3.2. Experimental 86

3.2.1. Materials 86
3.2.2. Sample preparation 87
3.2.3. Characterization 87
3.2.4. Simulation of 2D scattering pattern Si trench pattern 88

3.3. Results and discussion 88

3.3.1. Self-assembly of etch mask from BCP 88
3.3.2. Pattern transfer from BCP mask to silicon- trench pattern 93
3.3.3. Pattern transfer from BCP mask to silicon- hole pattern 99
3.3.4. Nano-imprint using silicon mold 101

3.4. Conclusions 102
3.5. References 103

4. SELF-ASSEMBLED BCP MICRODOMAINS FOR BIT PATTERNED MEDIA APPLICATIONS 105

4.1. Introduction 105
4.2. Experimental 107

4.2.1. Materials and sample preparation 107
4.2.2. Etching mask preparation 108
4.2.3. Characterization 108

4.3. Results and discussion 109

4.3.1. Porous BCP template fabrication 109
4.3.2. Silicon oxides pillar etch mask fabrication 112
4.3.3. Pattern transfer from silicon oxide pillars to carbon layer 120

4.4. Conclusions 122
4.5. References 122

5. FUTURE DIRECTIONS 124

5.1. Future directions 124
5.2. References.....126

BIBLIOGRAPHY.....128

LIST OF TABLES

Table Page

1.1 Chemical structure of various block copolymers 19

1.2 Flory-Huggins parameter for different block copolymers 20

2.1 List of BCPs with different molecular weights used in this study 30

2.2 Different process histories for BCP PS-*b*-P2VP 34k 50

2.3 SR and domain spacing at the order-disorder transition (ODT), and domain spacing at dry state for PS-*b*-P2VP BCPs with different molecular weights..... 62

2.4 Number-average (Mn) and weight-average (Mw) molecular weights of PS-*b*-P2VP..... 63

4.1 Area density information of silicon oxide pillars 116

4.2 Height information of silicon oxide pillars for different etch times..... 120

LIST OF FIGURES

Figure Page

1.1 Phase diagram of a diblock copolymer, calculated using self-consistent mean field theory. Regions of stability of disordered (dis), lamellar (lam), gyroid (gyr), hexagonal (hex) and body-centered cubic (BCC) phases are indicated. Adapted from [10]. 4

1.2 Balance the surface interaction between PS and PMMA on PS-r-PMMA neutral layer. (A) interfacial energies γ_{Sf} and γ_{Mf} and (B) $\Delta\gamma(f)= \gamma_{Mf} - \gamma_{Sf}$ for PS (cycle) and PMMA (triangles) on PS-r-PMMA brush as a function of f. Adapted from [17]. 7

1.3 Different ways to control the lateral ordering of BCPs using directed self-assembly. (a) Graphoepitaxy (b) Chemical pattern (c) Self-assembled saw-tooth substrate (e) e-beam lithography assisted patterning. Adapted from reference [23-26] 9

1.4 Two different set-ups of the solvent vapor-annealing chamber (a) closed jar annealing. (b) Carrying gas assisted solvent delivery annealing. 13

1.5 (a) Schematic of the pattern-transfer process from PS-*b*-PB to a silicon nitride substrate. (b,d) Self-assembly BCP microdomain, (c,e) patterned silicon nitride nanostructures after pattern transfer. Adapted from reference [42]. 16

2.1 Typical scattering profile (open spheres) in qy direction along with the corresponding fit (solid red line) to equation (2.1) 33

2.2 GISAXS scattering patterns of a swollen BCP film at different times. The indicated volume ratio corresponds to the swelling ratio as determined from the increase of film thickness during annealing. 36

2.3 Predicted values for the glass transition temperature of PS-*b*-P2VP block copolymers swelled by different amounts of THF according to the Flory-Fox equation 2.2 37

2.4 *In situ* GISAXS measurement of an as spun PS-*b*-P2VP film during solvent vapor Annealing in THF. Domain spacing (filled triangle), FWHM (filled circle), film thickness (solid line) vs. annealing time. 38

2.5 Ln of domain spacing of BCP in figure 2.4 as a function of ln of volume fraction polymer in the swollen film as calculated from the film thickness data shown in Figure 2.4. 39

2.6 Comparison between experimental data, (a), (e), and simulated 2D GISAXS patterns of the first order reflection (b-d),(f-h). (a)-(d) correspond to the swollen state and (e)-(h) to the films after solvent removal. 42

2.7 Results of *in situ* GISAXS experiments during SVA of BCP samples at three different solvent removal rates. Domain spacing, FWHM, film thickness (solid lines) vs. annealing time. The filled symbols correspond to the swelling, whereas the open symbols correspond to the solvent removal..... 44

2.8 Domain spacing of PS-*b*-P2VP as a function of the volume fraction of the BCP in the swollen film for different solvent removal rates. The filled symbols correspond to the swelling, whereas the open symbols correspond to the solvent removal. 46

2.9 SFM Phase images of BCP thin films after SVA. (a) rapid solvent removal corresponding to t_5 in Figure 2.8, (b) nitrogen flow rate of 49.2 sccm (5 nm/min) corresponding to t_5' in Figure 2.8 and (c) nitrogen flow rate of 11.0 sccm (1 nm/min) corresponding to t_5'' in Figure 2.8..... 47

2.10 OM of 45nm thin film PS-*b*-P2VP annealed in THF with SR 1.5 for 1h..... 49

2.11 SFM Step height measurement of the islands formed by solvent vapor annealing. 49

2.12 SFM images of samples with different processing history. Sample PH-1, before *in situ* experiment (a) and after *in situ* experiment (b). Sample PH-2, before *in situ* experiment (c) and after *in situ* experiment (d). Sample PH-3, before *in situ* experiment (e) and after *in situ* experiment (f). 52

2.13 Scattering profiles of PS-*b*-P2VP with different processing history before and after SVA in THF. 53

2.14 Temporal evolution of the in-plane scattering profiles for sample PH-1 (a), PH-2 (b), and PH-3(c). Data at different times were shifted vertically for clarity. 54

2.15 Results of *in situ* GISAXS experiments during SVA of BCP samples with different processing histories. Domain spacing, FWHM, and film thickness plotted vs. annealing time. (a) Sample PH-1, (b) Sample PH-2 (c) Sample PH-3 (d) All three samples plotted together. 55

2.16 ln of domain spacing of as a function of the ln of the volume fraction of the BCP for different processing histories. (a) PH-1 as-spun film, (b) PH-2 SVA annealed with instantaneous solvent removal, (c), PH-3 SVA annealed with slowly solvent removal, (d) all samples plotted together. All the swelling data points are represented by open symbols, while the deswelling data are shown as solid symbols. 57

2.17 Domain spacing of PS-*b*-P2VP BCPs of different molecular weight vs. swelling ratio (polymer concentration) during annealing in THF. The data correspond to the deswelling with all BCPs being in the ordered state (corresponding to a cylindrical morphology in all cases)..... 61

2.18 (a) ln-ln plot of the BCP concentration ϕ at ODT vs. the degree of polymerization N (Mw measured by GPC), and ln-ln plot of the BCP concentration ϕ at ODT vs. domain spacing D of the BCP. 64

2.19 ln-ln plot of domain spacing vs. the repeating unite of the BCP thin film 65

2.20 (a~e) 2-D X-ray scattering patterns of PS-*b*-P2VP 115k thin film with respect to different solvent vapor annealing time. (f) 1-D scattering profile of the BCP during the OOT..... 67

2.21 SEM images of the PS-*b*-P2VP 115k before OOT (a) and after OOT (b). 68

2.22 Representative 2-D scattering profile of the BCP during the *in situ* scattering experiment. 70

2.23 (a) Scattering profiles at different times. (B) analyzed data from the data shown in (a), temperature, domain spacing, and FWHM were plotted as a function of time. 71

2.24 SEM images of PS-*b*-P2VP thermally annealed at different temperatures. (a) PS-*b*-P2VP 34k and (c) PS-*b*-P2VP 58k annealed at 190deg for 1 hour. (b) PS-*b*-P2VP 34k and (d) PS-*b*-P2VP 58k annealed at 250deg for 1 hour. 73

2.25 (a) Flory-Huggins parameter at different temperatures during thermal annealing of PS-*b*-P2VP (based on equation 2.3) (b) Effective Flory-Huggins parameter of PS-*b*-P2VP swelled at different SR in a neutral sovlent during solvent vapor annealing (based on equation 2.4, and β is taken as 1.5) (c) plot of annealing temperature and SR at the same effective Flory-Huggins parameter 75

2.26 Colorized grains in the BCP microdomain structure for different swelling ratios: (a) 1.3, (b) 1.5, (c) 1.7 and (d) 1.7 (enlarged). Color wheel is shown at bottom of image. 76

3.1 Surface topography of PS-*b*-P2VP 58k during the different stage of solvent annealing and RIE. (a) SFM height images of the surface topography after different times of annealing in THF vapor, as spun (a-1), 20 min (a-2), 40 min (a-3), 60 min (a-4), 120 min (a-5), 180 min (a-6). All films were reconstructed in ethanol for 30 min before SFM imaging. Scale bars correspond to 250nm. (b) SEM images of the BCP film surface morphology after RIE at different etching times following solvent annealing and reconstruction: 0 sec (b-1), 10 sec (b-2), 15 sec (b-3), 20 sec (b-4), 25 sec (b-5), 30 sec (b-6) of etching in O_2 and Ar. Plot of the film thickness and the BCP line width, resp., versus the etching time (c).. 91

3.2 SEM images of thin film surface before, (a) plane-view (c) 60 degree tilt view, and after 15 sec of cryo ICP etching (b) plane-view (d) 60 degree tilt view. *Inset* image in (d) is a zoomed in image. (e, h) are 2D GISAXS patterns of silicon nanotrenches. Experimental data are shown in (e,f,g) and simulated data in (h,i,j). (f,i) are intensity plot with repect to peak position in-plane. (g,j) are intensity plot with repect to peak position out-of-plane 95

3.3 SEM images of silicon nano-trenches with a pitch of 27nm patterned from PS-*b*-P2VP (Mn= 23,600-*b*-10,400 kg/mol). (a) plane-view (b) 60 degree tilted cross-sectional view. *Inset* image in (d) is a zoomed in image. 96

3.4 SEM images of a PS-*b*-P2VP (40,000-*b*-18,000 kg/mol) pattern DSA by the trench pattern, and its pattern transfer into silicon. (a) illustration of the trench pattern. (b) illustration of the film thinning effect close to the edge of mesa. (c) PS-*b*-P2VP on a patterned substrate after solvent annealing and susbsequent reconstruction, (d) PS-*b*-P2VP on a patterned substrate after solvent annealing, reconstruction and etching. (e), (f) silicon nano-trenches after the pattern transfer..... 98

3.5 SEM images of a PS-*b*-PEO forming cylindrical domains oriented normal to the substrate. SEM was taken at a 60 degree tilt angle (a) block copolymer pattern after solvent annealing and subsequent reconstruction in ethanol, (b) the film after an additional etching of 10 s in RIE (c) transferred pattern in silicon after 10 s of cryo-ICP etching using the BCP mask (d) silicon pattern after 20 s of cryo-ICP etching. *Inset* image in (d) is the plane view of the silicon nano-hole pattern..... 100

3.6 SEM images of a PS resist after thermal imprinting using silicon fin as mold. (a) mold without treated with anti-sticking layer, (b) after the mold treated with FAS anti-sticking layer. 101

3.7 SFM images of P3HT after thermal imprinting using silicon fin as a mold. (a) height image, (b) phase image. Scale bar 1um. 102

4.1 SEM image of PS-*b*-P4VP 24k polymer template with different amount of oxygen/argon plasma etching, all of these etching are at 75W. a) 0 seconds etching, b) 10 seconds etching, c) 20 seconds etching, d) 30 seconds etching. Inserted cartoon is cross section view of the pore pattern, e) plot of film thickness with reactive ion etching time. 111

4.2 SEM image silicon pillar from PS-*b*-P4VP 24k with different amount of Ar/O_2 plasma etching time. a) and e) 0 seconds etching. b) and e) 10 seconds etching. c) and f)20 seconds etching. The first row is high magnification. The lower row is low magnification. 113

4.3 Cross section SEM image of silicon pillar from PS-*b*-P4VP 24k. a) low magnification of 75 degree tilted view. b) high magnification of 75 degree tilted view. c) low magnification of 90 degree tilted view. d) high magnification of 90 degree tilted view 113

4.4 The SFM height image of block copolymer porous template. a) reconstructed surface of PS-*b*-P2VP 77k. b) reconstructed surface of PS-*b*-P4VP 24K. c) reconstructed surface of PS-*b*-P2VP 20K. d) reconstructed surface of PS-*b*-P4VP 15K..... 115

4.5 The SEM image of block copolymer porous template. a) Reconstructed surface of PS-*b*-P2VP 77k, b) reconstructed surface of PS-*b*-P4VP 24k, c) reconstructed surface of PS-*b*-P2VP 20K, d) reconstructed surface of PS-*b*-P4VP 15K 116

4.6 The SFM height image of silicon pillar from block copolymer template. a) silicon pillar from PS-*b*-P2VP 77k template, b) silicon pillar from PS-*b*-P4VP 24k template, c) silicon pillar from PS-*b*-P2VP 20K template, d) silicon pillar from PS-*b*-P4VP 15K template..... 118

4.7 The SEM height image of silicon pillar from block copolymer porous template. a) silicon pillar from PS-*b*-P2VP 77k template, b) silicon pillar from PS-*b*-P4VP 24k template, c) silicon pillar from PS-*b*-P2VP 20K template, d) silicon pillar from PS-*b*-P4VP 15K template. 119

4.8 SEM cross section of Silicon pillar on media substrate with different amount of etching time. a) and d) after 20 seconds oxygen plasma etching. b) and e) after 40 seconds oxygen plasma etching. c) and f) after 70 seconds oxygen plasma etching. a) b) and c) samples are tilted for 75 degree. d), e), and f) samples are tilted for 90 degree. Inserted images schematic drawing of those pillar patterns..... 120

4.9 a)SFM height image of gold pillar made from porous block copolymer template, b) SFM height image, c) SEM image of Pt pillar made from porous block copolymer template 121

LIST OF SCHEMATICS

Schematic Page

2.1 *In situ* X-ray scattering experiment set-up. 31

3.1 Schematic diagram for self-assembled PS-*b*-P2VP thin film patterning of silicon nano-trenches (a) PS-*b*-P2VP spin coated on silicon wafer (b) microphase separated PS-*b*-P2VP film after solvent annealing (c) BCP film after reconstruction in ethanol to enhance the etching contrast between PS and P2VP domains (d) polymer pattern after etching the BCP film by means of RIE (e) silicon trenches after cryo-ICP etching using the polymer mask 88

4.1 Schematic procedure to make size tunable silicon oxide pillar by using block copolymer template 109

CHAPTER 1

BACKGROUND

1.1. Overview

Block copolymers (BCP) are a unique class of polymers, which can self-assemble into ordered microdomains with its sizes from 3 nm to about 50 nm making BCPs an appealing meso-scale material. In thin films, arrays of BCP microdomains with long-range lateral order can serve as ideal templates or scaffolds for patterning nano-scale functional materials and synthesizing nanostructured materials with size scales that exceed the reach of photolithography. Among many annealing methods, solvent vapor annealing (SVA) is a low-cost, highly efficient way to annihilate defects in BCP thin films and facilitates the formation of highly ordered microdomains within minutes. Directing the self-assembly of BCPs could, in principle, lead to the formation of domains with near perfect lateral ordering. The mechanism of SVA of BCPs, however, is still ill-understood, albeit it has been widely adopted in research laboratories around the world for the past decade.

I therefore tried to address this fundamental question of what is the mechanism of SVA, and also demonstrate lithography applications using BCP self-assembly. In the work presented here, I will introduce background information including: BCP, polymer thin film, solvent vapor annealing and lithography patterning techniques in the first chapter of this thesis. The second chapter focuses on investigation of the SVA process of BCP thin film using the real time *in situ* grazing incidence small angle X-ray scattering (GISAXS) and microscopy techniques. Several key parameters affecting the final

morphology of the annealed BCP sample will be identified and discussed. In the third chapter, I will use BCP lithography to pattern high resolution, high aspect ratio silicon nanostructures over large area. In chapter 4, the block copolymer lithography will be also implicated for bit pattern media application in the hard drive storage industry. The final chapter will point to some future directions regarding the research projects presented here,

1.2. Introduction to block copolymers

BCPs are a unique class of soft-materials well-known for their ability to self-assemble into well-ordered nanometer scale microdomains[1,2]. The BCPs consist of two chemically distinct polymers that are covalently linked at one end. Non-favorable segmental interactions, coupled with the inherent entropic loss due to the long-chain nature of the BCP, cause a separation of the blocks into domains where the size of the domains is dictated by the molecular weight of the BCP chain and the shape of the domain, be it spherical, cylindrical, gyroid or lamellar, is dictated, primarily, by the volume fraction of the components. Since the polymer chains are covalently bonded together at one end, the size scale of the domains must be commensurate with the size of the polymer chain, typically on the tens of nanometer length scale or less.

The theory of BCP self-assembly is well-developed and successfully predicts the phase diagram of the equilibrium morphology of BCP bulk melts, as shown in Figure 1.1, where χ is the Flory-Huggins segmental interaction parameter, N is the total number of repeating units, i.e. the degree of polymerization, and f is the volume fraction of one block. Here, χ is proportional to the unfavorable interactions between different blocks[3].

Earlier theories for BCP phase behaviors were developed for BCP at the strong segregation limit (SSL), where $\chi N>100$. Meier, Helfand, Wasserman and coworkers developed the self-consistent field theory (SCFT) to describe the BCP chain conformation and chain stretching[4-6]. This theory was later expanded to weak segregation limit (WSL), where $\chi N<10$, by Leibler and coworkers[7]. Masten and coworkers further developed the mean field theory (MFT) by unifying the theory in both SSL and WSL, as well as adding an intermediate regime ($10< \chi N <100$) [8,9]. Nowadays, BCP theory successfully predicts phase diagrams, and domain spacing of BCP, in good agreement with experimental results. In the SSL, MFT of BCP suggests that domain spacing, L_0 scale with χ and N by equation 1.1[3]:

$$L_0 \sim \chi^{1/6} N^{2/3} \tag{1.1}$$

And in the WSL, L_0 scale with χ and N by equation 1.2[3].

$$L_0 \sim N^{1/2} \tag{1.2}$$

According to MFT, diblock copolymer phase behavior in the melt can be described by χN and f as shown in Figure 1.1. In cases where the unfavorable interactions between the dissimilar chains segments are relatively weak, for example $\chi N < 10.5$, the dissimilar chain remains phase mixed, imposing lower limits to periodicity (L_0) of microdomain self-assembled by BCP. With increase of χN, the disorder-order transition (DOT) occurs at $\chi N_{(ODT)}=10.5$ for a symmetric BCP.

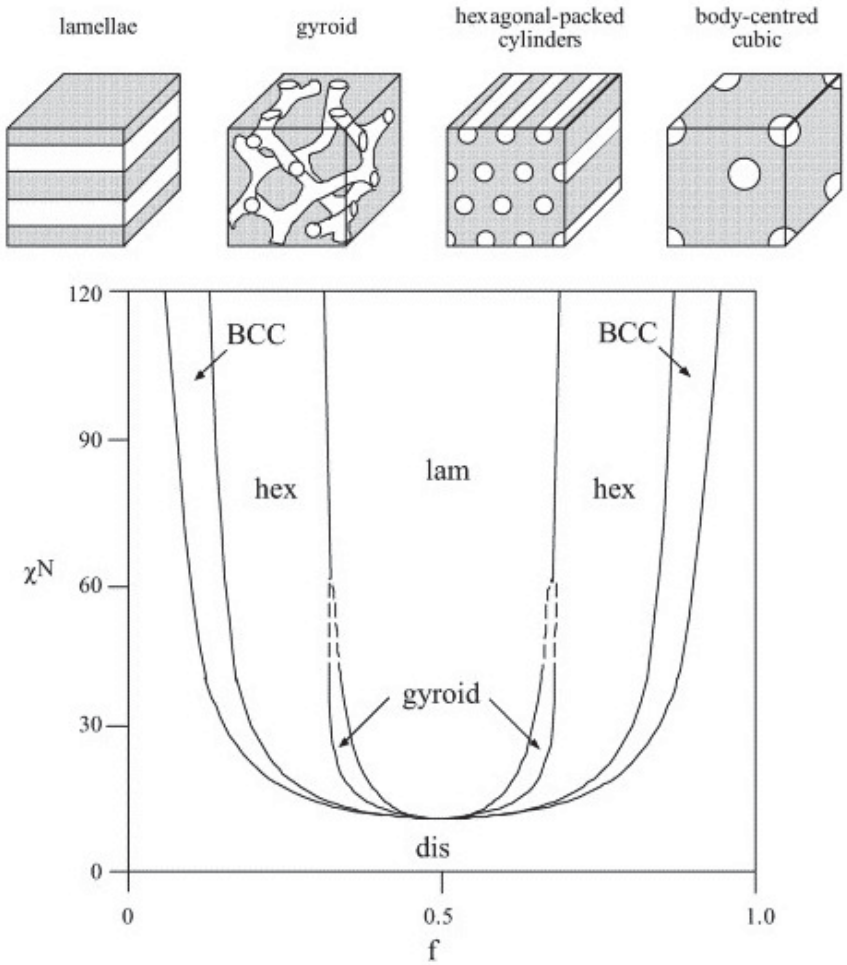

Figure 1.1 Phase diagram of a diblock copolymer, calculated using self-consistent mean field theory. Regions of stability of disordered (dis), lamellar (lam), gyroid (gyr), hexagonal (hex) and body-centered cubic (BCC) phases are indicated. Adapted from reference [10].

The kinetics of BCP chains is also strongly correlated to χN. Diffusion coefficient of block chains in the microphase-separated domain is much slower, up to 4-order magnitudes, than that of homopolymer with similar molecular weight[11]. The linear diblock copolymers with large χN typically take enormous time to self-assemble, which gives the upper limits for the domain spacing self-assembled by BCPs. However, by manipulating the structure of diblock copolymer, for example, use of long side chain

brush copolymer instead of linear BCP, the entanglement of BCP chain could be effectively reduced, enabling faster self-assembly of BCP to form micrometer size scale structure[12,13].

Different morphologies self-assembled by BCPs are also defined by the relative volume fraction of blocks, *f*, as shown in Figure 1.1. Symmetric diblock copolymers form lamellar microdomains, and asymmetric diblock copolymers form cylindrical microdomains or spherical microdomains with decrease the volume fraction of the minor block.

The phase behavior of BCPs is also strongly affected by the temperature[14]. For most BCPs, χ is inversely proportional to temperature (equation 1.3)

$$\chi = A + \frac{B}{T} \tag{1.3}$$

Where A and B are both constants, and B usually has positive values. As the temperature increase, χ decreases, and at a sufficient low χN value, the BCP no longer maintains phase separation and undergoes an order-to-disorder transition (ODT). On the other hand, upon cooling of the heated and phase mixed BCP sample, the BCP undergoes a disorder-to-order transition (DOT) to form microphase-separated microdomain, due to the increased χ.

1.3. Block copolymer thin film

For many lithographic applications of BCP sample, thin film geometry are mandatory. The phase behaviors of BCP thin film, however, are more complicated compared to BCP bulk due to the interfacial energy and confinement effects imposed at both polymer/substrate and polymer/air interface. In the thin film geometry, control of

both orientation and lateral ordering of of BCP microdomains is especially important, thus it will be discussed here.

In the BCP thin film geometry, the orientation of BCP microdomains is critical for BCP lithography applications[15,16]. For the dry etching process, the depth of patterns transferred from a mask is limited by the mask thickness and the selectivity of the specific etching recipe. Perpendicular oriented cylinder or lamellae microdomains have a high aspect ratio and are thus favored for pattern transfer applications. Unfortunately, a perpendicular orientation of BCP microdomains is not favored by nature due to the different surface energies of the two blocks of the copolymer at both the air/polymer and the substrate/polymer interfaces. The morphology of BCP thin films depends on the strength of interfacial interaction at interfaces[17]. Strong preferential interactions of one block with the air/substrate or a lower surface energy of one component cause a segregation of that block to either the surface of the film or the substrate interface. The connectivity of the blocks forces a parallel orientation of the microdomains to the substrate. When the substrate surface becomes neutral, i.e., the interfacial interactions are balanced (equally favorable or unfavorable), there is no preferential segregation of the components to the interfaces. Any slight incommensurability causes the microdomains to orient normal to the surface.

The interfacial energies of a BCP can be precisely controlled by anchoring a random copolymer to the surface, where the volume fraction, f, of monomers in the brush can be varied in the synthesis. As f is varied from 0 to 1, the system goes from a condition of preferential wetting of the substrate by A block to a preferential wetting by B block, in case of A-B diblock copolymer. However, for one value of f the interactions

of A and B with the substrate are balanced. At this point, the microdomains of the BCP orient normal to the surface. This simple concept of balancing interfacial interactions, whether this is done with an anchored random copolymer, a cross-linked random copolymer material, or even, as shown recently, a partial coverage of a BCP on the substrate or by passivating a surface, so as to control the orientation of the BCP microdomains has had a profound impact on the use of BCP as templates for pattern transfer or as scaffolds for the fabrication of nanostructured materials[17,18 19].

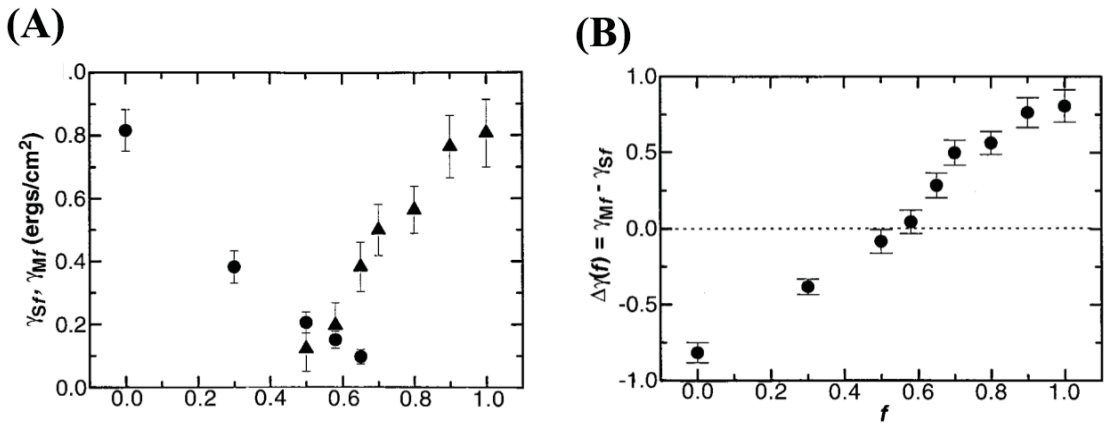

Figure 1.2 Balance the surface interaction between PS and PMMA on PS-r-PMMA neutral layer. (A) interfacial energies γ_{Sf} and γ_{Mf} and (B) $\Delta\gamma(f)= \gamma_{Mf} - \gamma_{Sf}$ for PS (cycle) and PMMA (triangles) on PS-r-PMMA brush as a function of f. Adapted from reference[17].

To give an example, poly(methyl methacrylate) (PMMA) cylinder or lamellae in polystyrene-*block*-poly(methyl methacrylate) (PS-*b*-PMMA) BCPs prefers a parallel orientation to the surface of a silicon wafer due to the preferential interactions of PMMA with the Si-OH at the substrate surface. Russell, Hawker and coworkers used a brush layer, which has neutral surface energy for both PS and PMMA, to control the orientation of PMMA microdomains[17]. A random PS-r-PMMA copolymer with a hydroxyl end

group was anchored to the substrate in order to adjust the surface energy of the silicon substrate, as shown in Figure 1.2. This method, however, requires the hydroxyl groups to be located on the substrate, whereby the application of a hydroxyl terminated neutral brush layer is restricted. The Russell group further improved this method by using a thermally cross-linkable random copolymer brush[18]. A random brush copolymer was spin coated and thermally cross-linked to produce a neutral surface, making it universally applicable to any substrates. Apart from controlling the surface energy at the polymer/substrate interface, a modification of the polymer/air interface was demonstrated by using top coats for BCP thin films[20]. Polydimethylsiloxane (PDMS) has a much lower surface energy compared to PS thus a wetting PDMS layer segregates to the air/polymer interface after thermal annealing of polystyrene-*block*-polydimethylsiloxane (PS-*b*-PDMS) BCPs. Top coats, which aimed to balance the surface energies for PS and PDMS, were spin-coated on the BCP film using the cross solvent. A polymer containing maleic anhydride moiety was designed, which, upon heating, switched its polarity to create a neutral surface for silicon-containing BCPs, thus allowing the lamellae PS-*b*-PDMS microdomains to be oriented normal to substrate.

Instead of using brush layer to balance the interaction between block A and B, external field can be used to overcome the surface energy, thus control the orientation direction of BCP microdomains. For example, the Russell group demonstrated field-induced alignment of microdomains in PS-*b*-PMMA BCP thin films in the presence of electric fields[21]. Solvent vapor gradient is also a strong field and can be used to orient the microdomain normal to the substrate [22].

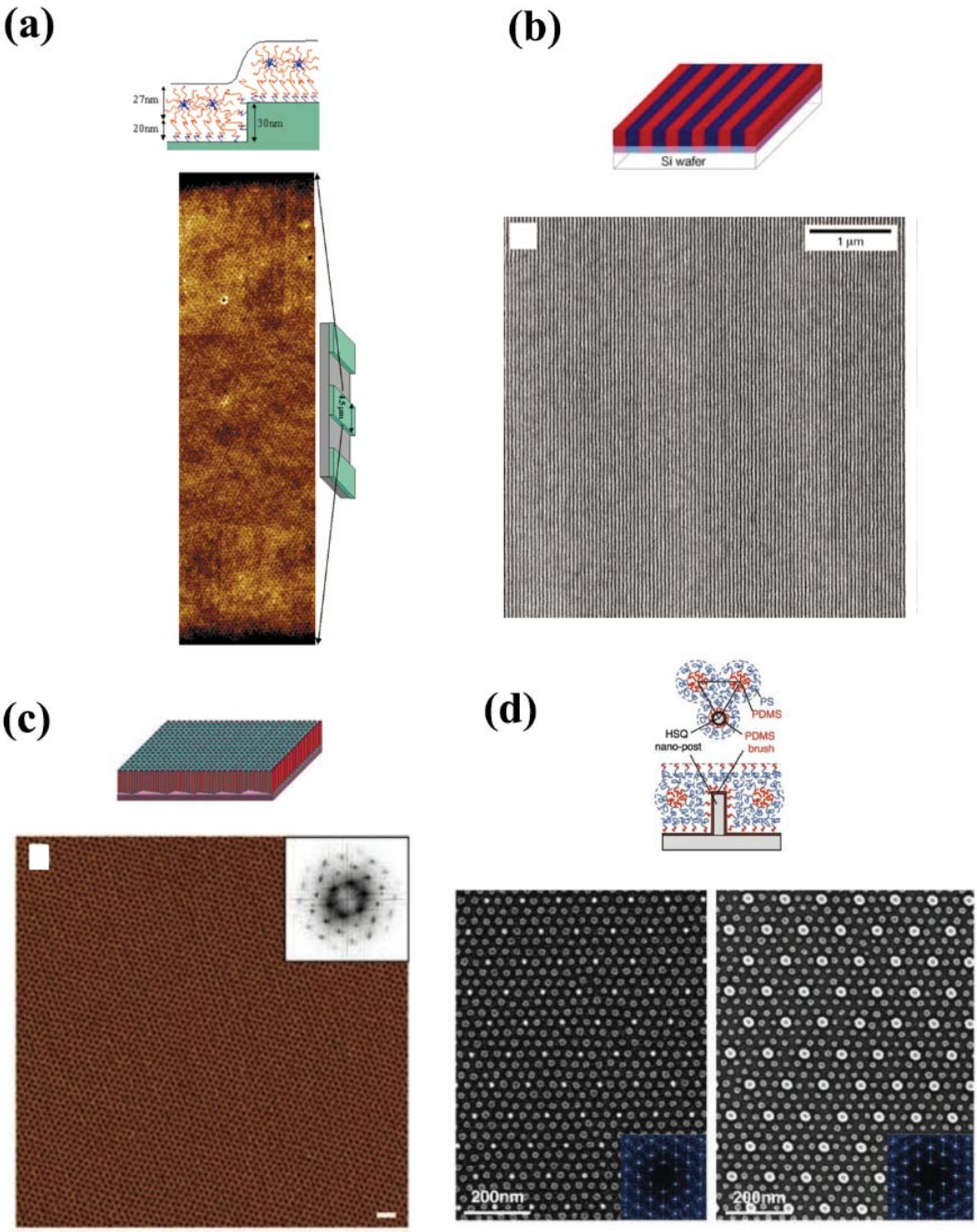

Figure 1.3 Differentways to control the lateral ordering of BCPs using directed self-assembly. (a) Graphoepitaxy (b) Chemical pattern (c) Self-assembled saw-tooth substrate (e) e-beam lithography assisted patterning. Adapted from reference [23-26].

Lateral ordering of the BCP microdomains is equally important for BCP lithography for many applications, where addressability of BCP microdomain is essential.

For example, bit patterned media application requires near-perfect orientational and translational order. Typically, BCP thin films self-assembled on flat substrates have micrometer size scale grain boundary and thus lacking long-range lateral order. The merging of "bottom-up" directed self-assembly (DSA) with "top-down" patterning techniques can potentially enable precise control of lateral ordering of BCP microdomains[15]. Graphoepitaxy, which uses topographic features on the surfaces to bias the lattice orientation of the copolymer microdomains, has been used to bias the orientation of hexagonal lattices. For example, Segalman *et al.* demonstrated the self-assembly of a single grain of polystyrene-*block*-poly (2-vinyl pyridine) (PS-*b*-P2VP) on a patterned silicon substrate, shown in Figure 1.3 a[23]. Various research groups have driven the progress of using topographic patterning to physically constrain BCPs tremendously. The Russell group extensively studied the self-assembly of both polystyrene-*block*-poly(ethylene oxide) (PS-*b*-PEO) and PS-*b*-P2VP/PS-*b*-P4VP BCPs on different topography patterns[25,27 28,29]. Among them, reconstructed faceted sapphire substrates have the ability to direct the self-assembly of microdomains to form arrays with long-range ordering (Figure 1.3c). This approach, which relies on a crystal surface reconstruction, yet another self-assembly progress, does not require large area "top-down" lithography and shows promise as a low-cost approach for roll-to-roll type processes. Ross and coworkers investigated polystyrene-*block*-poly(ferrocenylsilane) (PS-*b*-PFS) and PS-*b*-PDMS BCPs with topography confinement[26,30-32]. They used e-beam lithography to pattern hydrogen silsesquioxane (HSQ) pillars with the desired spacing and shape. Those HSQ pillars, coated with a PDMS brush, showed great capability to direct the self-assembly of PDMS microdomains (Figure 1.3 d). Chemical epitaxy is another way to

direct the self-assembly and to control the lateral ordering of BCPs. Early studies were performed on PS-*b*-PMMA BCPs on alternating stripes of gold (hydrophobic) and silicon dioxides (SiO_2) (hydrophilic) produced by grazing incidence thermal evaporation of gold on a faceted Si wafer surface[33]. Chemical epitaxy also utilizes e-beam lithography to pattern the substrate surface with nanoscale features and provides substrates with chemical contrast. Nealey and coworkers demonstrated the versatility and power of chemically patterned surfaces to the DSA of BCPs in a series of elegant studies (Figure 1.3b) [24,34,35]. Non-symmetrical structures using lithographically defined chemical patterns, like 90 degree bent line, were shown to direct the self-assembly of PS-*b*-PMMA[34]. Also, lithographically defined chemical surface patterns with frequencies over twice as much as the BCP period were used to direct the lateral ordering of BCPs by the so-called density multiplication[35].

1.4. Thermal annealing and solvent vapor annealing

As mentioned in previous section, BCPs in thin film geometry are demanded for a variety of applications. Spin coating is generally used employed to coat the BCP thin film on silicon substrate with high uniformity across large areas. This rather simple coating process, however, creates a problem: the fast solvent evaporation traps the BCP chain into nonequilibrium, disorganized and poorly ordered states. Further treatments of as spun film are used to enhance the ordering of the BCP microdomains, either by thermal or solvent vapor annealing, which introduces the mobility to the polymer chain to facilitate microphase separation and annihilation of defects[49].

Thermal annealing is widely used to remove defects in as spun BCP thin film. In a typical thermal annealing process, BCP thin films are simply heated above its glass transition temperature of the respective blocks of the copolymer and hold at elevated temperature for a certain time, then cooled down to room temperature. For example, PS-*b*-PMMA BCPs are typically annealed at temperatures between 160 and 250 degree depending on its molecular weight. Zone annealing, a more advanced form of thermal annealing, is also reported as a fast way to anneal out the defect in the BCP thin films[37]. In this method, the samples are annealed by passing them over heating and cooling zone to creat a sharp temperature gradient. However, this methodology typically heats the BCP high above its ODT, which is inaccessible for many BCPs with high χN, mainly due to the thermal degradation of BCP at high temperature. Recently, researchers also used a method named cold zone annealing to anneal BCP thin films, where the samples are not required to be heat above its ODT[38]. This methodology, again, works well only for BCP systems where self-assembly process is not limited by slow chain kinetic, limiting it only applicable to BCP with low χ and small molecular weight.

SVA is the other very useful technique to anneal the BCPs thin films, when ODT of BCPs is difficult or even impossible to observe experimentally due to thermal stability limits, which are very common for BCPs with high χ or large molecular weight. Although SVA of BCP thin films does not have a long history, it quickly becomes popular after the seminal work done by Russell group, where cylindrical forming polystyrene-*block*-polyethylene oxide (PS-*b*-PEO) BCP self-assembled into highly ordered hexagonally packed PEO microdomains in a PS matrix after solvent vapor annealed in THF vapor[22].

SVA provides several advantages compared to thermal annealing. First, as mentioned before, solvent vapor annealing provides means to anneal BCPs that are sensitive to thermal degradation. Second, the SVA is generally a more effective method to anneal out defects compared to thermal annealing of BCPs with same molecular weight[39]. Third, solvent vapor mediates the polymer/air surface energy and acts as neutral layer to both blocks[40]. Perpendicularly oriented cylindrical or lamellar microdomains were reported using only solvent vapor annealing without a neutral brush layer on the silicon substrate. Forth, by using selective solvent to anneal BCP film, asymmetric swelling of BCPs changes relative volume ratio between BCP blocks, thus changes the morphology of the BCP film.

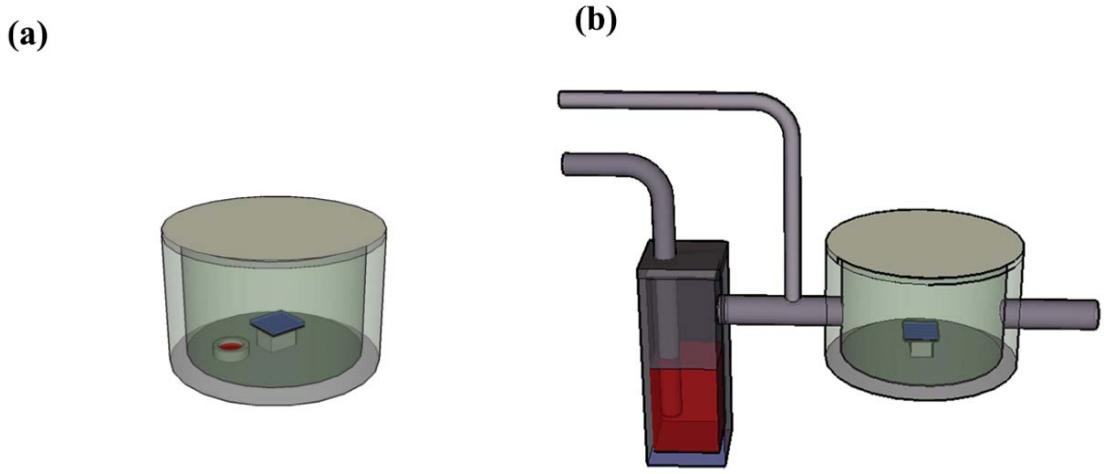

Figure 1.4 Two different set-ups of the solvent vapor-annealing chamber (a) closed jar annealing. (b) Carrying gas assisted solvent delivery annealing.

SVA can be generally categorized into two main varieties depending on the way solvent vapor is introduced into the annealing chamber (shown in Figure 1.4), despite that various research groups used their own SVA set-up. In the first approach, the solvent is kept in a solvent reservoir, and is placed inside an airtight chamber along with the BCP

film (Figure 1.4a). Here, the amount of solvent in the reservoir, the surface area of the solvent, the volume of the chamber, temperature, humidity and annealing time determine the vapor pressure inside the chamber, which dictates the morphology of BCP thin film at its swollen state. Basically, any close systems, in which the certain solvent vapor pressure could build up, can be used as annealing chamber, making them widely adopted by many research groups. However, those rather simple set-ups are not ideal for controlling the vapor pressure in the chamber and difficult for controlled solvent removal after annealing is finished. The SVA setup uses an inert carrier gas to deliver solvent vapor into the annealing chamber (Figure 1.4b). Instead of directly placing the solvent reservoir inside the chamber, a compress inert gas bubbles through the solvent reservoir, and carries the solvent vapors into the annealing chamber. By changing the relative mixing ratio of solvent vapor rich inert gas with pure inert gas provides a convenient way to control the partial vapor pressure of solvent vapor inside the annealing chamber. In addition, shutting down solvent vapor rich inert gas, and purging the chamber with pure inert gas with controlled flow rate gives a simple way to remove solvent in the swollen film after the SVA is done. The disadvantage of this technique is that the highest vapor pressure inside the annealing chamber is rather limited, because the inert carrying gas dilutes the solvent vapor.

Despite the wide use of solvent vapor annealing, a comprehensive understanding of the solvent vapor annealing process has not established. One of the reasons for lack of understanding the SVA process is that, morphology of the BCP films are typically characterized after solvents being removed from swollen film. Detailed studies on the effects of each of these parameters on the morphology of BCP thin films are scarce, yet

they are essential for a controlled annealing and to obtain the desired morphology. There are many other factors affecting the morphology of a BCP film in the swollen state and after removal of solvent vapor, for example, selectivity of the solvent, amount of swelling given to BCP film, solvent removal rates, film thickness, humidity, and temperature. Thus the first part of this thesis focuses on the understanding of the SVA of BCPs using real time measurements. A detailed study of the SVA of BCP will be discussed in chapter 2.

1.5. Lithographic applications by BCP self-assembly

The low-cost, high throughput, large area BCP lithography has great potential to extend Moore's law longer for the semiconductor and data storage industries. Conventional photolithography based on 193nm UV lithography is used to fabricate large area semiconductor chips with features down to 22 nm. The further shrinkage of the feature size using photolithography is restricted by both the wavelength of the light source and resists[41]. While, E-beam lithography provides improved resolution, down to sub 10 nm, but is limited by low through-put and high fabrication costs. Nano-imprint lithography is viable for mass production of devices, but again requires the fabrication of an expensive master template, which relies on e-beam lithography. BCP lithography has been under extensive research both in academia and industry after the first demonstration of BCP lithography by Park *et al*, shown in Figure 1.5 [42]. After years of research and developments, now BCP lithography has been recognized by the International Technology Roadmap for Semiconductor (ITRS) as a possible candidate lithography technique to go beyond the 14nm node[41].

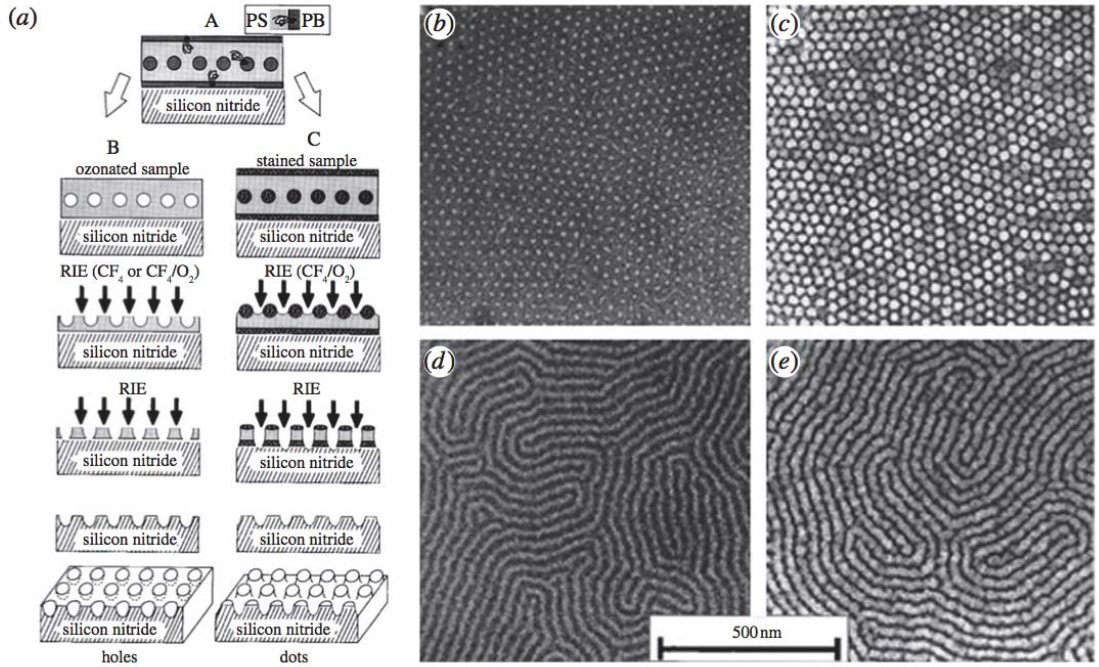

Figure 1.5 (a) Schematic of the pattern-transfer process from PS-*b*-PB to a silicon nitride substrate. (b,d) Self-assembly BCP microdomain, (c,e) patterned silicon nitride nanostructures after pattern transfer. Adapted from reference [42].

To take full advantage of the nanostructures offered by the DSA of BCPs, highly selective pattern transfer techniques with high fidelity are required. Typically, a two-steps etching process is needed to transfer the self-assembled BCP pattern to other functional materials. In the first step, one block of the BCP is selectively removed to make an etch mask; and then the etch mask is further pattern transferred to other functional materials in the second step.

Selectively removal block A from diblock copolymer A-B template is not a simple task. Most BCPs are made of organic materials, where it lacks etching contrast between different blocks. Simple oxygen RIE removes both organic polymer blocks at a similar rate, leaving a flat film that unsuitable for further pattern transfer. Thus, different

methods, depending on the chemical structure of BCP, have been to selectively remove minor block but not the other. For PS-*b*-PMMA BCP, a UV light selectively degrades the PMMA block and crosslinks the PS block at the same time[43]. UV-ozone selective degrades PB block, thus can be used to treat polystyrene-*block*-polybutadiene (PS-*b*-PB) BCP to form PS etch mask[42]. For polystyrene-*block*-poly(lactide) (PS-*b*-PLA) BCP, a weak acid or base is used to selective degrade PLA block using a hydrolysis reaction, thus selectively removes PLA block leaving PS domain as etch mask[44]. But as for other organic BCP systems, PS-*b*-PEO and PS-*b*-P2VP/PS-*b*-P4VP BCPs, a reconstruction process is needed to enhance the etch contrast between two organic blocks which will be discussed in detail in chapter 3 and 4.

For inorganic containing BCP, the mask fabrication from BCPs is much easier. The inorganic containing block is resisting to oxygen reactive ion etching (RIE). A simple oxygen RIE treatment removes organic block, and converts the inorganic block into the inorganic oxides. For example, PS-*b*-PDMS, PS-*b*-PFS and polystyrene-*block*-poly(methyl methacrylate hedral oligomeric silsesquioxane) (PS-*b*-PMAPOSS) were reported to form their respective inorganic oxides replicates the inorganic containing block, which can act as etch mask for the following etching step[45-48]. A summary of chemical structures of commonly used BCPs were given in Table 1, as well as their Flory-Huggins parameters Table 2[49].

After the etch mask being fabricated from self-assembled BCP patterns, a second step pattern transfer is carried out to transfer the mask to other functional materials. Different pattern transfer techniques, including dry etching, wet etching and ion beam etching, all have been used for pattern transfer of BCP etch mask to other materials.

Among those three etching techniques, dry etch is typically used as a directional etch process since the etchant gas is ionized by a high radio frequency field and ions are accelerated towards the sample surface by an electrical field. The highly energetic ions can chemically react with the etch mask and substrate, and can also transfer their kinetic energy to physically remove material via a sputtering mechanism. The mask itself determines the lateral resolution of the transferred pattern. However, the achievable depth of etching profile is limited by the thickness of the mask material, the selectivity of the etching recipe, and the etch quality. An undercut below the mask material is one of the main challenges limiting to achieve high aspect ratio etching profiles. Also a limited mask thickness and poor selectivity make a pattern transfer difficult. Oxygen gas RIE is commonly employed to oxidize and remove organic polymer materials. For silicon (Si) and metals, fluorine based etch chemistry is required for pattern transfer, for example, SF_6, C_2F_8, CHF_3, *etc.*, together with Ar gas. The etch rate varies depending on the different recipes. Typically, a higher radio frequency power (RF) increases the ion density and thus increases the etch rate. Ion milling is basically similar to the RIE etching, but it is a purely directional physical sputtering process. Argon (Ar) ions are typically used for the ion milling process. Dry etching is the preferred method for pattern transfer, as it is generally more controllable and generates less waste. Furthermore, dry etching avoids capillary induced pattern collapse of small polymer features and general shifting of features that can occur with wet processing[50].

Table 1.1 Chemical structure of various block copolymers[49]

Polymer name	Chemical structure
PS-*b*-PMMA	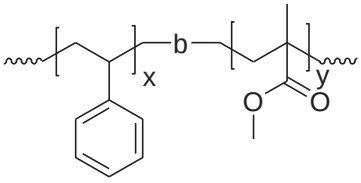
PS-*b*-PEO	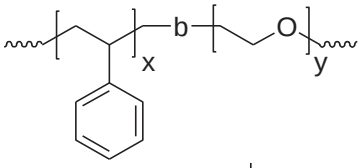
PS-*b*-PI	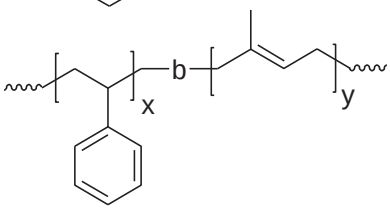
PS-*b*-P2VP	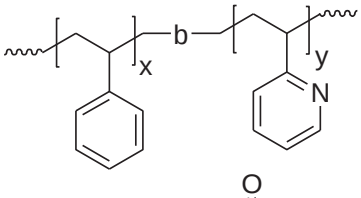
PS-*b*-PLA	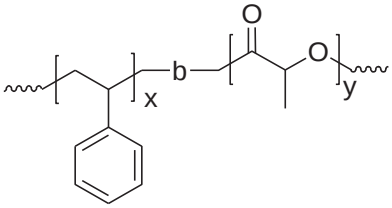
PS-*b*-PDMS	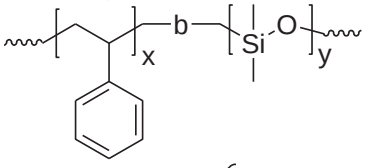
PS-*b*-PFS	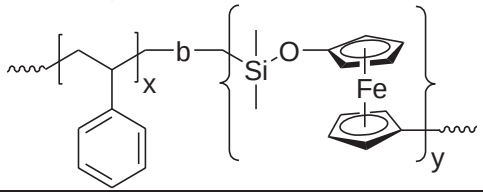

Table 1.2 Flory-Huggins parameter for different block copolymers[49]

Polymer name	Flory-Huggins parameter	χ at 25 degree	χ at 180 degree	χ after normalized by reference volume of 118 Å[51]
PS-*b*-PMMA[52]	4.46 T^{-1}+0.028	~0.043	~0.038	3.5 T^{-1}+0.022
PS-*b*-PEO[53]	29.8 T^{-1}-0.023	~0.077	~0.043	29.8 T^{-1}-0.023
PS-*b*-PI[54]	33 T^{-1}-0.0228	~0.088	~0.050	59.1 T^{-1}-0.071
PS-*b*-P2VP[55]	63 T^{-1}-0.033	~0.178	~0.106	N/A
PS-*b*-PLA[44]	98.1 T^{-1}-0.112	~0.217	~0.105	57.4 T^{-1}-0.061
PS-*b*-PDMS[53]	68 T^{-1}+0.037	~0.265	~0.187	90.7 T^{-1}-0.095

1.6. References

(1) Bates, F. S.; Fredrickson, G. H. Physics Today 1999, 52, 32–38.

(2) Hamley, I. W. Prog. Polym. Sci. 2009, 34, 1161–1210.

(3) Bates, F. S.; Fredrickson, G. H. Annual Review of Physical Chemistry 1990, 41, 525–557.

(4) Helfand, E.; Wasserman, Z. R. *Macromolecules* **1976**, *9*, 879–888.

(5) Helfand, E. *Macromolecules* **1975**, *8*, 552–556.

(6) Meier, D. J. *Journal of Polymer Science Part C-Polymer Symposium* **1969**, 81–98.

(7) Leibler, L. *Macromolecules* **1980**, *13*, 1602–1617.

(8) Matsen, M. W.; Schick, M. *Physical Review Letters* **1994**, *72*, 2660.

(9) Matsen, M. W.; Bates, F. S. *Macromolecules* **1996**, *29*, 1091–1098.

(10) Castelletto, V.; Hamley, I. W. *Current Opinion in Solid State and Materials Science* **2004**, *8*, 426–438.

(11) Yokoyama, H.; Kramer, E. J. *Macromolecules* **1998**, *31*, 7871–7876.

(12) Gu, W.; Huh, J.; Hong, S. W.; Sveinbjornsson, B. R.; Park, C.; Grubbs, R. H.; Russell, T. P. *ACS nano* **2013**, *7*, 2551–2558.

(13) Miyake, G. M.; Piunova, V. A.; Weitekamp, R. A.; Grubbs, R. H. Angew. Chem.-Int. Edit. 2012, 51, 11246–11248.

(14) Russell, T. P.; Hjelm, R. P., Jr; Seeger, P. A. *Macromolecules* **1990**, *23*, 890–893.

(15) Hawker, C. J.; Russell, T. P. *MRS Bulletin* **2005**, *30*, 952–966.

(16) Bang, J.; Jeong, U.; Ryu, D. Y.; Russell, T. P.; Hawker, C. J. *Adv Mater* **2009**, *21*, 4769–4792.

(17) Mansky, P.; Liu, Y.; Huang, E.; Russell, T. P.; Hawker, C. *Science* **1997**, *275*, 1458–1460.

(18) Ryu, D. Y.; Shin, K.; Drockenmuller, E.; Hawker, C. J.; Russell, T. P. *Science* **2005**, *308*, 236–239.

(19) Gu, W.; Hong, S. W.; Russell, T. P. *ACS nano* **2012**, *6*, 10250–10257.

(20) Bates, C. M.; Seshimo, T.; Maher, M. J.; Durand, W. J.; Cushen, J. D.; Dean, L. M.; Blachut, G.; Ellison, C. J.; Willson, C. G. *Science* **2012**, *338*, 775–779.

(21) Morkved, T. L.; Lu, M.; Urbas, A. M.; Ehrichs, E. E.; Jaeger, H. M.; Mansky, P.; Russell, T. P. *Science* **1996**, *273*, 931–933.

(22) Kim, S. H.; Misner, M. J.; Xu, T.; Kimura, M.; Russell, T. P. *Adv Mater* **2004**, *16*, 226–231.

(23) Segalman, R. A.; Yokoyama, H.; Kramer, E. J. *Adv Mater* **2001**, *13*, 1152–1155.

(24) Kim, S. O.; Solak, H. H.; Stoykovich, M. P.; Ferrier, N. J.; de Pablo, J. J.; Nealey, P. F. *Nature* **2003**, *424*, 411–414.

(25) Park, S.; Lee, D. H.; Xu, J.; Kim, B.; Hong, S. W.; Jeong, U.; Xu, T.; Russell, T. P. *Science* **2009**, *323*, 1030–1033.

(26) Bita, I.; Yang, J. K. W.; Jung, Y. S.; Ross, C. A.; Thomas, E. L.; Berggren, K. K. *Science* **2008**, *321*, 939–943.

(27) Park, S.; Kim, B.; Yavuzcetin, O.; Tuominen, M. T.; Russell, T. P. *ACS nano* **2008**, *2*, 1363–1370.

(28) Hong, S. W.; Gu, X.; Huh, J.; Xiao, S.; Russell, T. P. *ACS nano* **2011**, *5*, 2855–2860.

(29) Hong, S. W.; Huh, J.; Gu, X.; Lee, D. H.; Jo, W. H.; Park, S.; Xu, T.; Russell, T. P. *Proceedings of the National Academy of Sciences* **2012**, *109*, 1402–1406.

(30) Cheng, J. Y.; Mayes, A. M.; Ross, C. A. *Nature Materials* **2004**, *3*, 823–828.

(31) Yang, J. K. W.; Jung, Y. S.; Chang, J.-B.; Mickiewicz, R. A.; Alexander Katz, A.; Ross, C. A.; Berggren, K. K. *Nat. Nanotechnol.* **2010**, *5*, 256–260.

(32) Tavakkoli K G, A.; Gotrik, K. W.; Hannon, A. F.; Alexander Katz, A.; Ross, C. A.; Berggren, K. K. *Science* **2012**, *336*, 1294–1298.

(33) Rockford, L.; Liu, Y.; Mansky, P.; Russell, T.; Yoon, M.; Mochrie, S. *Physical Review Letters* **1999**, *82*, 2602–2605.

(34) Stoykovich, M. P.; Muller, M.; Kim, S. O.; Solak, H. H.; Edwards, E. W.; de Pablo, J. J.; Nealey, P. F. *Science* **2005**, *308*, 1442–1446.

(35) Ruiz, R.; Kang, H.; Detcheverry, F. A.; Dobisz, E.; Kercher, D. S.; Albrecht, T. R.; de Pablo, J. J.; Nealey, P. F. *Science* **2008**, *321*, 936–939.

(36) Sinturel, C.; Vayer, M.; Morris, M.; Hillmyer, M. A. *Macromolecules* **2013**, *46*, 5399–5415.

(37) Hashimoto, T.; Bodycomb, J.; Funaki, Y.; Kimishima, K. *Macromolecules* **1999**, *32*, 952–954.

(38) Berry, B. C.; Bosse, A. W.; Douglas, J. F.; Jones, R. L.; Karim, A. *Nano Lett.* **2007**, *7*, 2789–2794.

(39) Park, W. I.; Kim, K.; Jang, H.-I.; Jeong, J. W.; Kim, J. M.; Choi, J.; Park, J. H.; Jung, Y. S. *Small* **2012**, *8*, 3762–3768.

(40) Park, S.; Wang, J.-Y.; Kim, B.; Xu, J.; Russell, T. P. *ACS nano* **2008**, *2*, 766–772.

(41) ITRS. **2011**.

(42) Park, M.; Harrison, C.; Chaikin, P. M.; Register, R. A.; Adamson, D. H. *Science* **1997**, *276*, 1401–1404.

(43) Thurn-Albrecht, T.; Steiner, R.; DeRouchey, J.; Stafford, C. M.; Huang, E.; Bal, M.; Tuominen, M.; Hawker, C. J.; Russell, T. P. *Adv Mater* **2000**, *12*, 787–791.

(44) Zalusky, A. S.; Olayo-Valles, R.; Wolf, J. H.; Hillmyer, M. A. *J. Am. Chem. Soc.* **2002**, *124*, 12761–12773.

(45) Jung, Y. S.; Ross, C. A. *Nano Lett.* **2007**, *7*, 2046–2050.

(46) Lammertink, R.; Hempenius, M.; van den Enk, J.; Chan, V.; Thomas, E.; Vancso, G. *Adv Mater* **2000**, *12*, 98–103.

(47) Cheng, J.; Ross, C.; Chan, V.; Thomas, E.; Lammertink, R.; Vancso, G. *Adv Mater* **2001**, *13*, 1174–1178.

(48) Hirai, T.; Leolukman, M.; Liu, C.-C.; Han, E.; Kim, Y. J.; Ishida, Y.; Hayakawa, T.; Kakimoto, M.-A.; Nealey, P. F.; Gopalan, P. *Adv Mater* **2009**, *21*, 4334–4338.

(49) Gu, X.; Gunkel, I.; Russell, T. P. *Phil. Trans. R. Soc. A* **2013**, **371**, 20120306**2013**.

(50) Liu, C.-C.; Nealey, P. F.; Ting, Y.-H.; Wendt, A. E. *J. Vac. Sci. Technol. B* **2007**, *25*, 1963–1968.

(51) J. G. Kennemur, M. A. Hillmyer, F. S. Bates, *Macromolecules* **2012**, *45*, 7228–7236.

CHAPTER 2

IN SITU X-RAY SCATTERING INVESTIGATION OF BCP SELF-ASSEMBLY DURING THE PROCESS OF SOLVENT VAPOR ANNEALING

2.1. Introduction

The self-assembly (SA) and directed self-assembly (DSA) of block copolymer (BCP) thin films have attracted significant interest as routes to generate nanostructured materials. The ability to selectively remove one component or to do phase selective chemistries in the nanoscopic microdomains of the BCP have enabled applications ranging from templates for pattern transfer[1-4], used in the microelectronics industry to generate low dielectric constant materials, to scaffolds for the fabrication of nanoscopic inorganic elements[5,6], used for the generation of surface plasma or magnetic elements[7], to simple porous films, used for the realization of membranes with well-defined pore sizes, used as separations media for virus particles[8,9]. By controlling the lateral ordering of the microdomains, i.e. directing the self-assembly of the microdomains, by tailoring interfacial interactions or the topography of the substrate, highly ordered arrays of the microdomains can be achieved that are addressable[10-14]. With microdomains that can be as small as ~3 nm, areal densities of the elements can exceed 10 Tera dots/in^2, which for bit patterned media applications in the storage industry, has generated significant interest[14]. Achieving microdomain morphologies with the desired orientation and lateral ordering over large areas mandates controlling the interactions of each block of the BCP

with the substrate and air interfaces, the surface topography and chemistry, and sufficient mobility to the polymer to laterally order in a rapid manner.

Achieving lateral order in thin films of BCPs typically requires thermal annealing or solvent vapor annealing (SVA). In a thermal annealing experiment, the BCP film is heated to temperatures above the glass transition temperatures (T_g) of both blocks, imparting mobility to the BCP to enable SA or DSA. If the BCPs have a rigid backbone, as in the case of brush block copolymers, diffusion is rapid and lateral ordering can be achieved rapidly, even with very high molecular weights[15]. For BCPs with flexible backbones, diffusion processes are slow, even at elevated temperatures, due to chain entanglements, and achieving long-range lateral ordering can be time consuming[16]. To circumvent this, solvent annealing processes have been used where, by placing the BCP film in a solvent vapor atmosphere, the solvent swells the BCP film, reducing the T_g of the BCP and markedly enhancing the mobility. Consequently, long-range lateral ordering of the BCP can be achieved at room temperature within minutes. Both low molecular weight solvents and super critical CO_2 have been used to achieve this[17].

SVA is more complex than thermal annealing. The swelling of the BCP can cause changes in the morphology, due to differences in the solubility of the solvent in different blocks, leading to changes in the volume fractions of the components, as well as the interactions between the blocks. While mobility is enhanced, the period of the swollen BCP morphology has changed. The solvent also mediates interactions of the blocks with the substrate, the surface energies of the swollen blocks, and the segmental interactions between the blocks. If the solvent is neutral, i.e. equally soluble in both blocks, the solvent molecules screen non-favorable interactions between the segments of the two

blocks causing changes in the configuration of the chains anchored to the interface between the microdomains[18]. If, on the other hand, the solvent is highly selective to one block, then the non-favorable interactions can be increased[19,20]. Depending on the vapor pressure of the solvent, the concentration of the solvent in the BCP film will vary and, if the concentration is sufficiently high, the BCP can be driven into the disordered state. If the BCP is disordered, then, as solvent is removed, the BCP orders at the air surface initially. Lateral ordering at the surface occurs, due to the high mobility of the ordered surface layer. As solvent is continuously removed, an ordering front propagates into the film that is templated by the microdomains formed initially at the surface[21]. Consequently, lateral ordering and orientation of the microdomains result. If the swollen BCP remains microphase separated, then enthalpic interactions between the segments of the blocks and entropic penalties associated with the packing of the chains at the substrate and air interfaces will dictate the period of BCP and the lateral ordering. The concentration of the solvent in the BCP on the other hand determines the chain mobility. High concentration of the solvent guarantees the increased mobility, which leads to a faster response of the BCP chains and allows for larger gain sizes.

Gradually removing a solvent from a BCP dilute solution to enhance the ordering of BCP microdomains is well established in the bulk. Hashimoto and coworkers, and Thomas and coworkers, for example, used exceptionally slow solvent evaporation to generate highly ordered BCP microdomains for small angle X-ray scattering and electron microscopy studies[22-25]. In thin films, the use of a solvent to control the ordering and orientation of BCP microdomains was first reported by Kim and Libera where, for triblock copolymers of poly(styrene)-*block*-poly(butadiene)-*block*-poly(styrene), the

morphology strongly depended on the solution casting conditions[26]. Different solvent evaporation rates resulted in different orientations of the cylindrical microdomains, either in-plane or out-of-plane. Lin et al. found that for polystyrene-*block*-polyethylene oxide (PS-*b*-PEO) the orientation of the BCP microdomains normal to the film surface in thick films could be achieved by controlled solvent evaporation[27]. Kim *et al.*, using *in situ* grazing incidence x-ray scattering, showed that PS-*b*-PEO self-assembled into highly ordered hexagonally packed PEO microdomains in a PS matrix after the BCP thin film was annealed in benzene or in water/benzene vapors[21]. With benzene, the film is driven into the disordered state and a highly ordered and oriented array of BCP microdomains was achieved. With water/benzene, two immiscible solvents, a single layer of micelles formed that laterally ordered and, upon solvent removal, produced cylindrical domains oriented normal to the film surface. SVA has since been widely used to generate ordered morphologies in BCP thin films. Ross and coworkers, Kramer and coworkers, and others have investigated solvent annealing process of PS-*b*-PDMS and PS-*b*-P2VP/PS-*b*-PEO[11,28-36]. Albert *et al.* investigated the effect of solvent removal rate on the morphology of triblock copolymer thin films by *ex situ* scanning force microscopy (SFM) [37]. As with Kim and Libera, different orientations of the microdomains were found, depending on the solvent removal rates. *In situ* SFM was also used to image the morphology change during the SVA[38]. *In situ* x-ray scattering was used by Papadakis and coworkers to monitor the SVA induced ordering of lamellae-forming polystyrene-*block*-poly(methyl methacrylate) (PS-*b*-PMMA) using toluene or cyclohexane [39-42]. Ober and coworkers observed a transition from a cylindrical to spherical microdomain morphology in a selective solvent by using *in situ* x-ray scattering [43]. Russell and coworkers have used

in situ GISAXS to investigate the ordering of BCPs during SVA for a range of different BCPs [44-47]. The SVA in thin BCP has recently been extensively reviewed by Sinturel *et al*[48].

Yet, there are still questions that remain unanswered that may limit this very promising route to orient and order BCPs. When a neutral solvent is introduced to a BCP, the period of the BCP will decrease and the lateral dimension, *e.g.* length of cylinder, will increase. The BCP, though, is laterally confined to the area of the substrate, resulting in an incommensurability with the decreasing period of the BCP during swelling. The reduced period results from a relaxation of the BCP chains at the interface between the microdomains, giving rise to an increase in the area occupied by the chains at the interface. This effect has been observed in previous studies on bulk phases[22]. The confinement in thin films, however, results in an incommensurability as soon as the period changes that will not be observed in bulk. When the BCP film is swollen, the total volume of the film increases and, due to the lateral confinement, the film thickness increases, since the occupied surface area on the substrate remains fixed. The swelling ratio (SR) is the thickness of the swollen film divided by the original thickness. For microdomains oriented normal to the surface, this thickness change can be accommodated by the translational diffusion of the BCP chains along the interface between the microdomains. However, when the microdomains are oriented parallel to the substrate, there is an incommensurability between the swollen film thickness and the period of the swollen BCP microdomains. Consequently, there must be a re-distribution of BCP chains in the film, the generation of more microdomains, and the appearance of a surface topography. Upon solvent removal, the mobility of the BCP chains in a

microphase separated environment and the reformation of microdomains are critical in defining the final morphology of the dried film.

This chapter contains a systematic study of the self-assembly of cylinder-forming PS-*b*-P2VP BCPs during the process of SVA in THF (a near neutral solvent) vapor. *In situ* GISAXS experiments were performed during the swelling of the BCP films and as the solvent was removed in a controlled manner. The characteristics of the BCP film during swelling and de-swelling processes were determined, providing insights into the SVA and de-swelling processes and the impact on the lateral ordering of the BCP microdomains. BCP with different molecular weights were also investigated to understand how the molecular weight influences the solvent annealing process. Finally, a comparison of thermal annealing and solvent vapor annealing is discussed here.

2.2. Experimental

2.2.1. Materials and sample preparation

In this study, PS-*b*-P2VP BCPs were purchased from Polymer Source Inc. and used without further purification. The BCP samples are listed in table 2.1. Tetrahydrofuran (THF), toluene and ethanol were purchased from Sigma-Aldrich and used without further purification. BCPs were dissolved in a mixture of THF and toluene to form a uniform solution and then stirred overnight before use. Thin films of BCPs were prepared by spin coating the respective BCP solutions on to oxygen plasma cleaned silicon wafer substrates. Typical spin coating speeds were 2000/3000/4000 revolutions per minute (rpm) for 45 seconds at a ramp rate of 1500 rpm per second. Varying the

concentration of the block copolymer solution and the spin coating speeds controls the film thicknesses of coated samples. The 5 cm by 5cm as-spun films were cut into 1.5cm by 1.5cm pieces and were then used for further experiments to ensure consistent film thickness and morphology across different samples.

Table 2.1: List of BCPs with different molecular weights used in this study

Name	Molecular weight*	Volume fraction of P2VP	PDI
PS-*b*-P2VP 22k	14.8-*b*-6.5	28.8%	1.05
PS-*b*-P2VP 27k	18.0-*b*-9.0	31.5%	1.08
PS-*b*-P2VP 34k	23.6-*b*-10.4	28.9%	1.04
PS-*b*-P2VP 43k	30.0-*b*-12.5	27.7%	1.06
PS-*b*-P2VP 58k	40.0-*b*-18.0	29.3%	1.07
PS-*b*-P2VP 115k	79.0-*b*-36.5	29.8%	1.05
PS-*b*-P2VP 275k	185.0-*b*-90.0	30.9%	1.10

* Molecular weights of BCPs are provided by Polymer Source Inc.

2.2.2. Custom built solvent vapor annealing chamber

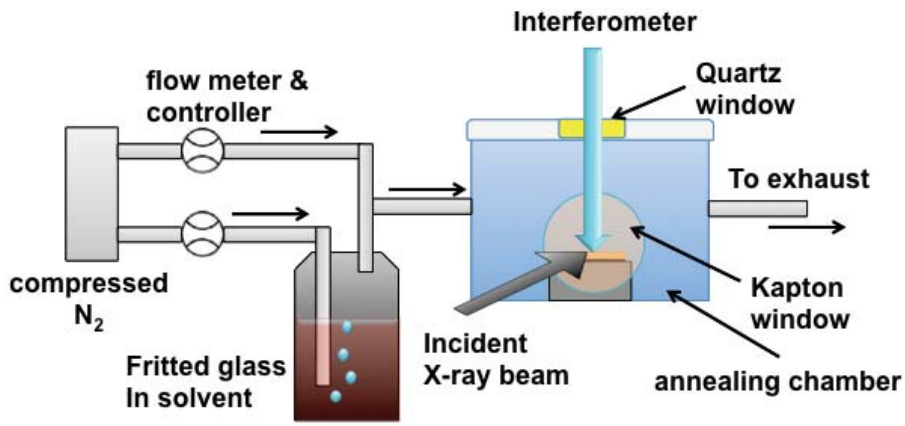

Schematic 2.1 *In situ* X-ray scattering experiment set-up.

The BCP films were placed in a custom-designed solvent vapor-annealing chamber to carry out real-time *in situ* GISAXS at 23±0.5^{o}C as solvent vapor was added or removed (shown in Schematic 2.1). Kapton windows (~100 um thick) on the front and rear of the chamber allowed the x-rays to enter and exit the chamber, respectively. A quartz window on top of the sample chamber allowed the film thickness to be measured in real-time using an optical interferometer (Filmetrics F20). THF vapor was introduced into the chamber (as shown) using N_2 as the carrier gas. Two gas streams, a pure N_2 gas and a THF-rich N_2, were mixed before flowing into the annealing chamber, so that the vapor pressure could be controlled. The fraction of solvent vapor in the experimental cell, i.e. the partial pressure and vapor pressure of THF, could be varied by adjusting the relative flow rates of the pure and THF-rich N_2[49]. This design also enabled the removal of solvent vapor inside the chamber by closing the THF-saturated vapor inlet and purging the chamber with pure N_2. The rate of solvent removal from the chamber was controlled

by varying the flow-rate of pure N_2 into the chamber. Flow rates varied from 5 standard cubical center meter per minute (sccm) to 50 sccm for slow to rapid removal of the solvent, respectively.

2.2.3. Grazing incidence small angle X-ray scattering

Grazing incidence small angle X-ray scattering (GISAXS) measurements were performed at Beamline 7.3.3 at the Advanced Light Source, Lawrence Berkeley National Laboratory, at a constant X-ray energy of 10 keV. The exposure time to collect each scattering profile was 20 s. After two exposures, the sample was moved to a fresh area to minimize errors due to beam damage of the sample. The sample-to-detector distance and, hence, scattering vector was calibrated using a silver behenate standard. The incidence angle between x-rays and the sample surface was changed between 0.14^{o} and 0.16^{o} depending on the different samples. Scattering profiles were recorded on a Pilatus 1M 2-D area detector.

The data reduction of scattering profiles was performed using "Nika", an Igor (Wave Metrics Inc.) based software package developed by a beamline scientist at the Advanced Photon Source, Argonne National Laboratory (http://usaxs.xray.aps.anl.gov/staff/ilavsky/nika.html) [50]. The 2-D scattering data was reduced to a 1-D scattering profile by slicing the 2-D scattering pattern in the in-plane direction, where the scattering intensity is plotted vs. the scattering vector. The in-plane scattering pattern was then fitted by using a Gaussian function according to equation (2.1), as shown in Figure 2.1.

$$y(x) = \underbrace{y_0 + Cx^{-d}}_{Background} + \underbrace{De^{-\ln 2\left(\frac{x-x_0}{b}\right)^2}}_{Gaussian} \tag{2.1}$$

The fitted Gaussian peak gives the peak position, corresponding to the periodicity of the BCP microdomain, and the FWHM, corresponding to the grain size of assemble BCP microdomain. The 2-D scattering profiles in the out of plane direction were simulated in the frame of the Distorted-Wave Born Approximation (DWBA) using HipGISAXS， which was developed by Alexander Hexemer at the Advanced Light Source at Lawrence Berkeley National Laboratory[51].

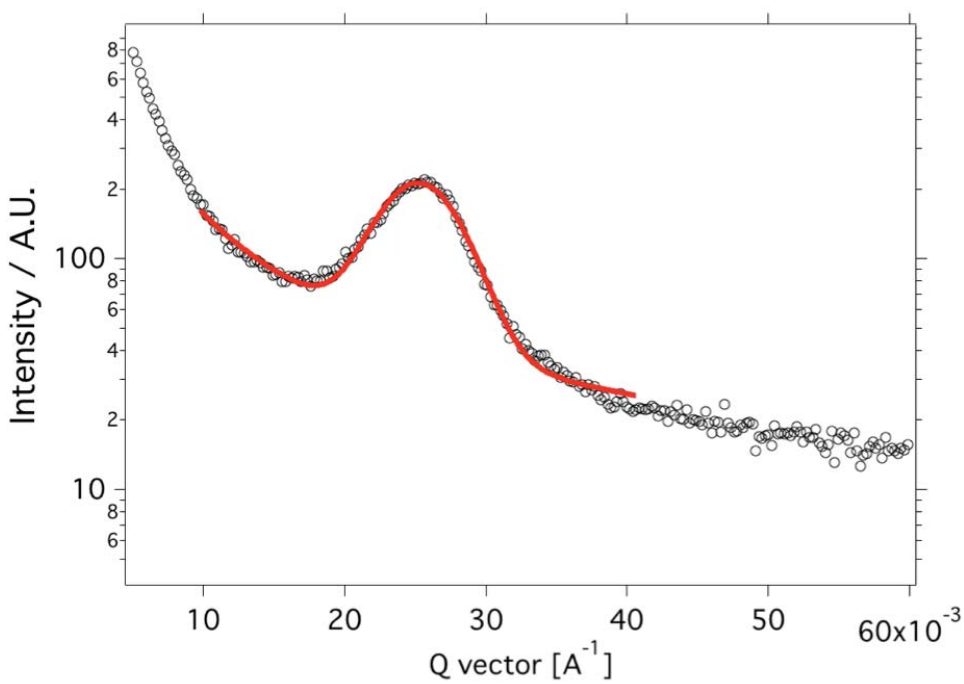

Figure 2.1 Typical scattering profile (open spheres) in qy direction along with the corresponding fit (solid red line) to equation (2.1)

2.2.4. Film thickness measurements by optical interferometry

The real time measurement of the BCP film thickness was carried out using Filmetrics interferometer model F20 (Filmetrics Inc.). The interferometer use light wave interference effect to characterize the film thickness and reflective index of the BCP thin film. The interferometer was built onto the chamber to fix the optical axis. Each film thickness measurement takes less than a second. The film thickness data was collected at an interval of 10 seconds and automatically stored in the software.

2.2.5. Surface morphology measurement

The surface morphology of the BCP thin films was characterized by a Veeco Nanoscope 3a scanning force microscope (SFM) in tapping mode and a Zeiss Ultra 60 field emission scanning electron microscope (SEM).

The SFM was used to image the top surface morphology of the BCP sample in the tapping mode. The samples were reconstructed in ethanol and etched in oxygen plasma, to enhance the contrast for SEM measurements. Solvent annealed samples were reconstructed in ethanol for 10min, then etched in oxygen plasma for 10 s (Oxford Instruments plasma lab 100, 10 mTorr, 20 sccm O_2, 75 W) to enhance the electron density contrast between PS and P2VP domains [4]. The sample surfaces were coated by 3 nm layer of gold to reduce the charging effect by SEM. The SEM images were further processed by Matlab (Mathworks Inc.) to code the orientation of the microdomains with different colors to aid in viewing the grains of the microdomains.

The top surface of BCP thin films was characterized by a Zeiss interference optical microscope.

2.2.6. Molecular weight characterization by GPC

The molecular weight of copolymer was determined by use of an Agilent 1200 Series HPLC equipped with a refractive index detector. A PLgel 10-µm miniMIX-B 250 ×4.6 mm column (Varian, Inc.) was employed with dimethylformamide (DMF) eluent (0.3 mL/min) and calibrated by using polystyrene standard samples (Agilent Technologies) in DMF with molecular weights ranging from 500 to 6 870 000 g/mol.

2.3. Results and discussion

2.3.1. SVA of BCP thin films: the swelling process

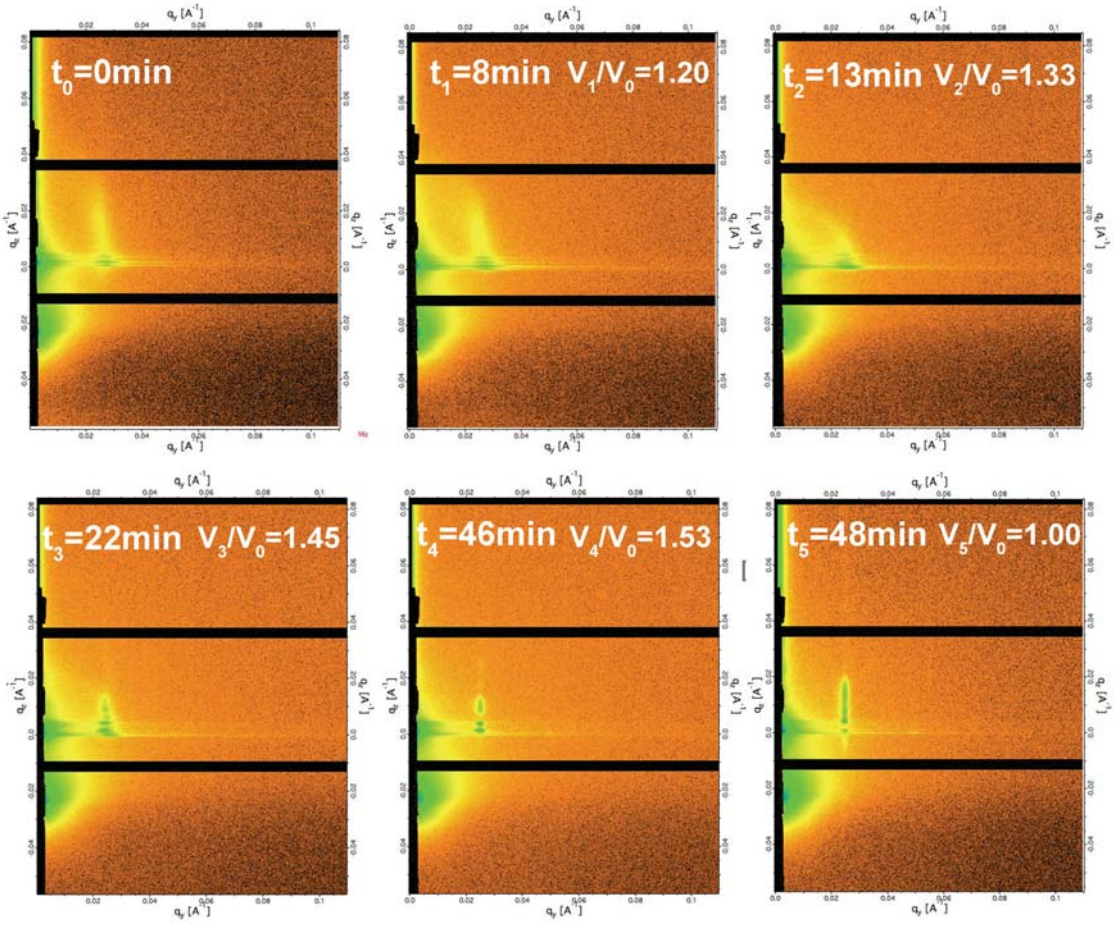

Figure 2.2 GISAXS scattering patterns of a swollen BCP film at different times. The indicated volume ratio corresponds to the swelling ratio as determined from the increase of film thickness during annealing.

A PS-*b*-P2VP 34k BCP thin film with an initial film thickness of 85nm was annealed in the THF vapor using the custom built annealing chamber. A series of GISAXS profiles obtained as a function of time during swelling is shown in Figure 2.2. The scattering profile of the as-spun PS-*b*-P2VP thin film (t_0) shows a well-defined, but diffuse reflection, at a Bragg spacing of 23.2 nm. This distance is much less than the equilibrium period of this BCP in the bulk of 28.0 nm. The full width at half maximum (FWHM) of ~6.5 x 10^{-2} nm^{-1}, which, using the Scherrer analysis, corresponds to a characteristic persistence of the interference of 87 nm, indicates that the order is only short range[52]. The slight bowing of the reflections indicates that there are interferences out of the sample plane and that the morphology is not well developed. During the first 8 minutes of exposure to THF vapor the film thickness has increased by 20%, indicating a swelling of the film with THF, but the scattering profiles did not change significantly. However, a close examination of the profile shows that the extension of the scattering normal to the surface has decreased. During this time period, the glass transition temperature (T_g) of the swollen BCP decreased below room temperature, imparting mobility to the BCP. The T_g of the 20% swollen BCP, estimated from the Fox-Flory equation (equation 2.2), is calculated to be ~18°C, which is below room temperature (Figure 2.3) [53]. The T_g of the BCP in the swollen state can be predicted by the Flory-Fox equation:

$$\frac{1}{T_{g,PS/THF}} = \frac{w_{PS}}{T_{g,PS}} + \frac{w_{THF}}{T_{g,THF}} = \frac{\phi\rho_{PS}}{\phi\rho_{PS}+(1-\phi)\rho_{THF}} * \frac{1}{T_{g,PS}} + \frac{\phi\rho_{THF}}{\phi\rho_{PS}+(1-\phi)\rho_{THF}} * \frac{1}{T_{g,THF}} \qquad (2.2)$$

where ϕ is the concentration of polymer in the swollen film, ρ_{PS} is the density of the PS ~ 1.0 g/cm^3, ρ_{THF} is the density of the THF ~ 0.889 g/cm^3 and $Tg_{,THF}$ =130K, $Tg_{,PS}$=373K.

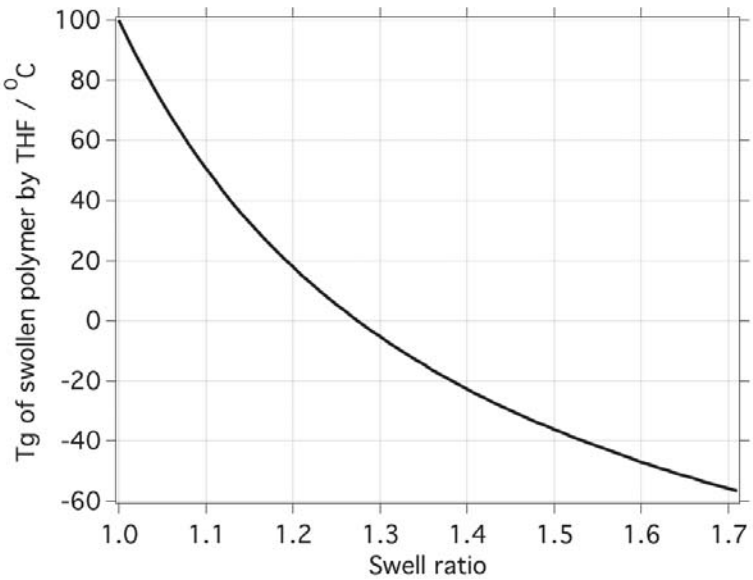

Figure 2.3 Predicted values for the glass transition temperature of PS-*b*-P2VP block copolymers swelled by different amounts of THF according to the Flory-Fox equation 2.2.

After 8 min (t_1), the reflection shifts to smaller q_y, larger spacing in-plane, with the bowing of the reflection in q_z being still evident. With increasing annealing time (t_2), the reflection broadens further, with a ring of scattering developing, indicating a further re-organization and disordering of the BCP. However, as the swelling of the BCP film continues (t_3), the GISAXS reflection continues to shift to smaller q_y, corresponding to a larger in-plane spacing, intensifies, and sharpens considerably (FWHM decreasing significantly) with an interference maximum being seen at q_y = 0.241 nm^{-1}, corresponding to a distance of 26.0 nm. With further swelling (t_4), the reflection maintains its overall shape, but shifts slightly to larger q_y, while the FWHM decreases

slightly. After swelling for 48 min (a final swelling ratio of 1.53), the solvent was rapidly removed by removing the top cover of the chamber to maximize the rate of evaporation of the solvent. The scattering pattern was stretched in the q_z direction, due to the reduced film thickness. In addition, the domain spacing and the FWHM increased slightly, indicating the introduction of some disorder during the solvent removal process. The intensity of the scattering also increased as a consequence of the increased contrast between the microdomains due to the solvent removal. It should be noted that reflections characteristic of a hexagonal packing of the microdomains parallel to the surface of the film were not observed, indicating that the consecutive layers of the cylindrical microdomains were not in register.

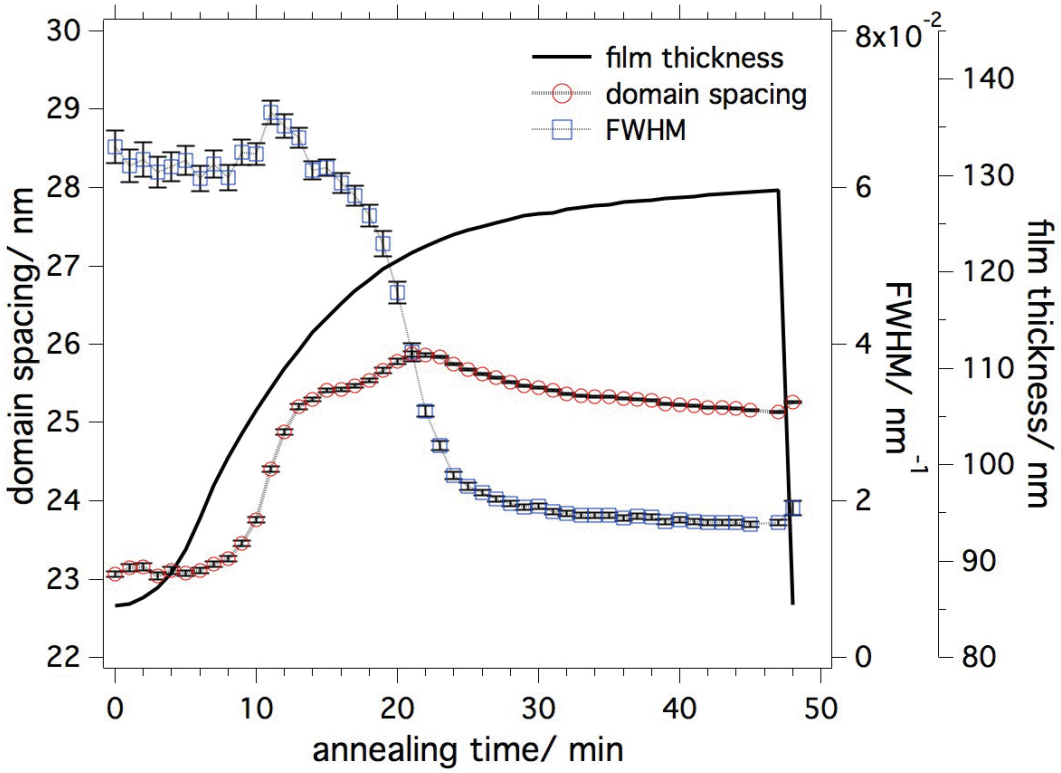

Figure 2.4 *In situ* GISAXS measurement of an as spun PS-*b*-P2VP film during solvent vapor Annealing in THF. Domain spacing (filled triangle), FWHM (filled circle), film thickness (solid line) vs. annealing time.

The scattering along q_y was further analyzed by fitting the intensity profiles along q_y, i.e. in the in-plane direction, to a Gaussian function so that the peak position and FWHM could be quantitatively determined. The Bragg spacing determined from the peak position, the FWHM and the film thickness are plotted together in Figure 2.4. From these data, an apparent induction period is observed up to t_1=8min, followed by a sharp increase in the spacing with little change to the FWHM up to t_2=13min, then a further increase of the spacing with a sharpening of the reflection (t_3=22nm), and then a slight decrease in the Bragg spacing, along with a further narrowing of the reflection (t_4=46min).

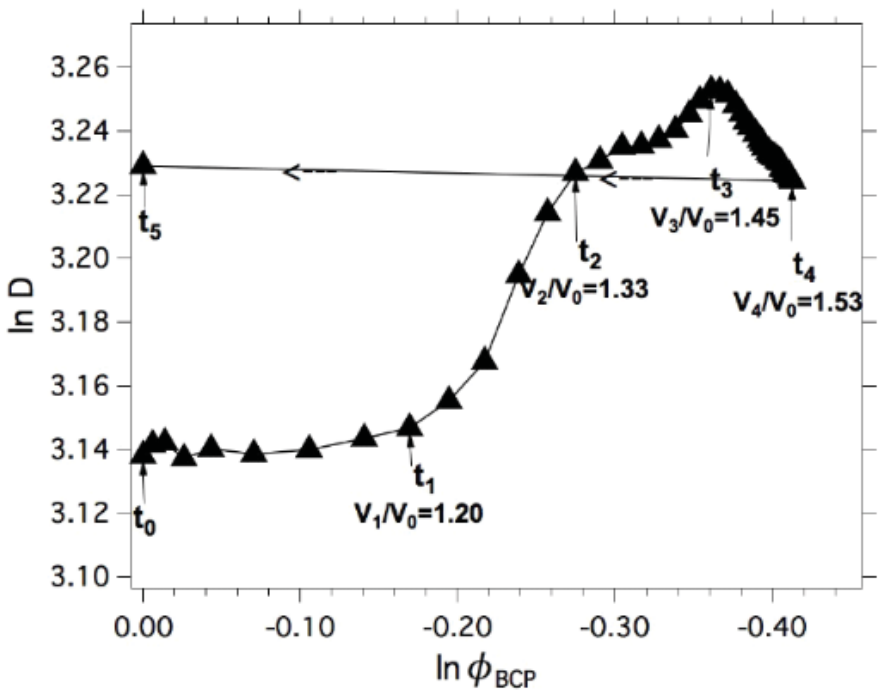

Figure 2.5 Ln of domain spacing of BCP in figure 2.4 as a function of ln of volume fraction polymer in the swollen film as calculated from the film thickness data shown in Figure 2.4.

In Figure 2.5 these data are plotted in a ln-ln manner. The different regimes encountered during the swelling process, as described above, are noted. These different regimes reflect the initial mobilization of the BCP chains due to the introduction of the solvent, the increase in the period as the BCP microdomains transition from the kinetically-trapped, spin-coated morphology, and the final decrease in the period at longer times, due to a relaxation of the BCP chains at the interfaces of the microdomains arising from the mediation of segmental interactions by the solvent. Plotted in this manner, it is very evident that the decrease in the period with increasing solvent concentration (from t_3 to t_4) follows a power law behavior with an exponent of 0.64 (~2/3). This exponent is much larger than that reported previously by Hashimoto and coworkers[22] and Lodge and coworkers[54], where the period of the lamellar microdomain morphology varied with the volume fraction of BCP as $\phi_{BCP}{}^{1/3}$.

The observed changes in the period can be described using mean-field theory arguments in the intermediate segregation regime, coupled with a concentration dependent interaction parameter (beyond the dilution approximation) [55,56]. The total number of BCP repeat units N is ~ 330. The temperature dependence of the Flory-Huggins segmental interaction parameter of PS-*b*-P2VP in the bulk (dry) was reported as [57]:

$$\chi_{dry} = \frac{63}{T} - 0.033 \tag{2.3}$$

At T=23°C, χ ~ 0.18, and χN ~ 59 in the dry state corresponding to a BCP in the strong segregation regime. When the BCP is swollen by a neutral solvent, using the dilution approximation, the effective χ is given by

$$\chi_{eff} = \chi_{dry}\phi_{BCP}^{\beta} \tag{2.4}$$

If the dilution approximation holds, β=1, χ_{eff} varies linearly with $\phi_{BCP} = \frac{V_{dry}}{V_{swell}} = SR^{-1}$, the BCP volume fraction. Lodge and coworkers found that the dilution approximation failed [54,56] and β values varying from 1.3 to 1.6 could describe their results. Now, for the swollen BCP, χ_{eff}N ~ 30, which corresponds to a BCP in the intermediate segregation regime, the repeat period is given by [55]

$$D \sim aN^{\frac{1}{2}}(\chi N)^{\alpha} \tag{2.5}$$

And with $\chi_{eff} = \chi_{dry}\phi_{BCP}^{\beta}$, then, by substitution,

$$D \sim aN^{\frac{1}{2}}N^{\alpha}\chi_{Dry}^{\alpha}\phi_{BCP}^{\alpha\beta} \tag{2.6}$$

If β varies from 1.3 to 1.6 and α = 0.40, which is predicted in case of intermediate segregation [55], then

$$D \sim \phi_{BCP}^{0.52\sim0.64} \tag{2.7}$$

It agrees well with our observations.

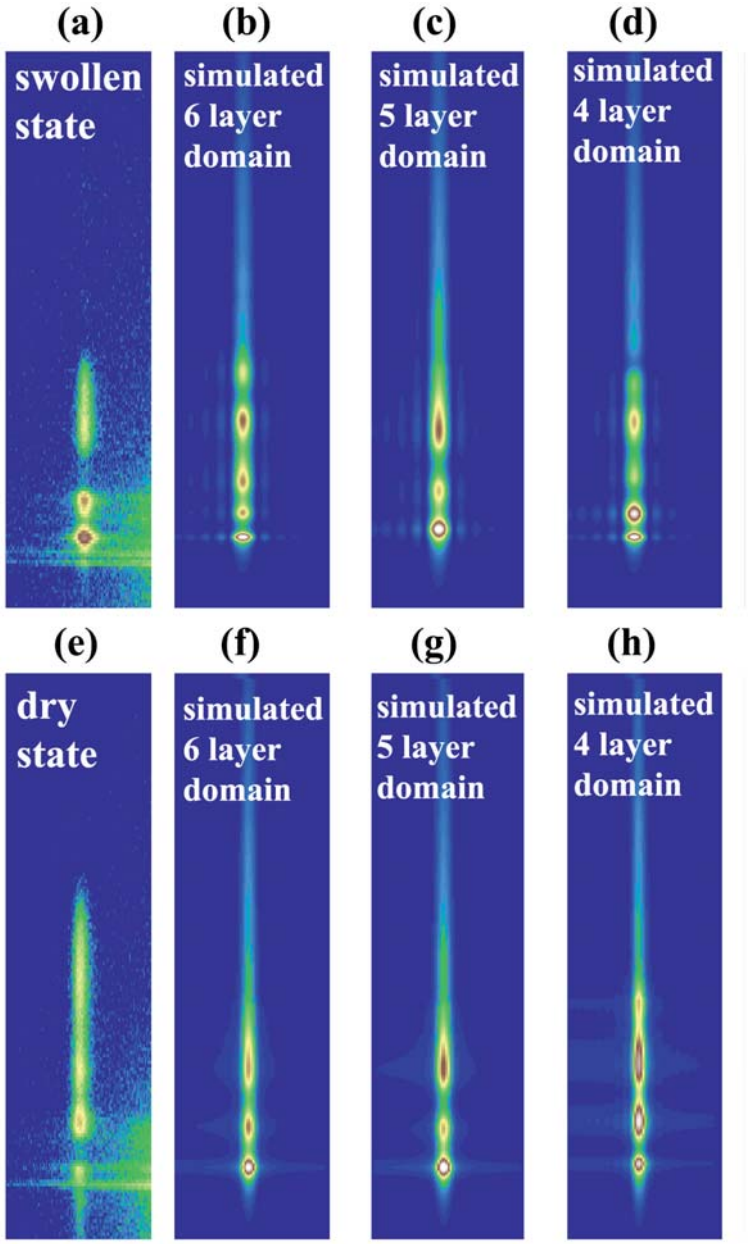

Figure 2.6 Comparison between experimental data, (a), (e), and simulated 2D GISAXS patterns of the first order reflection (b-d),(f-h). (a)-(d) correspond to the swollen state and (e)-(h) to the films after solvent removal.

2D GISAXS patterns were further analyzed by simulation in the framework of the Distorted-Wave Born Approximation (DWBA) using HipGISAXS to obtain information on the structure in the out-of-plane direction [51]. For the simulations a distribution for the domain spacing around 25 nm, a distribution for the grain size around 150 nm, and a cylinder diameter of 8 nm were used as input parameters. A different film thickness was used for the swollen film (125 nm) and the dried film (85 nm). To match the simulated GISAXS patterns with the experimental data we varied the number of layers in the out of plane direction. The simulations and experimental results are shown in Figure 2.6. For the swollen state we found good agreement between the simulated scattering profiles (Figure 2.6 c) and experimental data (Figure 2.6 a) for a film consisting of five layers of cylindrical microdomains oriented parallel to the substrate, while simulated patterns for films of four or six layer clearly deviated from the experimental data. Comparison of the experimental data for the swollen and the dried film (Figure 2.6 a,e) shows that solvent removal changed the microdomain structure in the out-of-plane direction as indicated by the change of relative peak positions in the qz direction. To account for these changes the distribution of the distances between different layers was varied in the simulations for the dried films. The simulated patterns corresponding to five layer and six layers (Figure 2.6 f,g) both agree with the experimental data (Figure 2.6 e) according to the relative peak positions. It should be noted that that the layers are uncorrelated, since the reflections characteristic of a hexagonal packing of cylindrical microdomains are not observed. The differences in the relative peak intensities can be due to an elliptical distortion of the cylindrical microdomains in the out-of-plane direction that was not accounted for in the simulations.

As discussed in this section, swelling of a BCP thin film in a neutral solvent not only reduces Tg of the BCP thin film, but also reduces the effective Flory-Huggins parameter, which is resulting in a faster kinetics of the self-assembly process[57].

2.3.2. SVA of BCP thin films: the process of solvent removal

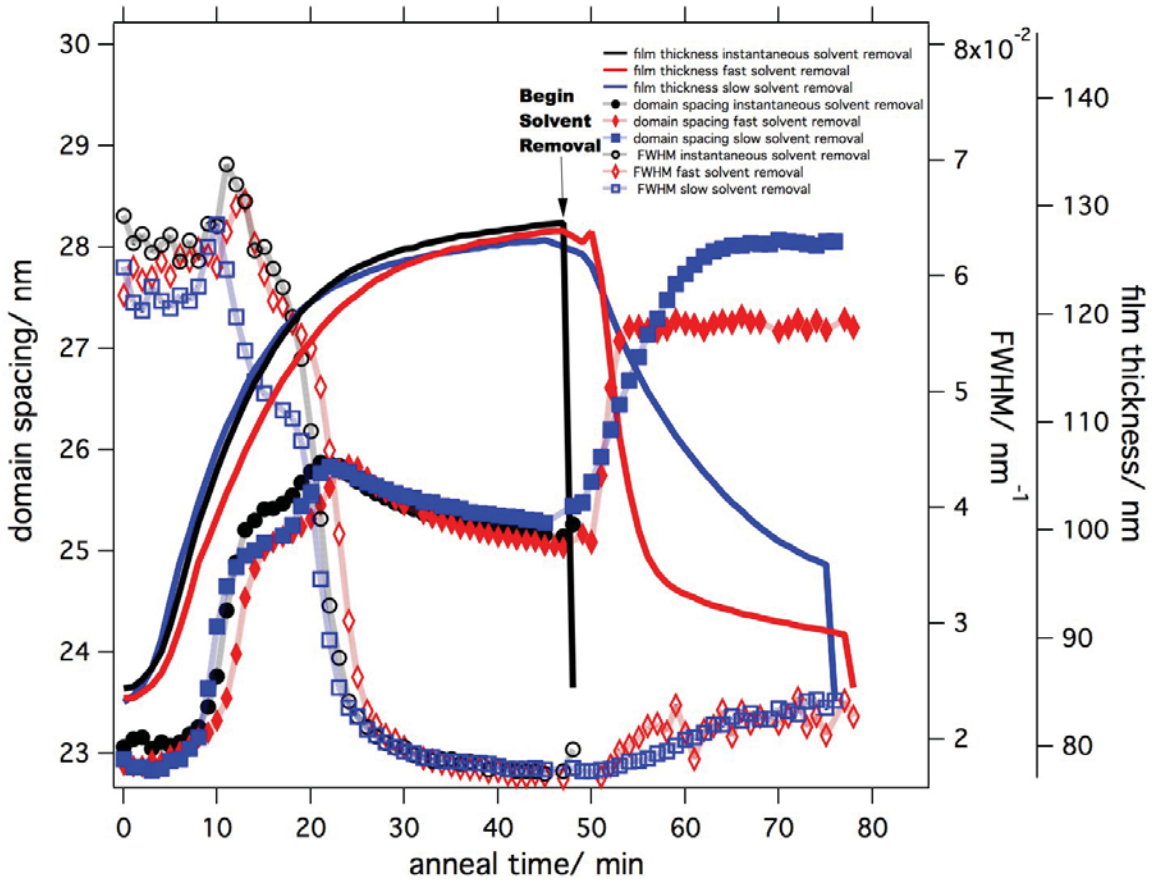

Figure 2.7 Results of *in situ* GISAXS experiments during SVA of BCP samples at three different solvent removal rates. Domain spacing, FWHM, film thickness (solid lines) vs. annealing time. The filled symbols correspond to the swelling, whereas the open symbols correspond to the solvent removal.

Furthermore, we studied the influence of the rate of solvent removal on the ordering of BCP microdomains. Three different BCP samples were annealed in THF for 45 min to a swelling ratio of ~1.53. The solvent was then removed from the chamber at

different rates. First, a very rapid removal of the solvent was achieved by opening the chamber top cover; the solvent vapor was removed within less than 1 sec. Two additional solvent removal rates were realized by flowing pure N_2 into the chamber at rates of 11.0 and 49.2 sccm, corresponding approximately to reductions in the swollen film thickness of 1 nm/min and 5 nm/min, respectively. The characteristics of the BCP microdomains for these three rates of solvent removal are shown in Figure 2.7. The data are coincident during the swelling, indicative of the reproducibility of the swelling process. When the solvent is very rapidly removed, the T_g of the film increases above room temperature almost instantly, kinetically trapping the morphology, where the lateral ordering of BCP thin film is the best. However, as shown, the period increases slightly and the FWHM increases, indicating that the BCP has undergone some re-organization and there is some disordering of the BCP microdomains. By controlling the rate of solvent removal with a nitrogen flow of 49.2 sccm, the domain spacing increases with increasing BCP concentration to a value of 27.2 nm when the film thickness was 105 nm or at a swelling ratio of 1.25, whereupon no further increase in the period was observed. The increase in the period results from an increase in the effective χ, which causes the BCP chains to stretch at the interface. At a swelling ratio of 1.25, the T_g of the swollen BCP films is ~5°C (assuming a uniform distribution of solvent in the film). However, since the concentration of solvent is lowest at the surface of the film, the T_g at the film surface will be well above room temperature, retarding changes to the morphology. Throughout the solvent removal process, the period and FWHM increase indicating a reorganization of the BCP microdomains as the solvent is removed. The competition between the rate of re-organization of the BCP microdomains and the increase in the T_g is reflected in the

larger period (27.2 nm) observed before re-organization ceases. At the lower nitrogen flow rate of 11.0 sccm, an even further relaxation of the BCP microdomains is observed. Again, at a swelling ratio of 1.25, changes in the period cease and a final, somewhat larger period (28.0 nm) were observed. The FWHM is not significantly different from that seen with the more rapid solvent removal rate, though both are larger than that found in the rapid solvent removal case, indicating more disordering were introduced to the BCP film at the slower solvent removal process.

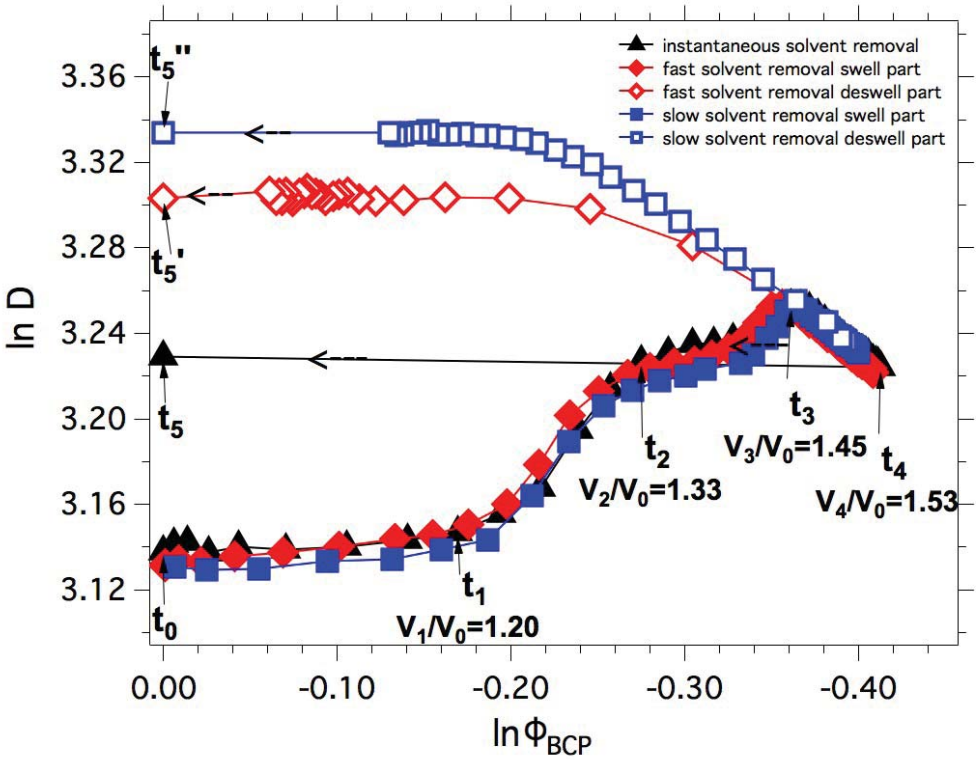

Figure 2.8 Domain spacing of PS-*b*-P2VP as a function of the volume fraction of the BCP in the swollen film for different solvent removal rates. The filled symbols correspond to the swelling, whereas the open symbols correspond to the solvent removal.

It was noted that the swelling of BCP film could be described by mean field arguments, coupled with modified dilution approximation in equation (2.4) by Lodge, for

a BCP in the weak segregation limit. As shown in Figure 2.8, these arguments also hold for the de-swelling process at the initial stages of solvent removal. In the log-log plot, as the solvent is removed, ln(D) varies linearly with ln(ϕ_{BCP}) down to a swelling ratio that depends on the solvent removal rate. The more rapid the solvent removal, the cooler will be the surface of the film, and the sooner will long-range motions cease, freezing in the morphology. For the two different solvent removal rates used, a power-law exponent of 0.64 is found, which is well within the range set in equation (2.7). Both the vitrification of the film and the shifting of the BCP from the weak to the strong segregation limit will cause deviations from this behavior.

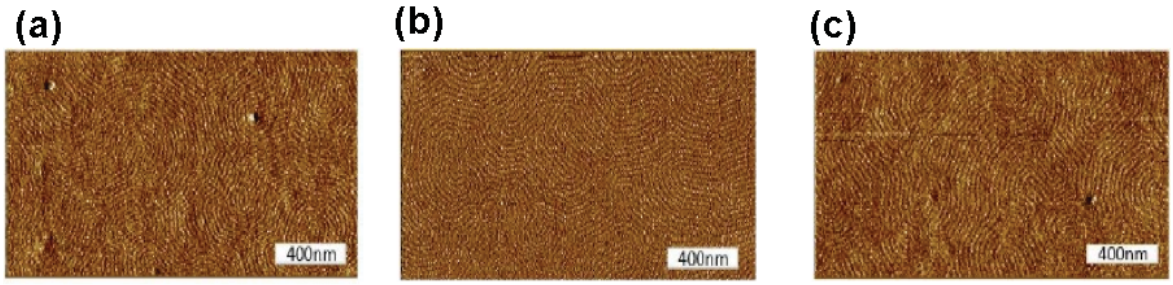

Figure 2.9 SFM Phase images of BCP thin films after SVA. (a) rapid solvent removal corresponding to t_5 in Figure 2.8, (b) nitrogen flow rate of 49.2 sccm (5 nm/min) corresponding to t_5' in Figure 2.8 and (c) nitrogen flow rate of 11.0 sccm (1 nm/min) corresponding to t_5'' in Figure 2.8.

The surface morphologies of the dried BCP samples, where the solvent removal rate was varied, were investigated by atomic force microscopy. The results of these studies are shown in Figure 2.9. In all cases, a fingerprint type of pattern was observed in the phase image, indicating that the cylindrical microdomains of P2VP are oriented parallel to the surface of the film. The corresponding height images showed some slight changes in the surface roughness. The spin coated film had an rms roughness of ~0.23

nm, while the films with decreasing rates of solvent removal (rapid, 5 nm/min and 1 nm/min) had roughness of 0.34, 0.58 and 0.68 nm, respectively. These results can be understood in terms of the time the BCPs are provided to re-organize during the solvent removal process. With the rapid solvent removal the best ordering was achieved where the samples were swollen and the rapid removal of the solvent froze-in this morphology. As the solvent is removed, non-favorable segmental interactions increase, the period of the microdomains increases, the extent to which the BCP chains are stretched at the interface increase, and the BCP must undergo a re-organization over the entire surface of the film to accommodate the incommensurability between the surface area and changing period of the BCP.

As swelling occurs, the thickness of the film increases linearly with the amount of solvent taken up in the film, placing an additional constraint on the systems due to the commensurability between the period of the swollen BCP microdomains and the swollen film thickness. Consequently, in addition to the changes in the period of the microdomains, topographic features must also appear during swelling, when the stretching of the BCP chains costs more energy than generating the additional surface area due to the topography. Islands are observed on the surface of the swollen film for high swelling ratios (>1.5). Interference optical microscopy measurements (see Figure 2.10) show the discrete surface topography with heights of $\sim\sqrt{3}/2\ L_0/SR$, where SR is the swelling ratio. For example, for a film with a thickness of 42nm ($\sim 1.5L_0$), the step height of the islands, on a film that was rapidly dried after swelling to an SR of 1.5, were 14.5 nm (see Figure 2.11). This value agreed well with the value of the step height according to $\sqrt{3}/2\ L_0/1.5=14.7$ nm.

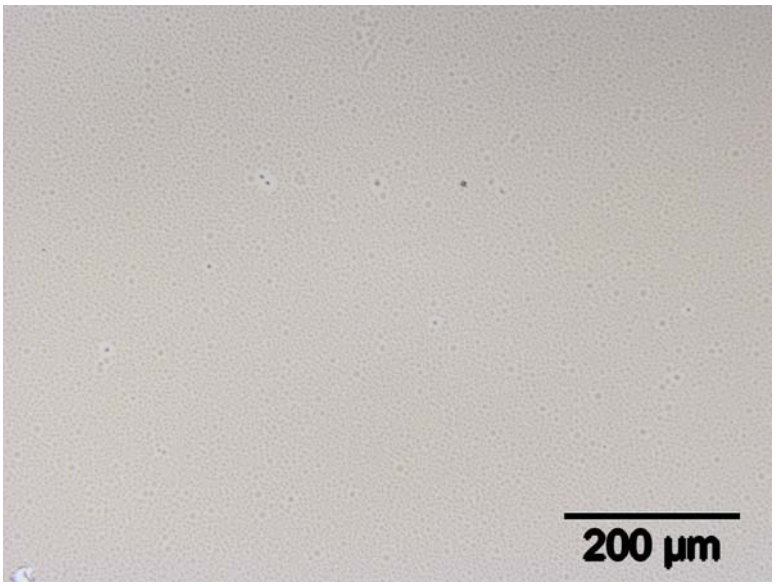

Figure 2.10 OM of 45nm thin film PS-*b*-P2VP annealed in THF with SR 1.5 for 1h.

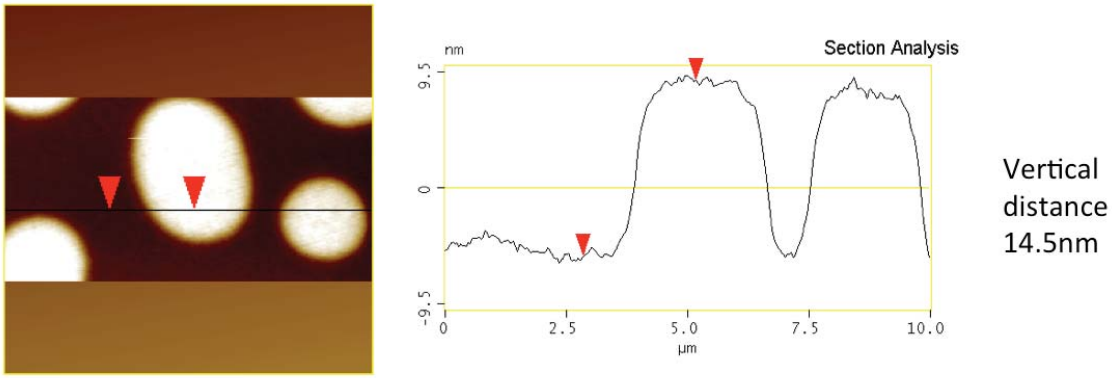

Figure 2.11 SFM Step height measurement of the islands formed by solvent vapor annealing.

2.3.3. SVA of BCP thin films: the influence of the processing history

The morphology of as-spun BCP thin film samples depends on the solvent used to prepare the polymer solution and coating methods[58]. A low boiling point solvent evaporates much faster during the coating process, thus the polymer chain has less time to relax, resulting in a kinetically trapped morphology. Park *et al.* reported that thin films

of poly(styrene-*block*-4-vinylpyridine) (PS-*b*-P4VP) dissolved in mixtures of toluene and tetrahydrofuran (THF) with different mixture ratio resulted in different micellar structures after coating on a silicon substrate[58]. Kim *et al.* found that the morphology of BCP thin films, having cylindrical microdomains oriented parallel or normal to the substrate, depends on the evaporation speed of solvent during the coating process of SBS thin films[59]. The influence of the processing history of a block copolymer thin film on its final morphology after SVA remains unclear. Here, we used *in situ* grazing incidence small-angle X-ray scattering (GISAXS) to investigate the ordering process of PS-*b*-P2VP 34k thin films with different processing histories during SVA. We studied BCPs both with initially disordered microdomains (as-spun film) and initially ordered microdomains (film after annealing in THF vapor).

Table 2.2 Different process histories for BCP PS-*b*-P2VP 34k

Sample name	PH-1	PH-2	PH-3
Processing history	As-spun PS-*b*-P2VP 34k film	As-spun PS-*b*-P2VP 34k film + SVA with instantaneous solvent removal	As-spun PS-*b*-P2VP 34k film +SVA with slow solvent removal

Three BCP thin film samples with same film thickness but different processing histories were studied here (see table 2.2). The first sample was an as-spun PS-*b*-P2VP thin film on a silicon substrate (PH-1). The second sample was a PS-*b*-P2VP thin film

spin coated onto a silicon substrate, subsequently annealed in THF for 1h to a swelling ratio (SR) of 1.5, and the solvent vapor was then removed instantaneously (PH-2). The last sample was a PS-*b*-P2VP sample spin coated onto silicon, subsequently annealed in THF for 1h at again a SR of 1.5, and then the solvent vapor was slowly removed from the sample at a solvent removal rate of 2nm/min from a film with a thickness of 95 nm in the swollen state (PH-3).

All samples were characterized by SFM and GISAXS before the *in situ* scattering experiment. As shown in Figure 2.12, the as-spun sample (PH-1) showed randomly oriented, microdomains with short-range ordering. During the spin coating process, solvent vapor evaporates rapidly, thus the polymer chain is kinetically trapped in its disordered state (Figure 2.12). This was further confirmed by GISAXS (Figure 2.13). As expected, the as-spun film showed only one broad Bragg peak with full width at half maximum (FWHM) of 6.2×10^{-2} nm^{-1}, indicating short ranged order of microdomains (Figure 2.13). Sample PH-2 showed ordered cylindrical microdomains oriented parallel to the substrate with a domain spacing of 26.1 nm (Figure 2.12c). The ordered state of the microdomain also is reflected by the relatively narrower FWHM ~ 2.6 $X10^{-2}$ nm^{-1} of the first order peak in the scattering data (Figure2.13). Sample PH-3 also showed ordered cylindrical microdomain oriented parallel to the substrate, but with a larger domain spacing of 27.8 nm compared to PH-2 (Figure 2.12e). Those three samples represent three different processing histories of PS-*b*-P2VP thin films, and were studied during SVA in THF by means of *in situ* GISAXS experiments.

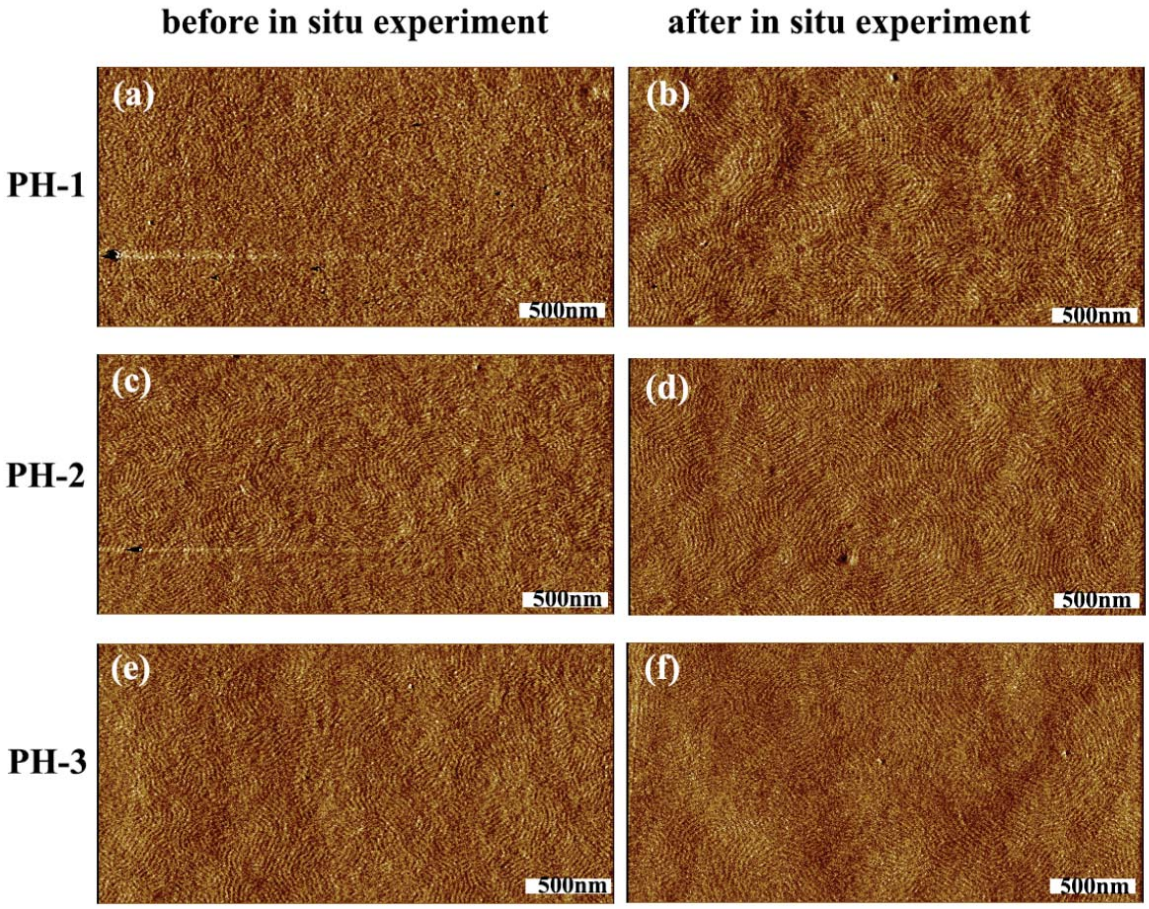

Figure 2.12 SFM images of samples with different processing history. Sample PH-1, before *in situ* experiment (a) and after *in situ* experiment (b). Sample PH-2, before *in situ* experiment (c) and after *in situ* experiment (d). Sample PH-3, before *in situ* experiment (e) and after *in situ* experiment (f).

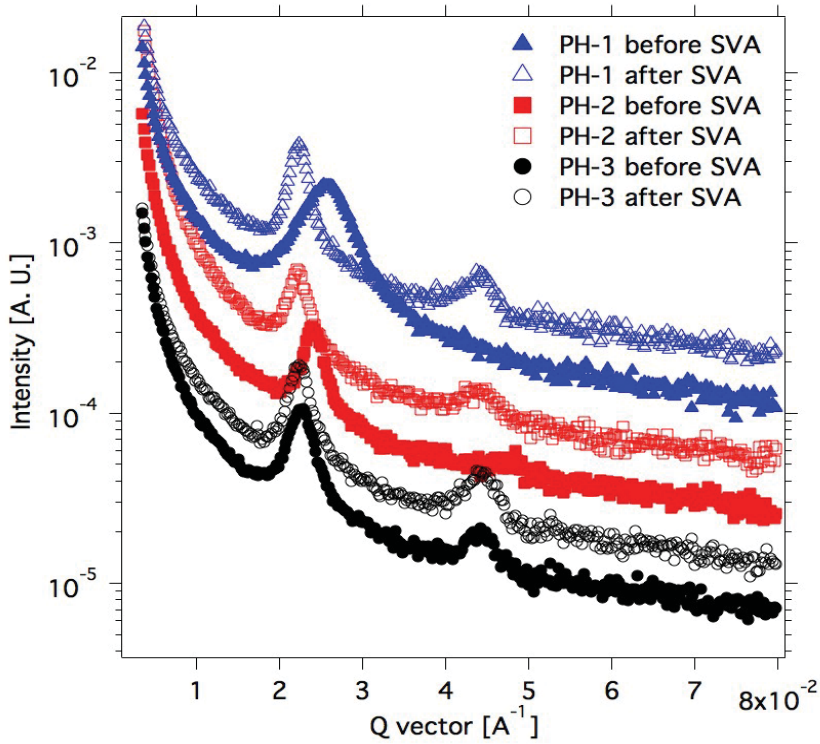

Figure 2.13 Scattering profiles of PS-*b*-P2VP with different processing history before and after SVA in THF.

All three samples were annealed in THF vapor to a swelling ratio of 1.47 for 30 min then followed by a slow solvent removal at a rate of 2.2 nm/min for 15 min (see Figure 2.15 for film thickness data). During the SVA, the scattering profiles of the swollen films were recorded by a two dimensional area detector and further analyzed using the fitting routing as described previously. The intensity profiles, I vs. q_y, are plotted for different annealing times in Figure 2.14.

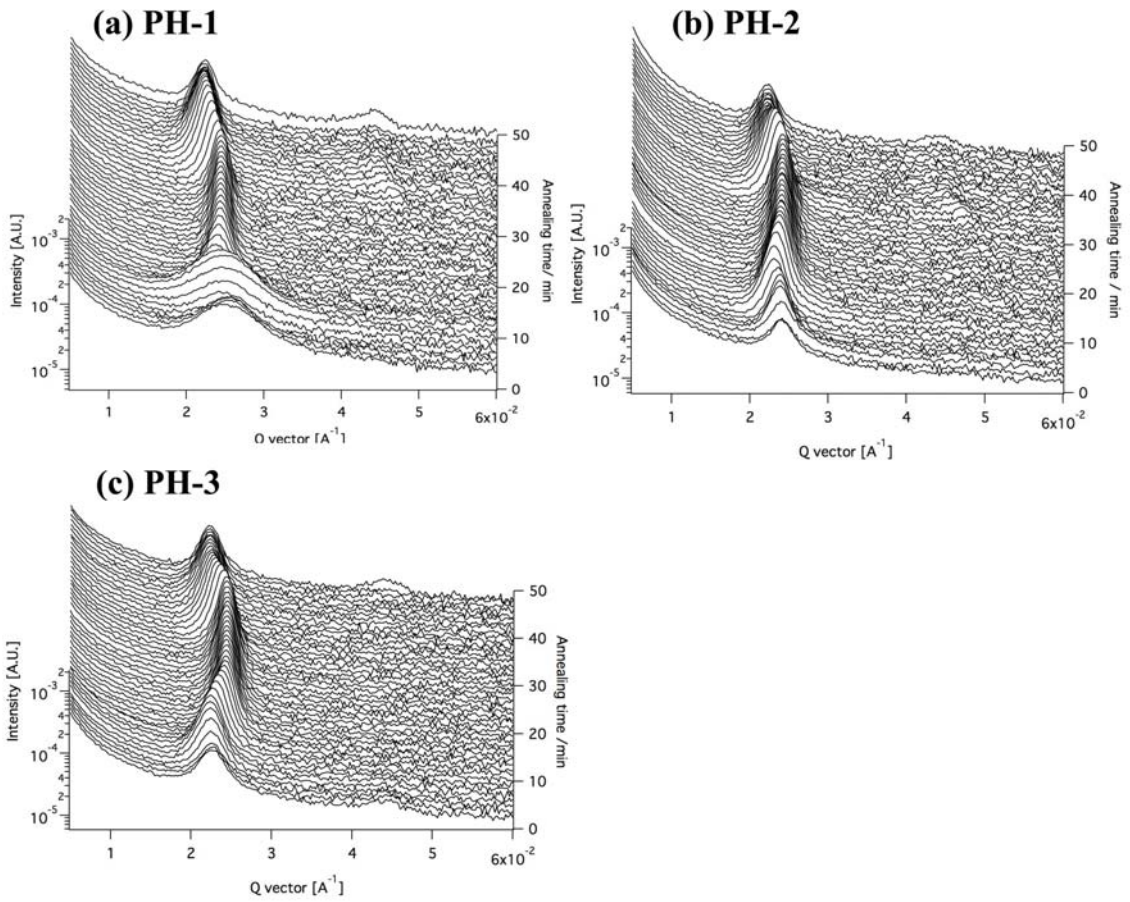

Figure 2.14 Temporal evolution of the in-plane scattering profiles for sample PH-1 (a), PH-2 (b), and PH-3(c). Data at different times were shifted vertically for clarity.

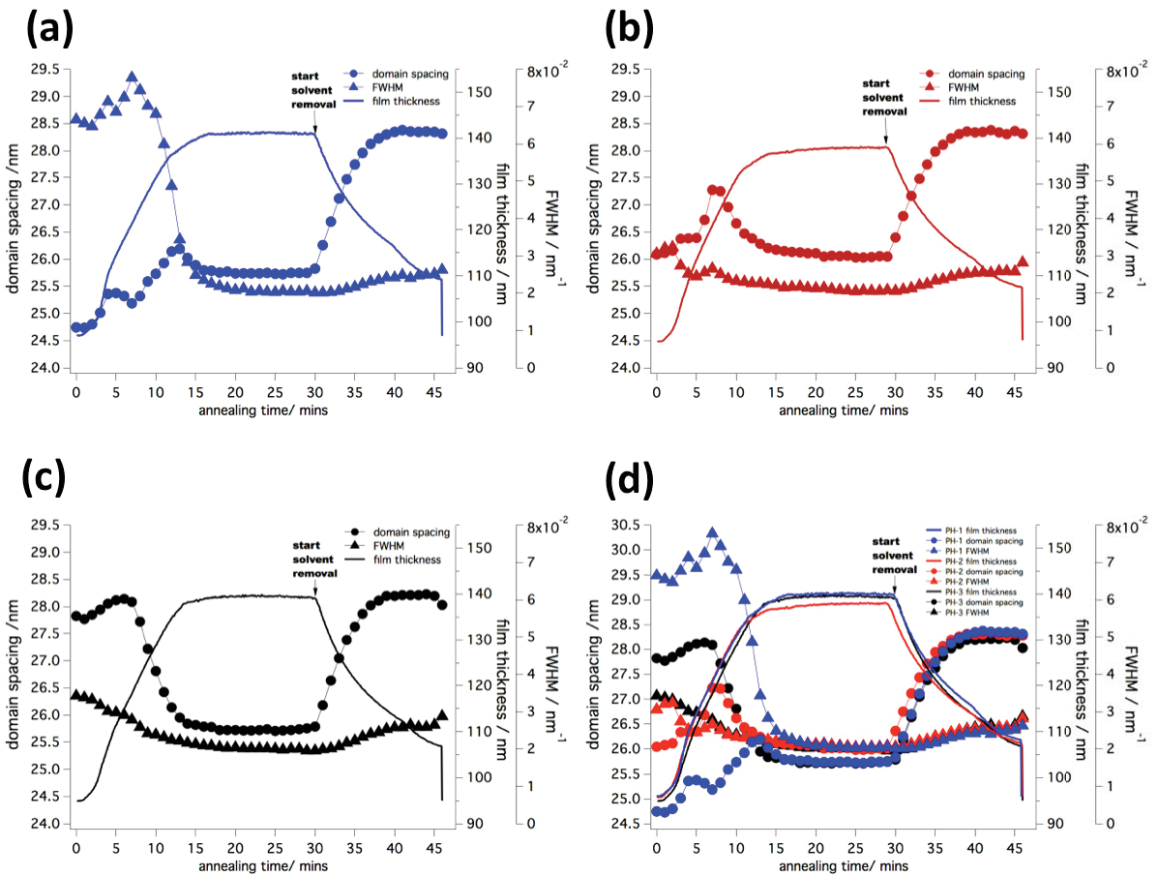

Figure 2.15 Results of *in situ* GISAXS experiments during SVA of BCP samples with different processing histories. Domain spacing, FWHM, and film thickness plotted vs. annealing time. (a) Sample PH-1, (b) Sample PH-2 (c) Sample PH-3 (d) All three samples plotted together.

The analyzed data, domain spacing, FWHM and film thickness, are plotted in Figure 2.15. Figure 2.15a revealed the ordering process for sample PH-1, an as-spun sample. The period of the microphase separated BCP increased initially during exposure to THF vapor (0~13 min), subsequently reached a maximum, and finally decreased. The period reached a plateau as soon as the changes in the film thickness ceased (13~30 min). By removing the solvent at a rate of ~ 2.2 nm/min, the period of the microphase separated morphology was found to increase with increasing block copolymer concentration, then it also plateaued at 28.2nm (31~45min). The ordering of PH-1 improves dramatically at

13min as indicated by a rapid drop of the FWHM from 7×10^{-2} nm^{-1} to 2×10^{-2} nm^{-1}. The drop of domain spacing arises from a screening of unfavorable interactions between the different blocks by the neutral solvent. Sample PH-2 retained its ordered cylindrical microdomains throughout the annealing process as indicated by a relatively low FWHM value (~ below 3×10^{-2} nm^{-1}). The domain spacing of the swollen polymer film also changed for different solvent concentrations in the swollen film for PH-2. During the annealing process, the domain spacing initially increased (0~7 min), and then decreased to a value of 25.8 nm. During the solvent removal process, PH-2 showed the same behavior as PH-1. The domain spacing increased continuously when solvent was removed from the swollen film until it reached a plateau (~28.2 nm). Sample PH-3 also had initially ordered microdomains as sample PH-2 but it showed a different behavior then PH-2 during swelling. During the initial swelling process (0~8 min), the domain spacing increased only slightly from 27.8 nm to 28.2 nm. After that, the domain spacing of the block copolymer kept dropping, when the swelling ratio was further increased, resulting in a decrease of the domain spacing value from 28.2 nm to 25.8 nm. During the deswelling process, the sample PH-3 showed the same behavior like samples PH-1 and PH-2. So the three samples considered here, showed different behavior between 0 to 15 min corresponding to a SR value lower than 1.4. At a SR of 1.4 (15min to 45mins) , all three samples showed almost identical behavior (Figure 2.15d).

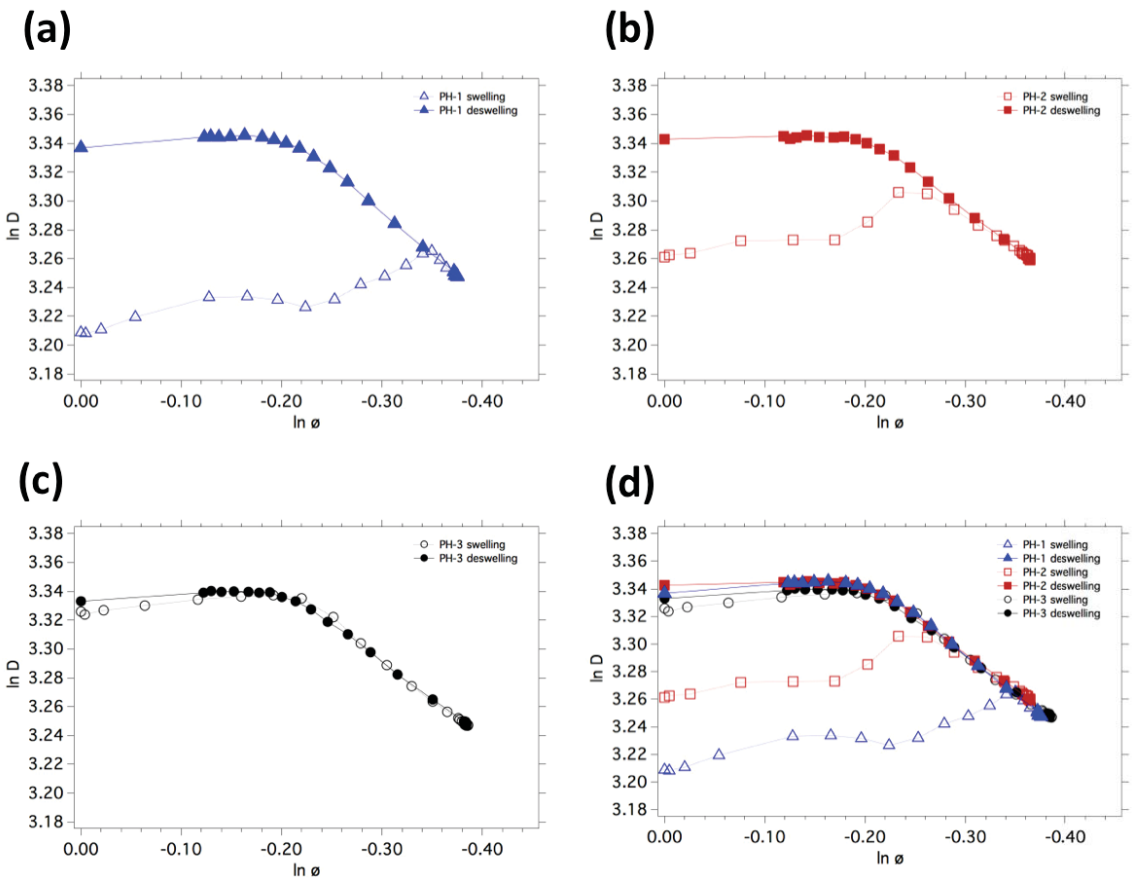

Figure 2.16 ln of domain spacing of as a function of the ln of the volume fraction of the BCP for different processing histories. (a) PH-1 as-spun film, (b) PH-2 SVA annealed with instantaneous solvent removal, (c), PH-3 SVA annealed with slowly solvent removal, (d) all samples plotted together. All the swelling data points are represented by open symbols, while the deswelling data are shown as solid symbols.

The domain spacing of a BCP swollen in a neutral solvent scales with the polymer concentration with an exponent of 0.64 as discussed in previous chapter. In Figure 2.16, the domain spacing and volume fraction of block copolymers in the swollen films for all three samples were plotted double-logarithmically. For all samples, the swelling process showed different trajectories of the data points (open symbol in Figure 2.16) during the initial stage of swelling process (0~15min), indicating the processing history was influencing the BCP morphology for SR below 1.4. This is related to the fact that polymer chains were kinetically trapped and could not reach the equilibrium morphology

in the time scale of the experiment. During the deswelling process, all three samples (solid symbol in Figure 2.16) showed the same trajectory, regardless of their different processing histories. This indicates that the processing history of the samples was erased, after swelling to a SR larger than 1.4. Interestingly, sample PH-3 showed reversible domain spacing trajectory during swelling and deswelling. During the swelling, the BCP concentration in a swollen film changes continuously, thus the effective Flory-Huggins parameter of BCP changes continuously, resulting in a change in the equilibrium domain spacing of the BCP. Since the sample PH-3 was prepared by swelling and a subsequent slow solvent removal, the initial domain spacing of PH-3 (27.8nm) before *in situ* GISAXS was close to its equilibrium domain spacing in the dry state (28.2nm). During the initial swelling, although PH-3 chain was kinetically trapped, the domain spacing of PH-3 was close to the equilibrium value of the swollen film. The sample PH-2 instead showed a different trajectory for the domain spacing for the swelling and deswelling process when the polymer concentration was larger than 0.77. Sample PH-2 was solvent annealed and the solvent was removed instantaneously, so the domain spacing for the PH-2 was trapped in 26.0 nm, which is far away from its equilibrium value (28.2nm) in the dry film. The Flory-Huggins parameter χ in the swollen and dry state differs by a factor of $\phi_{BCP}^{1.6}$, according to the dilution approximation[54,56]. During the first 8 min of SVA process, the domain spacing, being far away from the equilibrium, did not reach the equilibrium value because the film was kinetically trapped. After 8 min, when the BCP concentration below 0.77, the rearrangement of chain was fast enough for mobility required for reaching the equilibrium domain spacing. Note that the domain spacing is a function of the polymer concentration ϕ_{BCP} (8~30min), which is the origin of the merging

of swelling and deswelling curve. The PH-1 showed the largest discrepancy for the domain spacing during the swelling and deswelling SVA process among the three samples. The trajectory of the domain spacing during the swelling and deswelling did not merge until ϕ_{BCP} was smaller than 0.70. The sample PH-3 was further away from its equilibrium than PH-2. It was also observed that the increase in the period with increasing polymer concentration follows a power law behavior with an exponent of 0.62.

We studied the ordering process of BCP thin films with different processing histories by *in situ* GISAXS during SVA. The processing history was found to influence the domain spacing of a BCP only for small swelling ratio, when chains were kinetically trapped. At a higher swelling ratio, or faster chain kinetics, however, the processing history was erased and the morphology of the BCP sample was determined by the amount of swelling. In the case of a PS-*b*-P2VP with a molecular weight of 34 kg/mol, a swelling ratio >1.4 or polymer concentration smaller than 0.7, is required to give BCP chains enough mobility to remove the processing history of the film in the experiment time scale of 1h.

2.3.4. SVA of BCP thin films: the influence of molecular weights

BCP thin films with different molecular weights showed different kinetics. BCPs with the higher molecular weight diffuse more slowly in comparison BCPs of lower molecular weight BCPs. As a consequence, the formation of ordered microdomains in as spun BCP thin films of different molecular weight requires different annealing conditions in terms of annealing time and swelling ratio. Here, we study the influence of the molecular weight on the ordering of the BCP microdomains using a series of PS-*b*-P2VP

with different molecular weights. The PS-*b*-P2VP BCPs were selected as model system in this study. The molecular weight, volume fraction and polydispersity of the samples used here are listed in the table 2.3.

All BCP thin film samples were spin coated from the respect solutions to form uniform films with a thickness of 65 nm. The BCP thin film samples were annealed in the THF vapor to a SR high enough to drive the sample into the disordered state. Subsequently, the solvent vapors were slowly removed from swollen BCP film in a controlled manner. During the solvent removal process, the sample went through a disorder-order transition (DOT) and formed ordered cylindrical microdomains again. The in-situ X-ray scattering experiments were performed during the swelling and deswelling process. The scattering images were collect by 2-D area detector and further analyzed by fitting the first order in-plane scattering peak as described previous in this chapter.

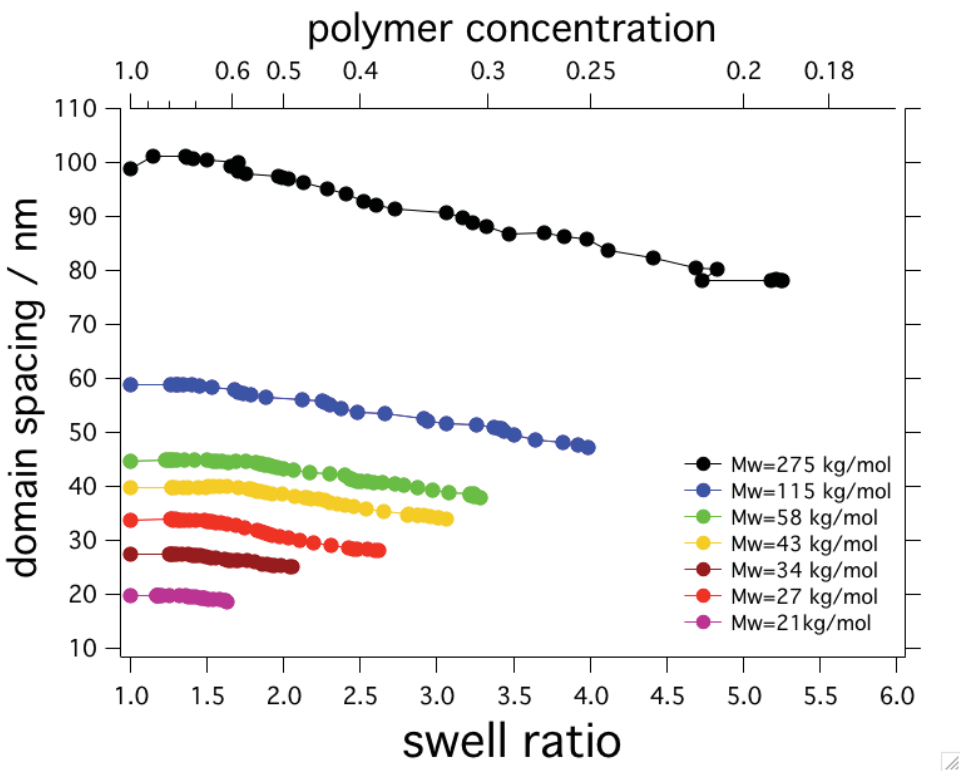

Figure 2.17 Domain spacing of PS-*b*-P2VP BCPs of different molecular weight vs. swelling ratio (polymer concentration) during annealing in THF. The data correspond to the deswelling with all BCPs being in the ordered state (corresponding to a cylindrical morphology in all cases).

Shown in Figure 2.17 is the domain spacing as a function of the swelling ratio, or polymer concentration, for PS-*b*-P2VP BCPs of different molecular weights in the ordered state during solvent removal. As expected, for each PS-*b*-P2VP BCP the values of the domain spacing decreased with increasing swelling ratio due to reduced the effective Flory-Huggins parameter. BCPs with higher molecular weight showed a larger domain spacing and their order-disorder transition occurred at higher values of the swelling ratio. BCPs with higher molecular weight were more immiscible since, $\chi_{dry}\phi_{BCP}^{\beta}N = constant$ at the ODT, a lower ϕ_{BCP}^{β} (higher swelling) is required to disorder the BCPs of higher molecular weight. The BCP with the highest molecular

weight used in this study, 275k PS-*b*-P2VP, has the strongest incompatibility and maintained microphase separated even at a swelling ratio up to ~6.05. During the solvent removal process for PS-*b*-P2VP 275k, the domain spacing measured by GISAXS, increased from 80 nm to 100 nm as a result of the continuously increasing χ_{eff} during deswelling. In contrast, the lowest molecular weight sample used in this study, PS-*b*-P2VP 22k BCP, showed ordered microdomains with a domain spacing of only 20 nm, and disordering already occurred at a swelling ratio of 1.68. This sample only showed a little increase in the values of the domain spacing from 18.8nm to 19.8nm during the deswelling process. All BCPs studied here, with molecular weights of 27 kg/mol, 34 kg/mol, 43 kg/mol, 58 kg/mol, and 115 kg/mol behaved similarly to PS-*b*-P2VP 22k and 275k, and the results are shown in Figure 2.17. Note that the BCP sample with a molecular weight of 27 kg/mol showed a larger domain spacing, 34nm, compared to the BCP sample with a molecular weight of 34 kg/ml, having a domain spacing of 27.5nm. The molecular weights of all PS-*b*-P2VP samples were determined by gel permeation chromatography (GPC). The results of these GPS measurements are listed in table 2.4. The PS-*b*-P2VP 27k indeed has a large molecular weight compared to PS-*b*-2VP 34k.

Table 2.3 SR and domain spacing at the order-disorder transition (ODT), and domain spacing at dry state for PS-*b*-P2VP BCPs with different molecular weights.

Polymer name	Polymer molecular weight kg/mol	SR at ODT	Domain spacing @ ODT /nm	Domain spacing @ dry film / nm
PS-*b*-P2VP 22k	14.8-*b*-6.5	1.68	18.8	19.8
PS-*b*-P2VP 27k	18.0-*b*-9.0	2.40	28.2	34

PS-*b*-P2VP 34k	23.6-*b*-10.4	2.14	25.1	27.5
PS-*b*-P2VP 43k	30.0-*b*-12.5	3.10	34	40
PS-*b*-P2VP 58k	40.0-*b*-18.0	3.33	38	45
PS-*b*-P2VP 115k	79.0-*b*-36.5	4.03	48	59
PS-*b*-P2VP 275k	185.0-*b*-90.0	6.05	75	100

Table 2.4 Number-average (Mn) and weight-average (Mw) molecular weights of PS-*b*-P2VP*

Polymer name	Polymer molecular weight kg/mol	Mw measure by GPC kg/mol	Mn measure by GPC kg/mol
PS-*b*-P2VP 22k	14.8-*b*-6.5	27	33
PS-*b*-P2VP 27k	18.0-*b*-9.0	61	74
PS-*b*-P2VP 34k	23.6-*b*-10.4	51	62
PS-*b*-P2VP 43k	30.0-*b*-12.5	94	110
PS-*b*-P2VP 58k	40.0-*b*-18.0	90	114
PS-*b*-P2VP 115k	79.0-*b*-36.5	180	220
PS-*b*-P2VP 275k	185.0-*b*-90.0	300	430

*GPC measurement of BCP sample.

PS-*b*-P2VP BCPs with different molecular weights undergo an order disorder transition (ODT) at different polymer concentrations, which is a result of a constant incompatibility, $\chi_{eff}N$, at the ODT according to Leibler theory, in combination with the (modified) dilution approximation, which can be summarized as follows[60],

$$\chi_{eff}N = \chi_{dry}\phi_{BCP}^{\beta}N = constant \tag{2.8}$$

thus,

$$\phi \sim N^{-1/\beta} \tag{2.9}$$

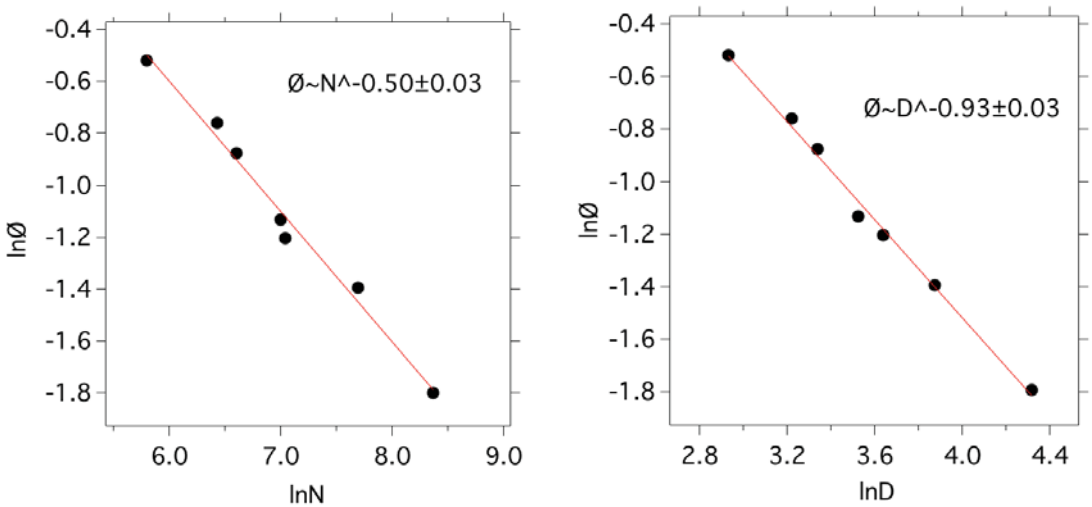

Figure 2.18 (a) ln-ln plot of the BCP concentration ϕ at ODT vs. the degree of polymerization N (Mw measured by GPC), and ln-ln plot of the BCP concentration ϕ at ODT vs. domain spacing D of the BCP.

The relation between the polymer concentration and the molecular weight for various PS-*b*-P2VPs are plotted in the Figure 2.18 in the ln-ln scale. Our experiment results showed that $\phi \sim N^{-0.50}$. This does not follow the dilution approximation described by Lodge et al., where the observed β=2.0 is slightly larger than 1.3 and 1.6 as they

reported. The polymer concentration at ODT is plotted against domain spacing in Figure 2.18b. Our experiment results showed that $\phi \sim D^{-0.93}$.

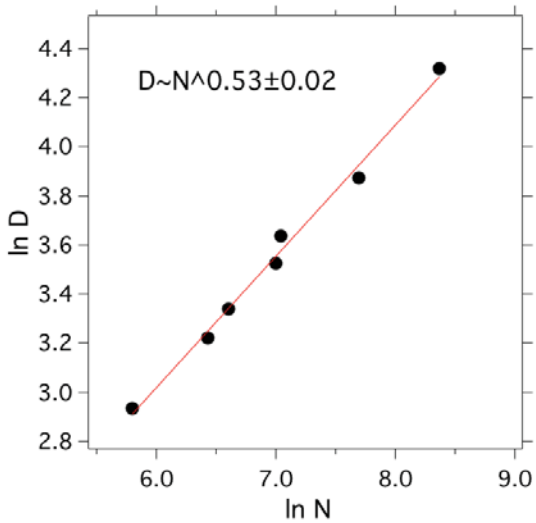

Figure 2.19 ln-ln plot of domain spacing vs. the repeating unite of the BCP thin film

The domain spacing of the BCP scales with the molecular weight of the BCP as predicted by mean field theory[60]. As the BCP reaches the ODT, the polymer chain can be described as a Gaussian chain, and thus the domain spacing D scales with the repeat unit or the molecular weight as $D \sim N^{0.5}$, which agrees well with the experimental finding shown in Figure 2.19. The experimental result shows D scales with N as follows:

$$D \sim N^{\wedge 0.53 \pm 0.02} \tag{2.10}$$

An interesting phenomenon observed during the *in situ* GISAXS is that the PS-*b*-P2VP with large molecular weights underwent an order-order transition (OOT) during the swelling process. Shown in Figure 2.20 are the representative 2-D scattering images of the PS-*b*-P2VP 115k during the OOT. The cylindrical BCP microdomains change

their orientation from being perpendicular to the substrate, with peak ratios: q*:√3q, to being parallel to the sample surface (peak ratio q*:2q*:3q*). This switch in the orientation of cylindrical microdomains was further confirmed by SEM measurements. The BCP sample was annealed *ex-situ* using the same conditions as for the *in situ* experiments. One sample was annealed in THF to a swelling ratio below the critical swelling ratio at the OOT, while the other sample was swollen above the critical swelling ratio at the OOT. In both cases the solvent was removed instantaneously to freeze in the microstructure and orientation of the microdomains in the swollen films. Figure 2.21 shows the surface topography of the BCP samples before and after OOT. As the SEM images clearly show, the sample showed dominantly perpendicularly oriented cylindrical microdomains before crossing the OOT, where the cylindrical microdomains locally packed in hexagonal lattices (Figure 2.21a). After crossing the OOT, the cylindrical microdomain changed their orientation and showed an orientation parallel to the substrate (Figure 2.21b). The perpendicular orientation of the BCP microdomains at the lower swelling ratio is a result of the limited diffusion of the polymer chains at the relatively higher value of Tg at the lower solvent concentration. The perpendicular orientation of microdomains provides an advantage of chain diffusion along the cylindrical interface in the out of the plan direction. Further experiments are needed to understand this phenomenon.

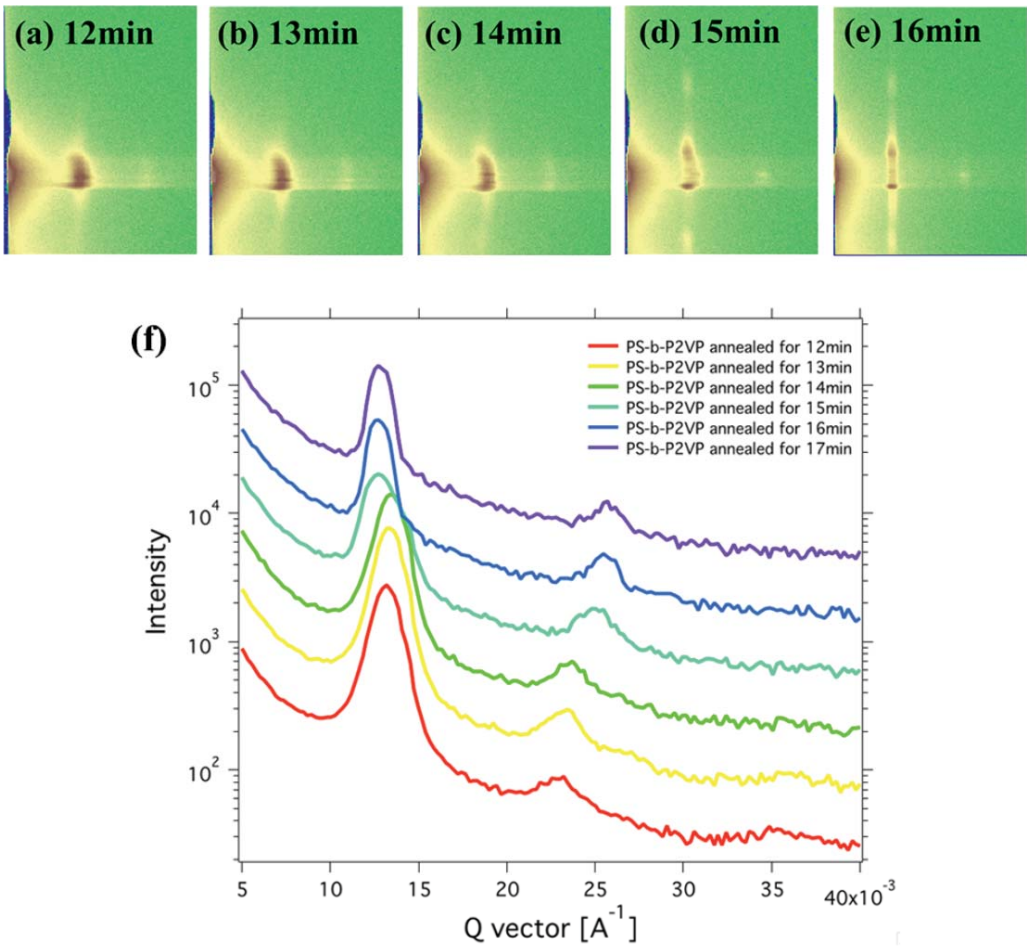

Figure 2.20 (a~e) 2-D X-ray scattering patterns of PS-*b*-P2VP 115k thin film with respect to different solvent vapor annealing time. (f) 1-D scattering profile of the BCP during the OOT

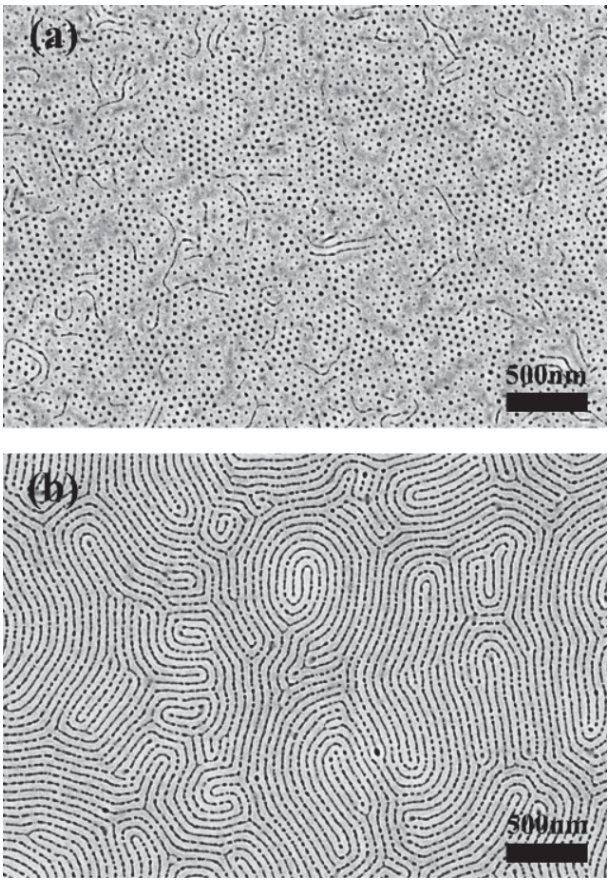

Figure 2.21 SEM images of the PS-*b*-P2VP 115k before OOT (a) and after OOT (b).

The experiments discussed above show that the SVA conditions necessary to achieve similarly ordered microstructures in BCPs with different molecular weights are different. Annealing conditions in terms of the values of the swelling ratio cannot be simply transferred between polymers of different molecular weight due to the different kinetics in BCPs of different molecular weights. Generally, BCPs with higher molecular weights require a higher swelling ratio, or lower polymer concentration, to form well-ordered microdomains after SVA. The concentration for BCP at ODT is predicted by the equation 2.9.

$$\phi \sim N^{-1/\beta} \tag{2.9}$$

The β was observed with a value of 2 in this experiment.

2.3.5. SVA of BCP thin films: comparison of SVA with thermal annealing

Both SVA and thermal annealing are widely used to produce films with well-ordered BCP microdomains. Detailed studies directly comparing both techniques in real time, however, have not been carried out. Here, we studied the effects of thermal annealing of a PS-b-P2VP 34k BCP and compared the results with the SVA process that we discussed earlier. Thin film samples for thermal annealing were prepared in the same way as previously used for SVA by spin coating. *In situ* thermal annealing was carried out in a custom designed thermal annealing chamber, where the BCP sample was placed onto a heating block with the temperature being controlled by a Watlow temperature controller. Nitrogen gas was used to continuously purge the chamber to create an inert environment, which is required to protect the PS-*b*-P2VP from degradation during the thermal annealing. A control experiment was carried out without the inert nitrogen gas atmosphere. In this experiment a degradation of the BCP was observed during the GISAXS experiments.

The BCP samples were first heated up to allow for the formation of ordered microdomains and then further heated to temperatures where the disordered state was observed. After holding the sample at 290 ^{0}C in its disordered state for 5mins the sample was slowly cooled down to room temperate at a rate of 10 degree/min. The heating profile of the BCP thin film is shown in the Figure 2.23 (b).

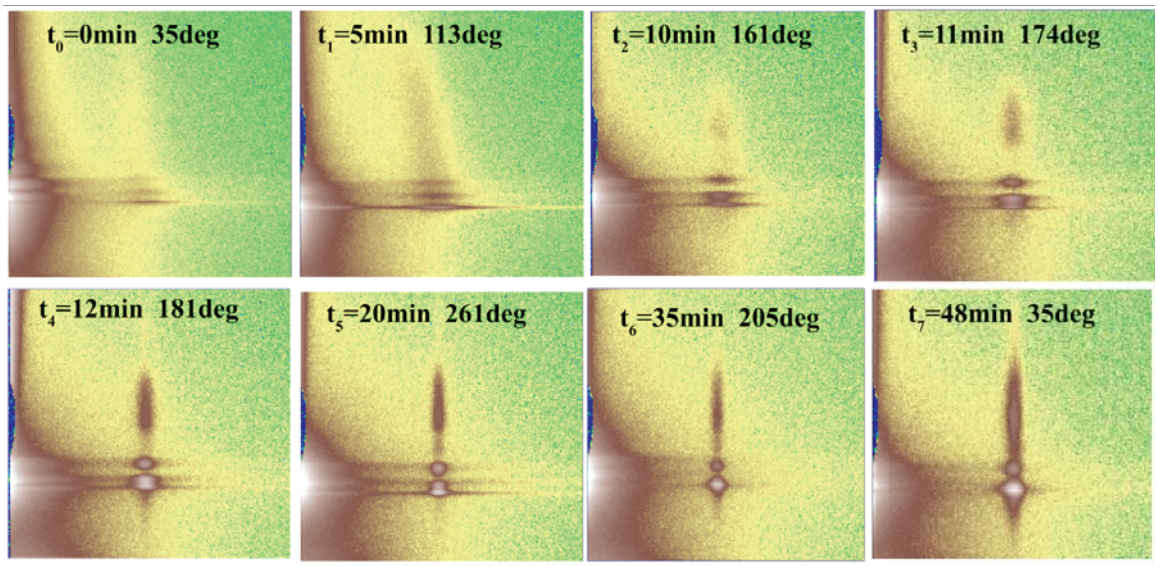

Figure 2.22 Representative 2-D scattering profile of the BCP during the *in situ* scattering experiment.

2-D scattering pattern of PS-*b*-P2VP 34k during the process of thermal annealing were recorded by a 2-D area detector and representative frames are shown in Figure 2.22. The scattering profiles are plotted as a function of time and shown in Figure 2.23 a. The thermal annealing process generally is very similar to the solvent vapor annealing. The as spun sample showed little or no ordering. With sample heated above its glass transition temperature, (c.a. 100 ^{0}C), the BCP chains have enough mobility to rearrange itself, as reflected in the change of the domain spacing. The BCP were heated further, and a disorder to order transition was observed at 10min. A sharpening of the primary scattering peak was observed. With further thermal annealing, the first order scattering became sharper and also shifted to higher values of q range (smaller domain spacing). Similar to solvent vapor annealing, the reduction of the domain spacing is a result of the reduced Flory-Huggins parameter, χ. The temperature dependence of the Flory-Huggins segmental interaction parameter of PS-*b*-P2VP in the bulk (dry) was reported as [57]:

$$\chi_{dry} = \frac{63}{T} - 0.033 \tag{2.3}$$

As temperature increase, the χ_{dry} is reduced.

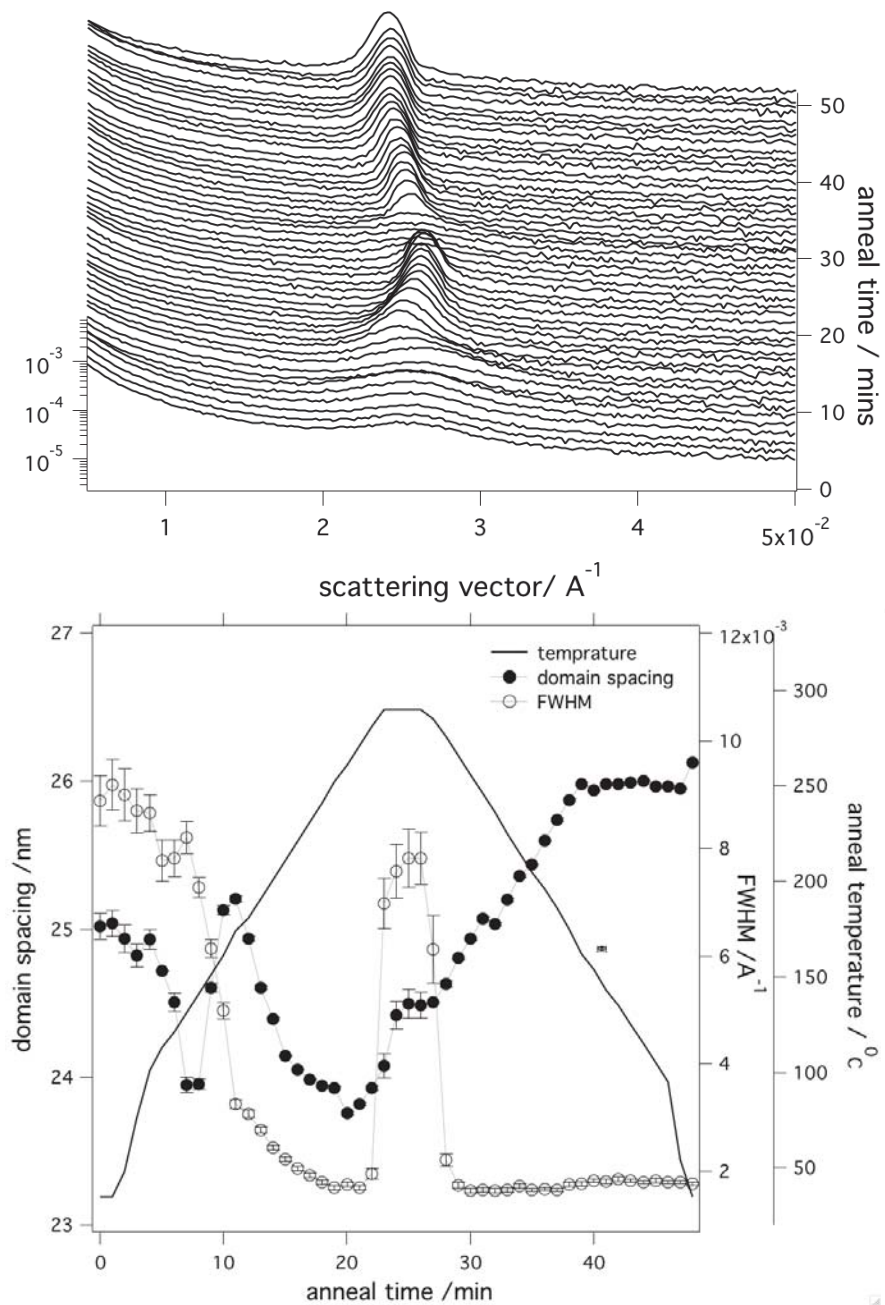

Figure 2.23 (a) Scattering profiles at different times. (B) analyzed data from the data shown in (a), temperature, domain spacing, and FWHM were plotted as a function of time.

As the temperature was further increased, the disorder-order transition (ODT) of PS-*b*-P2VP (Mn=34k) took place at about 280 ^{0}C, as indicated by a sharp increase in

FWHM. Then, during the process of cooling at 25mins, the sample underwent a disorder-order transition, and cylindrical microdomains oriented parallel to the substrate were formed, as later confirmed by SEM measurements. Opposite to the heating process, χ_{dry} increased and also the values of domain spacing increased during cooling (Figure 2.23). With further cooling, the kinetics of the BCP chain is significantly reduced. The domain spacing of the BCP remained unchanged at temperatures below 160 degree.

Thermal annealing is very similar to solvent vapor annealing in neutral solvents. In both processes the chain mobility is enhanced, either by increasing the temperature of the BCP film in case of the thermal annealing, or by reducing the Tg of the BCP film by adding small molecules, and more importantly, the reduction of the Flory-Huggins parameter.

In case of thermal annealing, the system reaches equilibrium at elevated temperatures, which is similar to the swollen BCP by a neutral solvent. For applications, however, the sample needs to be cooled down to room temperature. During cooling χ increases, and as a consequence the domain spacing of the BCP increases. The BCP film, however, is confined onto the silicon substrate, which introduces incommensurability issues between the changing domain spacing and film thickness in the BCP thin film, as in the case of solvent vapor annealing.

Ex situ thermal annealing experiments of PS-*b*-P2VP 34k and 58k BCP samples were carried out using the thermal annealing chamber at different temperatures with the BCP samples slowly cooled down after thermal annealing. After thermal annealing, all samples were reconstructed in ethanol and etched in oxygen RIE and then imaged by SEM. The SEM images of the BCP samples are shown in Figure 2.24. The PS-*b*-P2VP

34k sample annealed at 190 ^{0}C only showed a small grain size of about 100 nm. At higher annealing temperature of 250 ^{0}C the grain size of the BCP were greatly increased to 2500 nm. For PS-*b*-P2VP 58k BCPs, the sample annealed at 190 degree Celsius showed no improvement on the lateral ordering as compared to the as-spun film. The sample annealed at 250 ^{0}C only showed a small grain size of about 100 nm. These results indicate that the grain size of the thermally annealed BCPs is inversely proportional to the $\chi_{eff}N$, same as for the SVA.

.

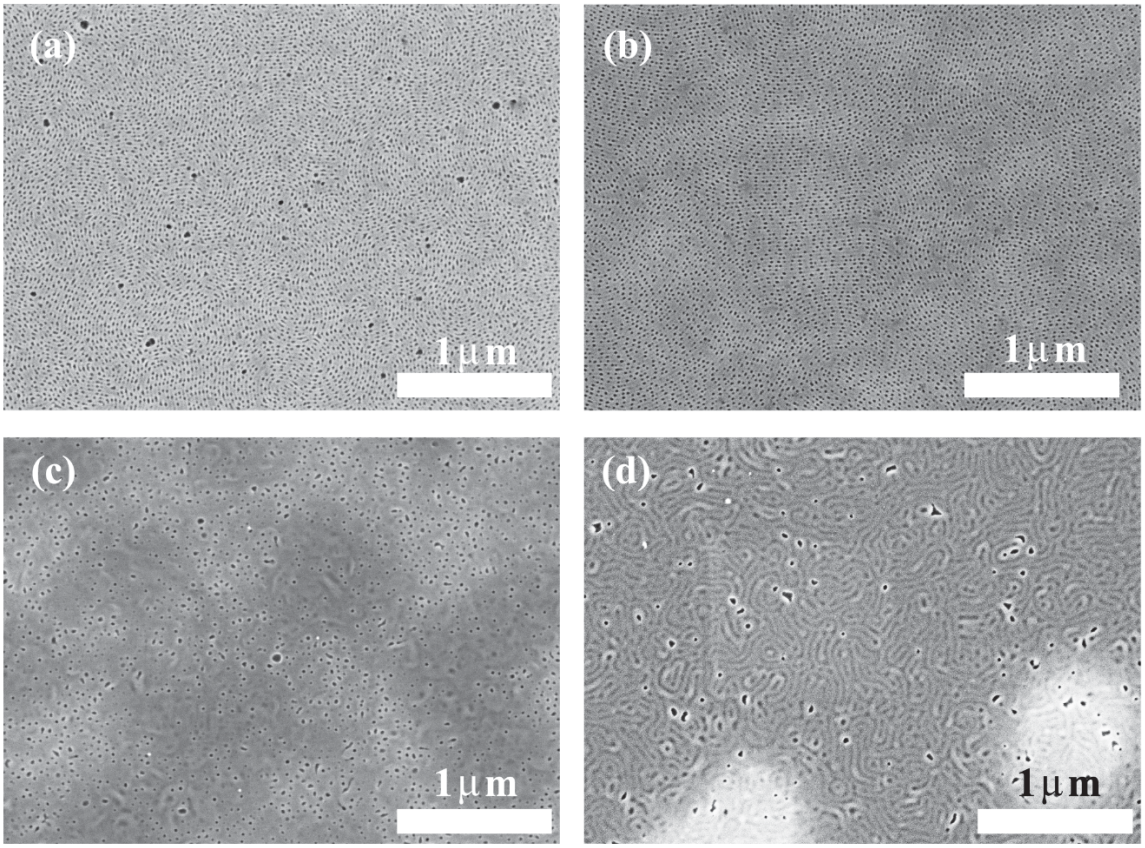

Figure 2.24 SEM images of PS-*b*-P2VP thermally annealed at different temperatures. (a) PS-*b*-P2VP 34k and (c) PS-*b*-P2VP 58k annealed at 190deg for 1 hour. (b) PS-*b*-P2VP 34k and (d) PS-*b*-P2VP 58k annealed at 250deg for 1 hour.

Both the thermal annealing and solvent vapor annealing of the BCPs are accompanied by

a reduction of Flory-Huggins parameters, either by an increased temperature or by screening of unfavorable interaction by the neutral solvents. The reduced of Flory-Huggins parameters greatly enhance the chain mobility and enhance the lateral ordering of BCP microdomains. But the range of the χ_{eff} observed in the thermal annealing experiment is very limited compared to range of χ_{eff} in solvent vapor annealing experiments due to thermal degradation of the BCP thin film at higher temperatures. In PS-*b*-P2VP BCPs, for example, 400 ^{0}C is the typical upper limit for the annealing temperature. However, χ only reduces from 0.175 at room temperature to 0.060 when sample heated to 400 ^{0}C (Figure 2.25a). In case of solvent vapor annealing, on the other hand, a swelling ratio of 2 effectively reduces χ to 0.060, which corresponds to heating the sample to 400 ^{0}C (Figure 2.25b). A direct comparison of the χ of thermal annealing and effective χ solvent vapor annealing is shown in the (Figure 2.25c). It is clear that solvent vapor annealing in neutral solvent covers a much broad range of χ_{eff}, e.g. χ_{eff} is only 0.012 when SR is 6, thus making the SVA more versatile to change χ_{eff} for PS-*b*-P2VP. It is also possible to design and synthesis BCPs with χ strongly depends on the temperature, so that the χ can be more effectively reduced at elevated temperature.

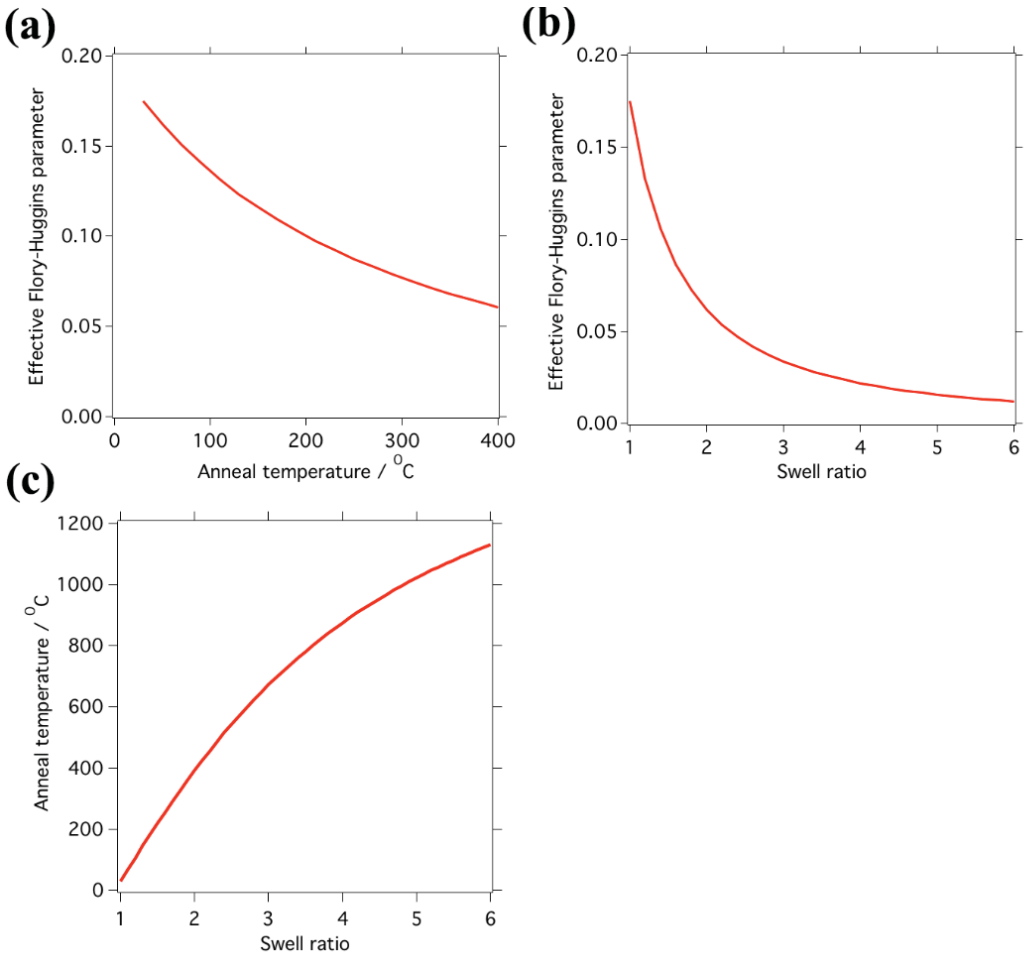

Figure 2.25 (a) Flory-Huggins parameter at different temperatures during thermal annealing of PS-*b*-P2VP (based on equation 2.3) (b) Effective Flory-Huggins parameter of PS-*b*-P2VP swelled at different SR in a neutral sovlent during solvent vapor annealing (based on equation 2.4, and β is taken as 1.5) (c) plot of annealing temperature and SR at the same effective Flory-Huggins parameter

2.3.6. SVA of BCP thin films: grain size at different swell ratio

To examine the growth of the BCP microdomains, PS-*b*-P2VP 34k BCP was solvent vapor annealed in THF to a swelling ratio controlled by the vapor pressure of the solvent in the same chamber used for the GISAXS studies. The temperature for these studies was slightly lower (ca 20 ^{0}C) than that used for the GISAXS studies which will

enhance the swelling of the BCP film. After the BCP thin film solvent were SVA in THF for 1hour, the solvent was removed rapidly by venting the chamber to air.

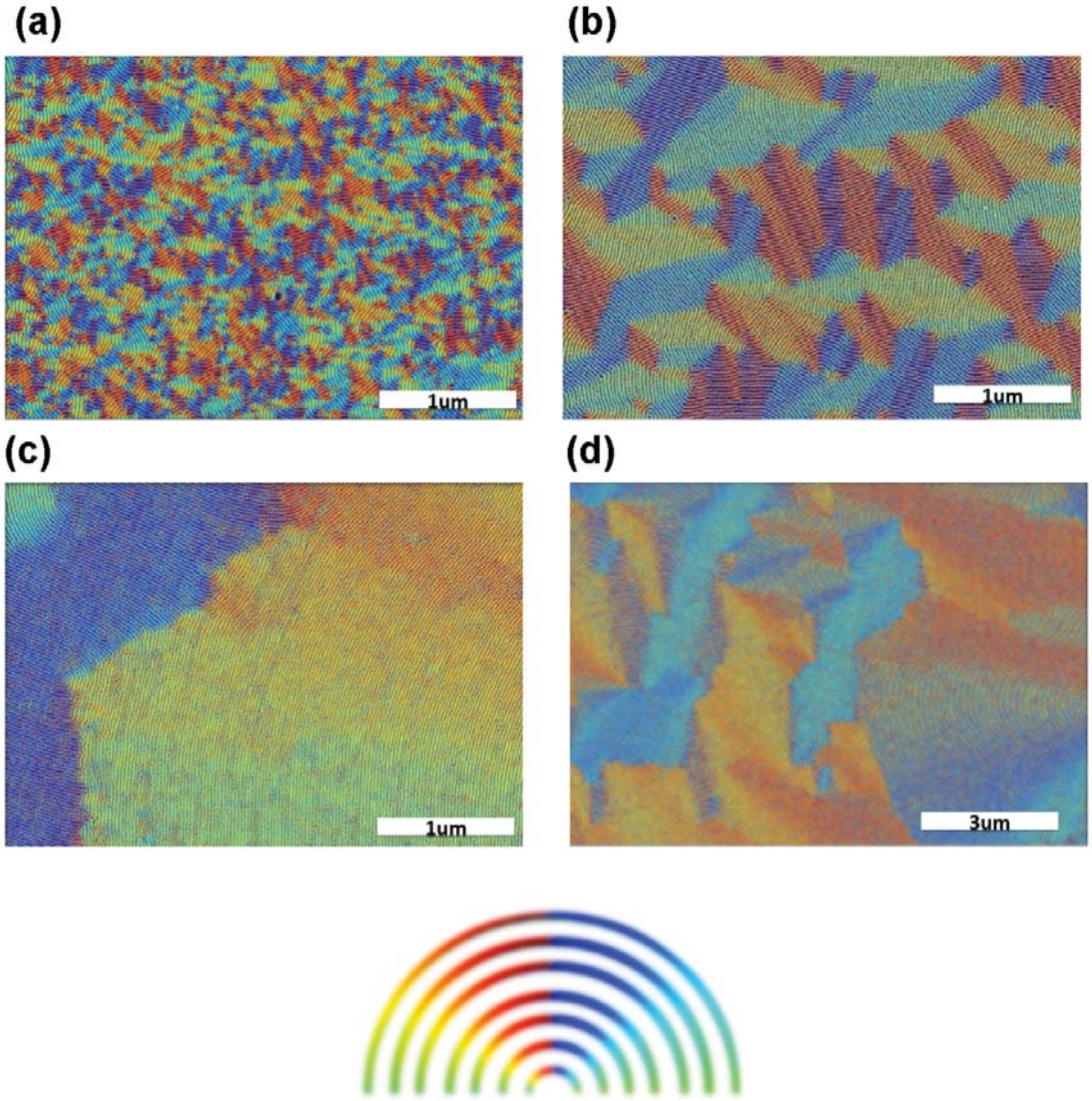

Figure 2.26 Colorized grains in the BCP microdomain structure for different swelling ratios: (a) 1.3, (b) 1.5, (c) 1.7 and (d) 1.7 (enlarged). Color wheel is shown at bottom of image.

The influence of the degree of swelling on the grain size is shown in Figure 2.26. With increasing solvent concentration or swelling ratio, the grain size was observed to

increase. The data shown in Figure 2.26 show are colorized according to the orientation of the cylindrical microdomains. After one hour at a swelling ratio of 1.3, the average grain size was ~100nm (Figure 2.26a), indicative of relatively short range ordering. The grains are seen to be anisotropic in shape, approximating an ellipse with the major axis of the ellipse oriented orthogonal to the axes of the microdomains. The average ellipticity (ratio of the minor to major axis) of the grains is ~0.5. By increasing the swelling ratio to 1.5 (Figure 2.26b), the average grain size has increased to ~500nm and the average elipticity is ~0.6, indicating an increase in the ordering normal to the cylinder axes and also an increase in the length of the cylinders before encountering a grain boundary. If the swelling ratio is increased to 1.7, the average grain size increased to ~2 um with an average ellipticity of ~0.8. The observation that the grain sizes are larger at higher solvent concentrations, i.e. smaller χ_{eff}N, is somewhat surprising, as one would expect larger grains with stronger segregation where defects cost more energy. This observation indicates that for a complete theoretical description one also needs to take into account the increased chain mobility at higher solvent concentration when predicting grain sizes in BCP thin films patterns after SVA. It should also be noted that many of the grain boundaries are less well-defined with only a slight change in the orientation from one grain to the next. This is more evident in the zoomed-out image. If the swelling ratio is increased to 1.9, the concentration of solvent is sufficiently high to drive the BCP into the disordered state. In fact, a closer examination of the data for a swelling ratio of 1.7 shows that the integrity of the cylindrical microdomains is beginning to be compromised, due to the proximity of the order-to-disorder transition.

2.4. Conclusions

In this chapter, we presented a detailed in-situ GISAXS study of SVA of PS-*b*-P2VP in a near neutral solvent.

During SVA, solvent molecules diffuse into the BCP thin film, which results in the plasticization of the film, i.e. a decrease of the Tg of the BCP below room temperature. More importantly, SVA leads to a lower effective Flory-Huggins parameter of the BCP in the swollen film due to a screening of unfavorable interactions between blocks by the solvent molecules at the interface. As a result, the periodicity of the microdomains is reduced and the chain kinetics is greatly enhanced. The strength of unfavorable interactions between different blocks, $\chi_{eff}N$, not only determines the kinetics of the BCP chains, but also the grain size of the BCP in both SVA and thermal annealing. It is not clear at this point why $\chi_{eff}N$ is inverse proportional to the grain size BCPs in the ordered state.

χ_{eff} strongly depends on the polymer concentration in the swollen film. Thus, for a specific BCP a certain swelling ratio is required that is related to the specific interaction parameter χ and molecular weight, N of this BCP. For a relatively low swelling ratio, $\chi_{eff} * N \gg (\chi * N)_{ODT}$, the system is kinetically arrested, where only limited lateral order of microdomains could be achieved in the experiment time scale, ~ hours. In the other extreme, if $\chi_{eff} * N < (\chi * N)_{ODT}$, the system undergoes an ODT and no microphase separated structure will be formed. Only a certain range of $\chi_{eff}N$, which is close to χN_{ODT}, gives an optimal condition for the self-assembly process of a BCP during SVA. Thus, it is impossible to reproduce the SVA annealing experiments, performed in a different laboratory without specific values of the swelling ratio provided, which we

encourage to become common practice in SVA reports in refereed journals.

The solvent removal rates are critical for preserving the well ordered microdomain structures observed in the swollen states of BCP thin films. Quenching the ordered swollen film with high degrees of lateral order traps the ordered microdomain structure, and preserves the maximal the degree of order. A slow solvent removal results in changes of the domain spacing, thus creates an incommensurability issue since the BCP thin film is confined onto the silicon substrate. Ideally, the well ordered BCP microdomains need to be cross-linked, before the solvents is removed to preserve the degree of lateral order of the microdomain in the swollen state, given that the cross-linked BCPs have enough mechanical strength to maintain its integrity.

2.5. References

(1) Cheng, J.; Ross, C.; Chan, V.; Thomas, E.; Lammertink, R.; Vancso, G. *Adv Mater* **2001**, *13*, 1174–1178.

(2) Park, M.; Harrison, C.; Chaikin, P. M.; Register, R. A.; Adamson, D. H. *Science* **1997**, *276*, 1401–1404.

(3) Thurn-Albrecht, T.; Schotter, J.; Kästle, G. A.; Emley, N.; Shibauchi, T.; Krusin-Elbaum, L.; Guarini, K.; Black, C. T.; Tuominen, M. T.; Russell, T. P. *Science* **2000**, *290*, 2126–2129.

(4) Gu, X.; Liu, Z.; Gunkel, I.; Chourou, S. T.; Hong, S. W.; Olynick, D. L.; Russell, T. P. *Adv Mater* **2012**, *24*, 5688–5694.

(5) Chai, J.; Wang, D.; Fan, X. N.; Buriak, J. M. *Nat. Nanotechnol.* **2007**, *2*, 500–506.

(6) Gu, X.; Dorsey, P.; Russell, T. P. *Adv Mater* **2012**, *24*, 5505–5511.

(7) Cheng, J. Y.; Ross, C. A.; Thomas, E. L.; Smith, H. I.; Vancso, G. J. *Appl. Phys. Lett.* **2002**, *81*, 3657–3659.

(8) Jackson, E. A.; Hillmyer, M. A. *ACS nano* **2010**, *4*, 3548–3553.

(9) Yang, S. Y.; Ryu, I.; Kim, H. Y.; Kim, J. K.; Jang, S. K.; Russell, T. P. *Adv Mater* **2006**, *18*, 709–712.

(10) Ruiz, R.; Kang, H.; Detcheverry, F. A.; Dobisz, E.; Kercher, D. S.; Albrecht, T. R.; de Pablo, J. J.; Nealey, P. F. *Science* **2008**, *321*, 936–939.

(11) Bita, I.; Yang, J. K. W.; Jung, Y. S.; Ross, C. A.; Thomas, E. L.; Berggren, K. K. *Science* **2008**, *321*, 939–943.

(12) Segalman, R. A.; Yokoyama, H.; Kramer, E. J. *Adv Mater* **2001**, *13*, 1152–1155.

(13) Kim, S. O.; Solak, H. H.; Stoykovich, M. P.; Ferrier, N. J.; de Pablo, J. J.; Nealey, P. F. *Nature* **2003**, *424*, 411–414.

(14) Park, S.; Lee, D. H.; Xu, J.; Kim, B.; Hong, S. W.; Jeong, U.; Xu, T.; Russell, T. P. *Science* **2009**, *323*, 1030–1033.

(15) Gu, W.; Huh, J.; Hong, S. W.; Sveinbjornsson, B. R.; Park, C.; Grubbs, R. H.; Russell, T. P. *ACS nano* **2013**, *7*, 2551–2558.

(16) Kim, E.; Ahn, H.; Park, S.; Lee, H.; Lee, M.; Lee, S.; Kim, T.; Kwak, E.-A.; Lee, J. H.; Lei, X.; Huh, J.; Bang, J.; Lee, B.; Ryu, D. Y. *ACS nano* **2013**, *7*, 1952–1960.

(17) Stafford, C. M.; Russell, T. P.; McCarthy, T. J. *Macromolecules* **1999**, *32*, 7610–7616.

(18) Helfand, E.; TAGAMI, Y. *The Journal of chemical physics* **1972**, *56*, 3592–3601.

(19) Lai, C.; Russel, W. B.; Register, R. A. *Macromolecules* **2002**, *35*, 4044–4049.

(20) Wang, J. Y.; Chen, W.; Roy, C.; Sievert, J. D.; Russell, T. P. *Macromolecules* **2008**, *41*, 963–969.

(21) Kim, S. H.; Misner, M. J.; Xu, T.; Kimura, M.; Russell, T. P. *Adv Mater* **2004**, *16*, 226–231.

(22) Shibayama, M.; Hashimoto, T.; Hasegawa, H.; Kawai, H. *Macromolecules* **1983**, *16*, 1427–1433.

(23) Albalak, R. J.; Capel, M. S.; Thomas, E. L. *Polymer* **1998**, *39*, 1647–1656.

(24) Mori, K.; Hasegawa, H.; Hashimoto, T. *Polymer* **2001**, *42*, 3009–3021.

(25) Mori, K.; Okawara, A.; Hashimoto, T. *The Journal of chemical physics* **1996**, *104*, 7765.

(26) Kim, G.; Libera, M. *Macromolecules* **1998**, *31*, 2670–2672.

(27) Lin, Z. Q.; Kim, D. H.; Wu, X. D.; Boosahda, L.; Stone, D.; LaRose, L.; Russell, T. P. *Adv Mater* **2002**, *14*, 1373–1376.

(28) Jung, Y. S.; Ross, C. A. *Nano Lett.* **2007**, *7*, 2046–2050.

(29) Jung, Y. S.; Ross, C. A. *Adv Mater* **2009**, *21*, 2540–2545.

(30) Jeong, J. W.; Park, W. I.; Kim, M.-J.; Ross, C. A.; Jung, Y. S. *Nano Lett.* **2011**, *11*, 4095–4101.

(31) Tang, C.; Lennon, E. M.; Fredrickson, G. H.; Kramer, E. J.; Hawker, C. J. *Science* **2008**, *322*, 429–432.

(32) Albert, J. N. L.; Bogart, T. D.; Lewis, R. L.; Beers, K. L.; Fasolka, M. J.; Hutchison, J. B.; Vogt, B. D.; Epps, T. H. *Nano Lett.* **2011**, *11*, 1351–1357.

(33) Seppala, J. E.; Lewis, R. L., III; Epps, T. H., III. *ACS nano* **2012**, *6*, 9855–9862.

(34) Bosworth, J. K.; Paik, M. Y.; Ruiz, R.; Schwartz, E. L.; Huang, J. Q.; Ko, A. W.; Smilgies, D.-M.; Black, C. T.; Ober, C. K. *ACS nano* **2008**, *2*, 1396–1402.

(35) Knoll, A.; Horvat, A.; Lyakhova, K.; Krausch, G.; Sevink, G.; Zvelindovsky, A.; Magerle, R. *Physical Review Letters* **2002**, *89*, 035501.

(36) Knoll, A.; Lyakhova, K. S.; Horvat, A.; Krausch, G.; Sevink, G. J. A.; Zvelindovsky, A. V.; Magerle, R. *Nature Materials* **2004**, *3*, 886–891.

(37) Albert, J. N. L.; Young, W.-S.; Lewis, R. L., III; Bogart, T. D.; Smith, J. R.; Epps, T. H., III. *ACS nano* **2012**, *6*, 459–466.

(38) Horvat, A.; Knoll, A.; Krausch, G.; Tsarkova, L.; Lyakhova, K. S.; Sevink, G. J. A.; Zvelindovsky, A. V.; Magerle, R. *Macromolecules* **2007**, *40*, 6930–6939.

(39) Smilgies, D.-M.; Busch, P.; Papadakis, C. M.; Posselt, D. *Synchrotron Radiation News* **2002**, *15*, 35–42.

(40) Papadakis, C. M.; Di, Z.; Posselt, D.; Smilgies, D.-M. *Langmuir* **2008**, *24*, 13815–13818.

(41) Di, Z.; Posselt, D.; Smilgies, D.-M.; Papadakis, C. M. *Macromolecules* **2010**, *43*, 418–427.

(42) Di, Z.; Posselt, D.; Smilgies, D.-M.; Li, R.; Rauscher, M.; Potemkin, I. I.; Papadakis, C. M. *Macromolecules* **2012**, *45*, 5185–5195.

(43) Paik, M. Y.; Bosworth, J. K.; Smilges, D. M.; Schwartz, E. L.; Andre, X.; Ober, C. K. *Macromolecules* **2010**, *43*, 4253–4260.

(44) Cavicchi, K. A.; Berthiaume, K. J.; Russell, T. P. *Polymer* **2005**, *46*, 11635–

11639.

(45) Kim, S. H.; Misner, M. J.; Yang, L.; Gang, O.; Ocko, B. M.; Russell, T. P. *Macromolecules* **2006**, *39*, 8473–8479.

(46) Cavicchi, K. A.; Russell, T. P. *Macromolecules* **2007**, *40*, 1181–1186.

(47) Kim, S. H.; Misner, M. J.; Russell, T. P. *Adv Mater* **2008**, *20*, 4851–4856.

(48) Sinturel, C.; Vayer, M.; Morris, M.; Hillmyer, M. A. *Macromolecules* **2013**, *46*, 5399–5415.

(49) Gotrik, K. W.; Hannon, A. F.; Son, J. G.; Keller, B.; Alexander-Katz, A.; Ross, C. A. *ACS nano* **2012**, *6*, 8052–8059.

(50) Ilavsky, J. *J Appl Crystallogr* **2012**, *45*, 324–328.

(51) Chourou, S. T.; Sarje, A.; Li, X. S.; Chan, E. R.; Hexemer, A. *J Appl Cryst* **2013**, 1–15.

(52) Russell, T. P.; Mayes, A. M.; Kunz, M. S. In *Ordering in Macromolecular Systems*; Springer Berlin Heidelberg: Berlin, Heidelberg, 1994; pp. 217–223.

(53) Fox, T. G.; Loshaek, S. *J. Polym. Sci.* **1955**, *15*, 371–390.

(54) Lodge, T. P.; Hanley, K. J.; Pudil, B.; Alahapperuma, V. *Macromolecules* **2003**, *36*, 816–822.

(55) Shull, K. R. *Macromolecules* **1992**, *25*, 2122–2133.

(56) Lodge, T. P.; Pan, C.; Jin, X.; Liu, Z.; Zhao, J.; Maurer, W. W.; Bates, F. S. *J. Polym. Sci. B Polym. Phys.* **1995**, *33*, 2289–2293.

(57) Dai, K. H.; Kramer, E. J. *Polymer* **1994**, *35*, 157–161.

(58) Park, S.; Wang, J. Y.; Kim, B.; Chen, W.; Russell, T. P. *Macromolecules* **2007**, *40*, 9059–9063.

(59) Kim, G.; Libera, M. *Macromolecules* **1998**, *31*, 2569–2577.

(60) Leibler, L. *Macromolecules* **1980**, *13*, 1602–1617.

CHAPTER 3

PATTERN TRANSFER FROM SELF-ASSEMBLED BLOCK COPOLYMER MICRODOMAINS TO SILICON WITH SUB-10NM RESOLUTION

3.1. Introduction

Photolithography has been the mainstay for meeting the demand for continuous shrinkage in the semiconductor industry, but it is facing limitations for sub-30 nm patterning[1]. Block copolymer (BCP) lithography has emerged as a promising low-cost, high throughput alternative. A block copolymer consists of two or more polymeric chains, which are chemically different and covalently attached to each other. BCPs can microphase separate into periodic arrays of nanostructures, including spherical, cylindrical, lamellar, and gyroid morphologies, depending on the volume fractions of the constituent blocks.[2] The molecular weight ultimately defines the size scale of the structures, with typical sizes in the tens to sub-ten nanometer range where microdomains as small as 3 nm have been demonstrated.[3] BCPs are emerging as very promising scaffold and template platforms for the fabrication of nanostructured materials and are already finding use for magnetic recording, semiconductors and dielectric insulators.

With BCP lithography, one of the blocks must be removed or there must be sufficient etching contrast so that pattern transfer can be realized with high fidelity. Dry etching is the preferred method to remove polymers, as it is generally more controllable and generates less waste. Furthermore, it avoids capillary-induced pattern collapse of

small polymer features and general shifting of features that can occur with wet processing.[4,5] To use BCPs for high resolution lithography, two different patterning selectivities must be considered. First, there is the etching contrast between the different blocks of the BCP, and second, there is the etching rate difference between the BCP mask and the underlying substrate. To achieve high etching selectivity, numerous studies have described the complexation of one block with a heavy element (e.g Si or Fe) containing BCP or complexation heavy metal into one block of BCPs. Mansky[6] *et al.*, first demonstrated the idea of using BCPs for lithographic purposes. Later, Park[7] *et al.*, showed that, by using ozone cleaning or osmium tetraoxide (OsO_4) staining, the microdomain morphologies of polystyrene-*block*-polybutadiene (PS-*b*-PB) or polystyrene-*block*-polyisoprene (PS-*b*-PI) could be transferred to the underlying silicon nitride substrate by etching. In the case of poly(styrene-*block*-2-vinylpyridine) (PS-*b*-P2VP), P2VP can be complexed with metal ions to enhance the etching contrast.[8,9] Peng *et al*.,[10,11] enhanced the contrast by infiltrating the PMMA microdomains of polystyrene-*block*-poly(methyl methacrylate) (PS-*b*-PMMA) with a trimethylaluminum (TMA) gas precursor. Tseng[12] *et al.,* futher improved the sequential infiltration process to demonstrate using PS-*b*-PMMA template to pattern high aspect ratio (~10:1) silicon trench. Subsequently, Russell and coworkers showed that the BCP template could be backfilled with PDMS to generate silicon oxide nanodots to enhance the contrast.[13,14] For polystyrene-*block*-polyferrocenylsilane (PS-*b*-PFS)[15-17] and polystyrene-*block*-polydimethylsiloxane (PS-*b*-PDMS) [18-21], direct pattern transfer is possible due to the inherent etching contrast between the blocks of the BCP. The downside of this approach is that the mask removal process must be aggressive and often leaves behind

contamination. The alternative approach is to remove one block (usually the minor component block) and directly pattern into the underlying substrate. For example, the PMMA block in PS-*b*-PMMA diblock copolymers can be removed by degradation of the PMMA block with UV to generate a porous film in direct contact with the substrate. Alternatively, with PS-*b*-PMMA, an O_2 or CHF_3 and O_2 mixture gas reactive ion etching (RIE) dry process can be used to remove the PMMA block. [4,22,23] Nonetheless, as the size scales of the features decrease, the thickness of the BCP film also decreases and any steps that can be taken to enhance the contrast is desirable and soon will be a necessity to achieve pattern transfer with a high fidelity.

In this Chapter, we use a solvent reconstruction process to enhance the etch contrast between two organic blocks, where the BCP film is placed in a good solvent for the minor block that is also a bad solvent for the matrix block. If the microdomains are oriented normal to the surface, upon drying, the minor component block is drawn to the surface of the film, if the film thickness is ~1L_0 thick, where L_0 is the period of the BCP in the bulk. After drying, the film is nanoporous, where the nanopores span the entire thickness of the film. If, however, the cylindrical microdomains are oriented parallel to the substrate, the film consists of a cylindrical microdomains embedded in a matrix of the major component. Here, with a preferential swelling, one of the following two things occurs. In one case, if the major component is below its glass transition temperature, the osmotic force to swell the minor component is sufficiently large to cause a deformation of the glassy matrix to increase the size of the minor component phase and, upon drying, a larger, less dense microdomain of the minor component is formed. That leads to a substantially enhanced etching rate of the P2VP domains. Alternatively, the osmotic

force to dissolve the minor component can be sufficiently large so that the minor component breaks through to the surface of the film and, upon drying, a trench is generated in the film. In either case, the highly selective dry etching process enables the transfer of the copolymer pattern to a silicon substrate to form high aspect ratio silicon trenches. Unlike lamellae forming PS-*b*-PMMA which is used to generate trenches in silicon, the method described here does not require a neutral brush layer to orient the BCP microdomains normal to the film surface. PS and P2VP, the constituent blocks of the BCP under study here, have a large (more non-favorable) Flory-Huggins interaction parameter (χ ~0.18) than PS-*b*-PMMA (χ ~0.06), so that theoretically smaller microdomains can be achieved more readily by self-assembly.[18]

3.2. Experimental

3.2.1. Materials

PS-*b*-P2VP (Mn= 40,000-*b*-18,000 kg/mol, Mn= 23,600-*b*-10,400 kg/mol) and PS-*b*-PEO (Mn= 32,000-*b*-11,000 kg/mol) were purchased from Polymer Source, Inc. and used without further purification. PS-*b*-P2VP was dissolved in toluene and tetrahydrofuran (THF) (volume fractions of 8:2) to form a solution with a concentration ranging between 0.7 ~ 1%. PS-*b*-PEO was dissolved in benzene to form a solution with a concentration of 0.6%. BCP thin films were prepared by spin coating where the film thickness was controlled by varying concentration of the solution and the spin coating speed.

3.2.2. Sample preparation

The PS-*b*-P2VP thin film was solvent-vapor annealed in 0.5 ml THF in a 250ml closed jar for different amounts of time. The PS-*b*-PEO thin film was preswelled in 0.2ml water for 1 h, then solvent annealed in 0.5ml THF in a 250 ml jar for 2 h, then open the top cap to remove the solvent instantaneously. For PS-*b*-P2VP 58k BCP, a maximal swell ratio of 2.2 was achieved during SVA. The annealed film was reconstructed by immersing the it in ethanol for 30 min.

The O_2 /Ar RIE was performed at 75 W for 5s to 30s in Oxford instrument Plasmalab 80 plus. Flow rate of O_2 and Ar were 20 sccm and 2 sccm respectively, the chamber pressure was 10 mTorr. The SF_6 and O_2 cryo-ICP etching was performed at 5 W for etching chamber and 1000 W for plasma generator chamber for 5s to 20s in Oxford instrument Plasmalab 150. Flow rate of SF_6 was 34 sccm and O_2 was 16 sccm, chamber pressure was 30 mTorr.

3.2.3. Characterization

A Veeco Digital Instruments nanoscope 3 was used to characterize the surface morphology by tapping-mode scanning force microscopy (SFM).

A Zeiss Ultra 60 SEM was used to image the surface of the BCP thin films. The acceleration voltage was 1 kV. All samples were imaged without any metal coating of the sample surface.

GISAXS measurements were performed at beamline 7.3.3, Advanced Light Source at the Lawrence Berkeley National Laboratory. The wavelength of X-rays was 1.24 Å.

3.2.4. Simulation of 2D scattering pattern Si trench pattern

On the DWBA, the Si pattern has an average thickness of 73nm and occupies an average volume of about 35% of that of the total patterned film volume. Since, the refractive index of Si at 10 keV is $n=1-4.88e^{-6}-i*7.37e^{-8}$, we have used the average refractive index of the patterned film $n_{_0} = 1-1.7e^{-6}-i*2.58e^{-8}$ as the reference index in the DWBA computation.

3.3. Results and discussion

3.3.1. Self-assembly of etch mask from BCP

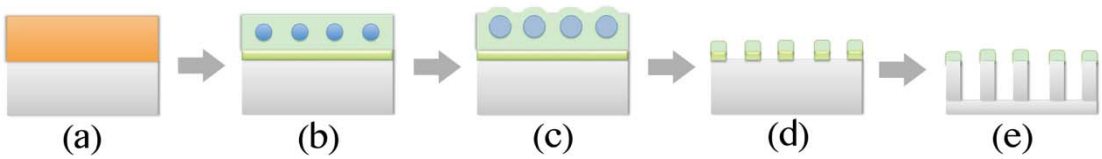

Schematic 3.1 Schematic diagram for self-assembled PS-*b*-P2VP thin film patterning of silicon nano-trenches (a) PS-*b*-P2VP spin coated on silicon wafer (b) microphase separated PS-*b*-P2VP film after solvent annealing (c) BCP film after reconstruction in ethanol to enhance the etching contrast between PS and P2VP domains (d) polymer pattern after etching the BCP film by means of RIE (e) silicon trenches after cryo-ICP etching using the polymer mask

Schematic 3.1 shows the scheme for the process to fabricate the high aspect ratio silicon trenches based on BCP self-assembly, reconstruction, and an RIE process. A PS-*b*-P2VP BCP thin film was spin coated onto a p-type silicon wafer (Schematic 3.1a). The BCP thin film was solvent annealed in THF vapor in a sealed jar for different times ranged from 20 minutes to 3 hours to form microphase separated P2VP cylindrical

microdomains, oriented parallel to the film surface, imbedded in a PS matrix (Schematic 3.1b). The solvent annealed BCP film without reconstruction showed little SEM or SFM contrast between the PS matrix and P2VP microdomains. When the BCP film was reconstructed[24] by immersion in ethanol, a good solvent for P2VP but a bad solvent for PS, ethanol swelled the P2VP microdomains. The resulting volume expansion of the P2VP domains caused the PS matrix above it to deform during the reconstruction process. Some of the PS film also was broken through showing perforation from above as observed by scanning force microscopy (SFM). Since the PS matrix was below its glass transition temperature, drying the thin film results in a reduced packing density of the P2VP domain or even holes in the PS matrix. The structure of the reconstructed film was preserved after drying, since PS was below its T_g (Schematic 3.1c). A mild O_2 /Ar RIE was applied to the reconstructed thin film. The loosely packed P2VP domains etch significantly more rapidly than the PS domains, leaving behind a polymeric line pattern consisting mainly of PS (Schematic 3.1d). A highly selective cryo-ICP SF_6/O_2 etching transferred the polymer mask pattern into the silicon substrate to form high aspect ratio silicon trenches (Schematic 3.1e).

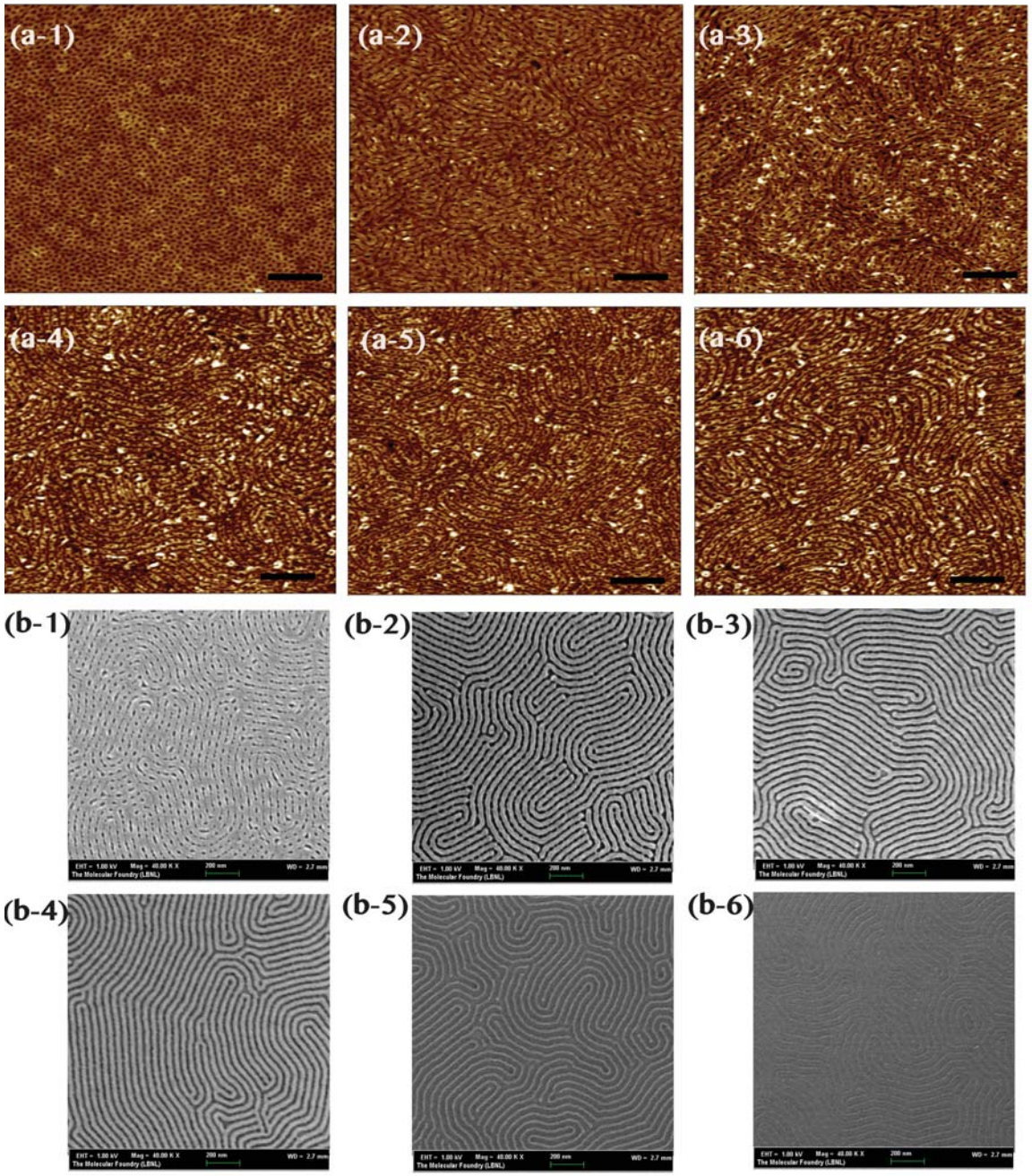
(a-1)
(a-2)
(a-3)
(a-4)
(a-5)
(a-6)
(b-1)
(b-2)
(b-3)
(b-4)
(b-5)
(b-6)

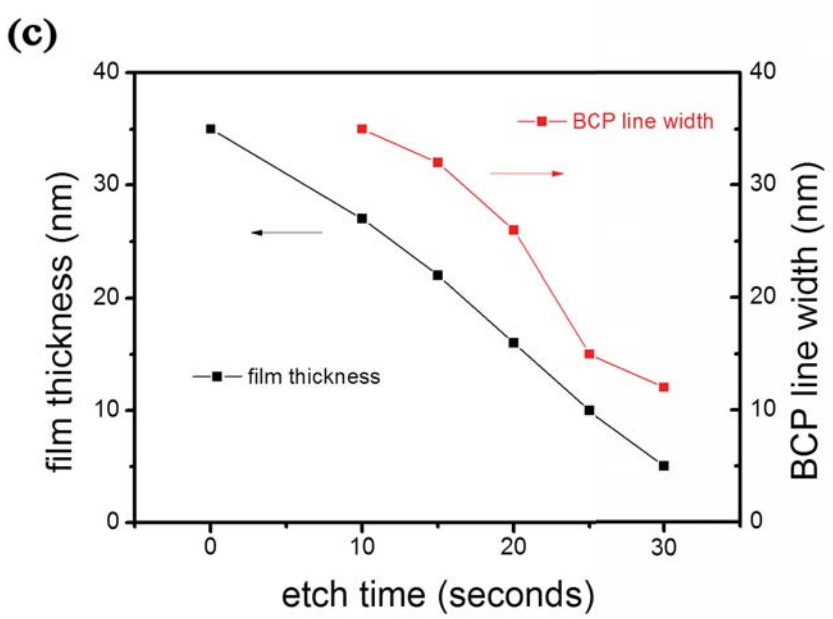

Figure 3.1Surface topography of PS-*b*-P2VP 58k during the different stage of solvent annealing and RIE. (a) SFM height images of the surface topography after different times of annealing in THF vapor, as spun (a-1), 20 min (a-2), 40 min (a-3), 60 min (a-4), 120 min (a-5), 180 min (a-6). All films were reconstructed in ethanol for 30 min before SFM imaging. Scale bars correspond to 250nm. (b) SEM images of the BCP film surface morphology after RIE at different etching times following solvent annealing and reconstruction: 0 sec (b-1), 10 sec (b-2), 15 sec (b-3), 20 sec (b-4), 25 sec (b-5), 30 sec (b-6) of etching in O_2 and Ar. Plot of the film thickness and the BCP line width, resp., versus the etching time (c).

In the as-spun (Figure 3.1 a-1) film, hexagonally packed cylindrical microdomains oriented normal to the film surface were observed. Figure 3.1a-1~6 shows SFM height images of the surface topography of PS-*b*-P2VP 58k films annealed in THF for different times and then, subsequently reconstructed in ethanol. The solubility parameter for tetrahydrofuran (THF) is 19.4 $(MPa)^{1/2}$, for PS it is 18.5 $(MPa)^{1/2}$ and for P2VP it is 20.4 $(MPa)^{1/2}$.[25] Consequently, THF is a neutral solvent for the PS block and P2VP block. In the THF-annealed films, the P2VP microdomains are oriented parallel to the surface and embedded in a PS matrix. There is only a ~2nm height difference that indicates the location of the P2VP microdomains. After reconstruction, the swelling of

the P2VP microdomains by ethanol amplifies this height difference to ~7nm. After the film was solvent annealed in THF for 20 minutes, P2VP micelles begin to merge, forming elliptical-shaped micelles (Figure 3.1a-2). After 40 minutes annealing, these elongated P2VP micelles merge with nearby micelles and form longer micelles (Figure 3.1a-3). After 1 hour annealing, cylindrical micelles are clearly observed after reconstruction of the film. Cylindrical micelles form parallel to the silicon substrate after 1 hour annealing in THF vapor (Figure 3.1a-4,5,6). By contrast, ethanol has a solubility parameter of 26.0 $(MPa)^{1/2}$. Consequently, the preferential solvation of P2VP by ethanol is so strong that P2VP is drawn to the surface, forming holes (Figure 3.1a-4,5,6) above the cylindrical P2VP domains in the reconstructed films.

To pattern the substrate, finely tuned RIE processes were developed. Figure 3.1b-1~6 shows SEM images of the solvent annealed and reconstructed surface of PS-*b*-P2VP BCP thin films as a function of etching time, using an O_2 and Ar gas mixture (flow rate ratio 10:1). After 10 sec of etching a continuous trench pattern was observed (Figure 3.1b-2). Further etching reduced both width and thickness of the cylindrical polymeric structure in this non-selective, nearly isotropic etching process. The etching rate in this case was ~0.9 nm/sec. Hence, the ability to create a well-defined pattern arises strictly from the BCP reconstruction in ethanol. This is confirmed with an reactive ion etched, THF-solvent-annealed PS-*b*-P2VP film that was not reconstructed, which showed almost no selectivity between the PS and P2VP domains. In this case there is only a 2 nm trench after etching, in comparison to the 14 nm trench, if the BCP film was reconstructed before etching. The reconstruction decreases the density of the P2VP microdomains, while the PS matrix is insoluble in the solvent and the density remains fixed. The center-

to-center distance of the resulting etched line patterns were measured from the SEM micrographs (Figure 3.1b-1~6) and are plotted versus the etching time in Figure 3.1c. The center-to-center distance, as it would be expected, remained unchanged at a value of ~42 nm during etching. After 25 seconds of oxygen plasma treatment, 15 nm wide and 10 nm thick PS walls are seen with a ~42 nm center-to-center distance over a 10 cm silicon wafer.

3.3.2. Pattern transfer from BCP mask to silicon- trench pattern

Pattern transfer of the thin, high-resolution polymer mask to create a high aspect ratio silicon structure is a challenge. Here, cryo-ICP etching with SF_6/O_2 at a temperature of -120 Celsius was used for high fidelity nanoscale pattern transfer without an undercut. This process was tuned for an extremely high polymer to silicon etch selectivity to enable a one-step, high fidelity pattern transfer using very thin polymer masks.[26] The low temperature enhances the sticking coefficients to form a thin SiO_xF_y layer to passivate the sidewalls with only small additions of oxygen to the etching gas. The anisotropic ion distribution in ICP etching preferentially bombards and removes the passivant formed at the bottom of the silicon trench, to break through the passivant, etch the silicon, and produce high aspect ratio features with vertical sidewalls. A combination of low temperature, low oxygen, and low RF power decreases the etch rate of the polymer mask and significantly enhances the overall selectivity to allow high aspect ratio nanoscopic features with a thin polymer mask. Figure 3.2 shows the structures before (Figure 3.2a,c) and after cryo-ICP etching (Figure 3.2b,d). After 15 sec of cryo-ICP etching, sub-15nm high aspect ratio silicon walls with near vertical sidewalls were produced. The top-down

SEM views, before and after etching, (Figure 3.2a,b) show a dramatic change in contrast after the silicon trenches were created but no change in feature size. The 60° tilted cross-section views show the thin mask (Figure 3.2c), the silicon nano-walls (Figure 3.2d) and the smooth, vertical silicon sidewalls. The width and height information of the silicon walls were obtained from the SEM image at 5 different spots. The silicon walls have a width of 14±1 nm and center-to-center distance of 42±2 nm (same as the initial mask) indicating the cryo-ICP delivers pattern transfer with high fidelity. The sample lost etching mask if it was etched for 20sec in ICP. Thus, we estimated the residual layer of the polymer mask was ~2 nm. Thus the cryo-ICP etching selectivity between the polymer mask and silicon is ~ 10:1. This methodology is capable to scale down to pattern smaller features by reducing the molecular weight of the BCP. A lower PS-*b*-P2VP molecular weight (Mw 23.6-*b*-10.4 kg/mol) was also used to increase the area density of the silicon nano-wall patterns. Figure 3.3 shows a 27 nm pitch silicon trench with a width of 12±1nm and a depth of 50 nm.

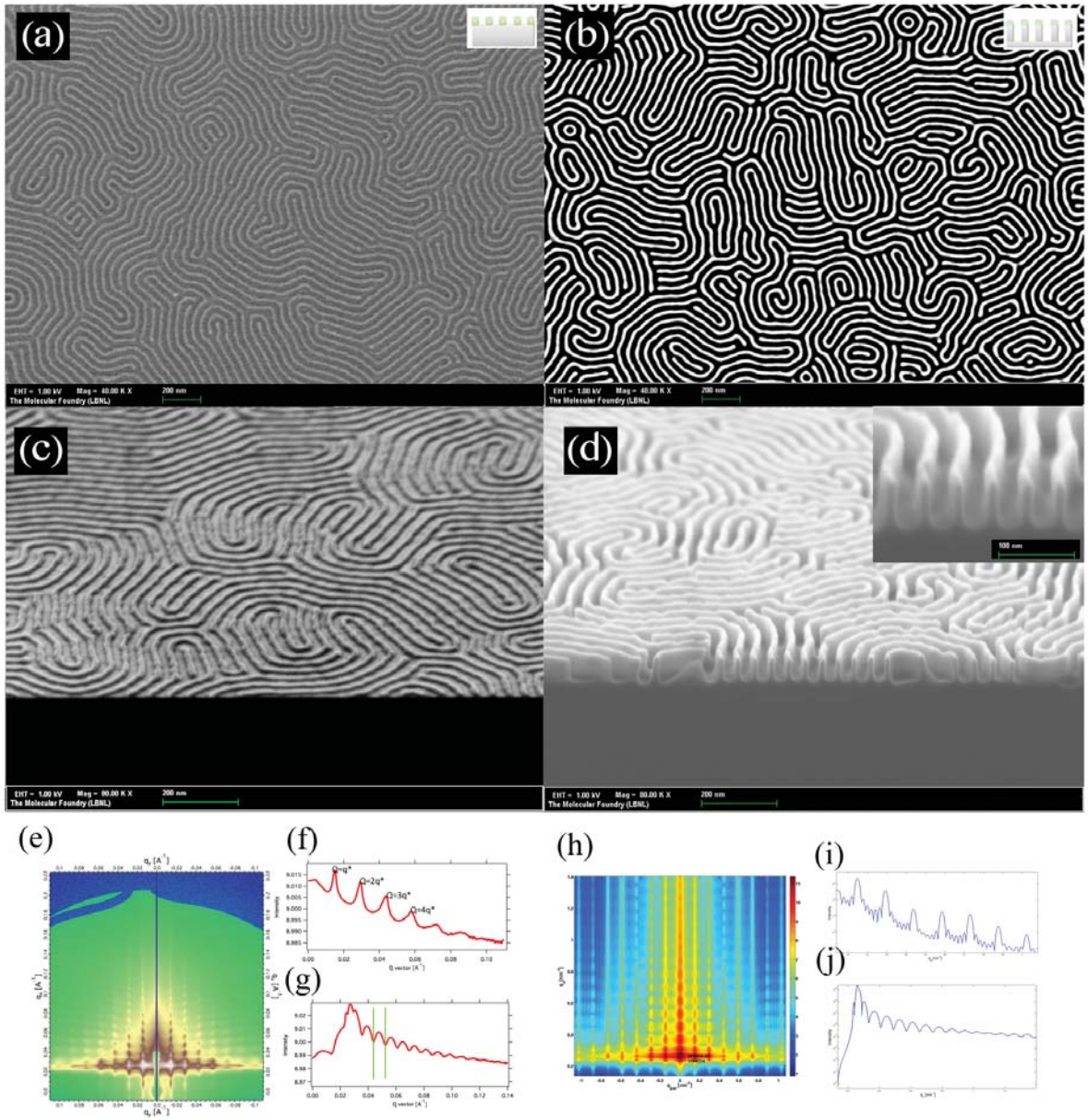

Figure 3.2 SEM images of thin film surface before, (a) plane-view (c) 60 degree tilt view, and after 15 sec of cryo ICP etching (b) plane-view (d) 60 degree tilt view. *Inset* image in (d) is a zoomed in image. (e, h) are 2D GISAXS patterns of silicon nanotrenches. Experimental data are shown in (e,f,g) and simulated data in (h,i,j). (f,i) are intensity plot with repect to peak position in-plane. (g,j) are intensity plot with repect to peak position out-of-plane

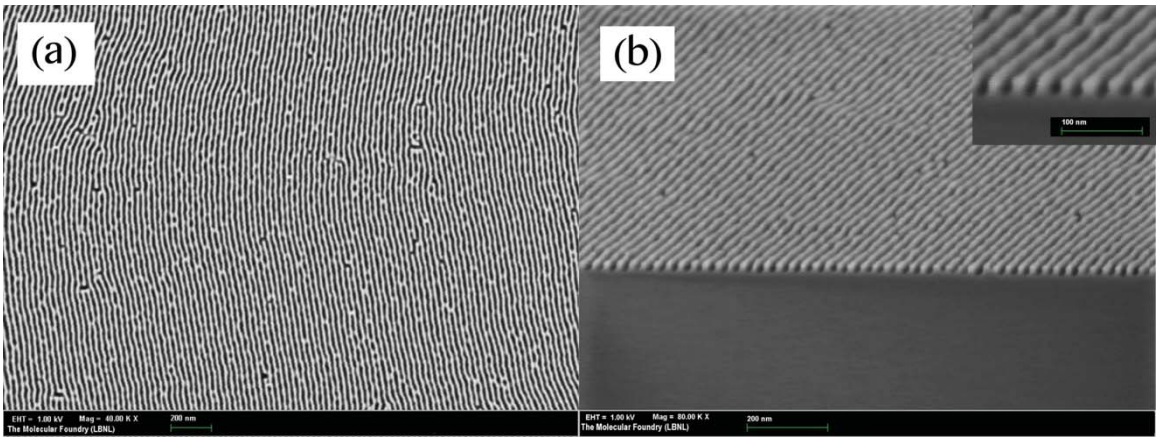

Figure 3.3 SEM images of silicon nano-trenches with a pitch of 27nm patterned from PS-*b*-P2VP (Mn= 23,600-*b*-10,400 kg/mol). (a) plane-view (b) 60 degree tilted cross-sectional view. *Inset* image in (d) is a zoomed in image.

GISAXS was used to characterize the silicon nanotrench. Figure 3.2e~j shows the GISAXS pattern of the silicon nanotrench and a simulated GISAXS pattern, calculated using the Distorted Wave Born Approximation (DWBA). Both the height information and center-to-center distance of silicon walls can be obtained from Figure 3.2e and the data agrees well with SEM cross-section image (Figure 3.2d). A line cut profile of the scattering pattern in the q_y direction shows higher order scattering peaks, indicating a highly ordered, periodic structure in the plane of the substrate. From the value of the first order Bragg peak, q_y*, the average center-to-center distance of the silicon trenches was determined to be ~ 42 nm, which coincides with the corresponding value of polymer resist pattern before ICP etching. The modulation of the intensity in the q_z direction arises from the incident beam being reflected by the top and bottom surface of the silicon trenches. The separation in q between consecutive minima of these Kiessig fringes, Δq, is 8.5×10^{-3} A^{-1}, yielding an average depth of the trench of 73 nm, which is in good agreement with SEM cross-section of the silicon trenches (Figure 3.2d). A simulated 2D GISAXS pattern of the silicon nanotrenches is shown in Figure 3.2h and was created as

follows. The silicon nanotrench was modeled as an array of trenches having a length of 200 nm, a width of 15±2 nm and a height of 73±3 nm with 42nm spacing. The cross section profile is radially averaged in all the in-plane orientations, to simulate the fingerprint pattern (no ordering in plane view) (Figure 3.2d). An isosceles trapezoidal cross section of the lines has a base angle $88^{o}\pm2^{o}$ (near vertical). The introduction of 2 degree tilted sidewalls produced a curvature in the array of peaks away from q_y and resulted in relative peak intensities in closer agreement with the experiment (Figure 3.2e, h). Line cuts in q_z and q_y in the simulated data agree well with experiment data in terms of the peak decay (Figure 3.2f~j).

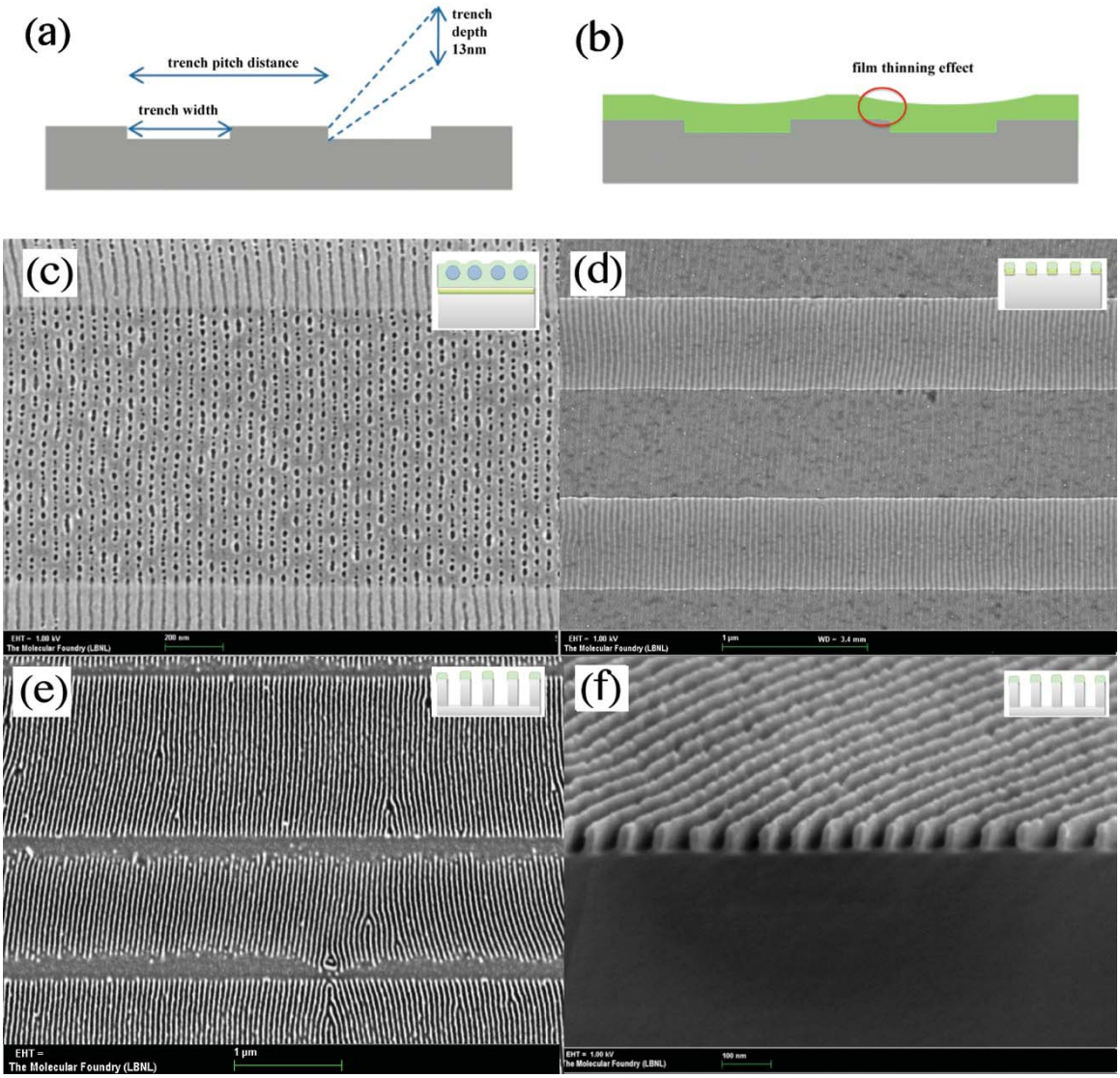

Figure 3.4 SEM images of a PS-*b*-P2VP (40,000-*b*-18,000 kg/mol) pattern DSA by the trench pattern, and its pattern transfer into silicon. (a) illustration of the trench pattern. (b) illustration of the film thinning effect close to the edge of mesa. (c) PS-*b*-P2VP on a patterned substrate after solvent annealing and subsequent reconstruction, (d) PS-*b*-P2VP on a patterned substrate after solvent annealing, reconstruction and etching. (e), (f) silicon nano-trenches after the pattern transfer.

Graphoepitaxy was used to guide the PS-*b*-P2VP BCP to self-assemble into a long range ordered array of cylindrical microdomains oriented parallel to the film surface. A trench pattern with a depth of 13 nm, widths of 600 and 1200 nm, and pitches of 1300 nm and 2600 nm, (Figure 3.4a) respectively, were fabricated in a silicon wafer

using photolithography and CF_4 RIE. A film thinning effect at the edges of the trenches caused a gradient in the remaining cylindrical microdomains (Figure 3.4b). Cylindrical domains oriented normal to the trench sidewalls were observed when PS-*b*-P2VP (Mn= 40,000-*b*-18,000 kg/mol) was solvent annealed in THF vapor (Figure 3.4c). The same phenomenon was observed by H.C. Kim *et al.* for PS-*b*-PMMA block copolymers.[27] The authors argued that surface corrugation results in a polymer chain distortion, forcing the copolymer to follow the contour of the surface corrugation. After the film is etched in O_2/Ar RIE for 25 sec, a highly ordered polymeric mask was formed on the topographic features (Figure 3.4d). After 15 seconds of cryo-ICP etching, BCP cylindrical microdomains were transferred into the underlying silicon (Figure 3.4e). Defects on the raised portion of the silicon were due to the mask gradient near the edge. Cross-sectional images (Figure 3.4f) show that unidirectional silicon trenches were achieved. The depth of silicon nano-trenches is about 70 nm.

3.3.3. Pattern transfer from BCP mask to silicon- hole pattern

We demonstrate the generality of this reconstruction and etching methodology, using a polystyrene-*block*-poly(ethylene oxide) (PS-*b*-PEO) BCP to form silicon nanoholes. By using water and THF, the PS-*b*-PEO was solvent annealed to form cylindrical microdomains oriented normal to the surface of the film. After the film was reconstructed in ethanol, porous films were formed on the silicon (Figure 3.5a). Most of the PEO was displaced to the surface, while a small fraction, due to the bonding to the PS block, remained in the nanohole. After 10 sec of etching in oxygen plasma, the residual PEO in the nanohole was removed leaving a patterned polymer mesh mask on the wafer

(Figure 3.5b). The high-selectivity cryo-ICP SF_6/O_2 was again used to etch the silicon. Figure 3.5c shows PS-*b*-PEO masked silicon after 10 sec ICP etching. During the sample cleaving, part of the polymer mask peeled away to reveal the etched silicon structure. And after 20 sec ICP etching, 60 nm deep, 25±2 nm diameter nanopores were created in silicon with an average pitch of 40nm.

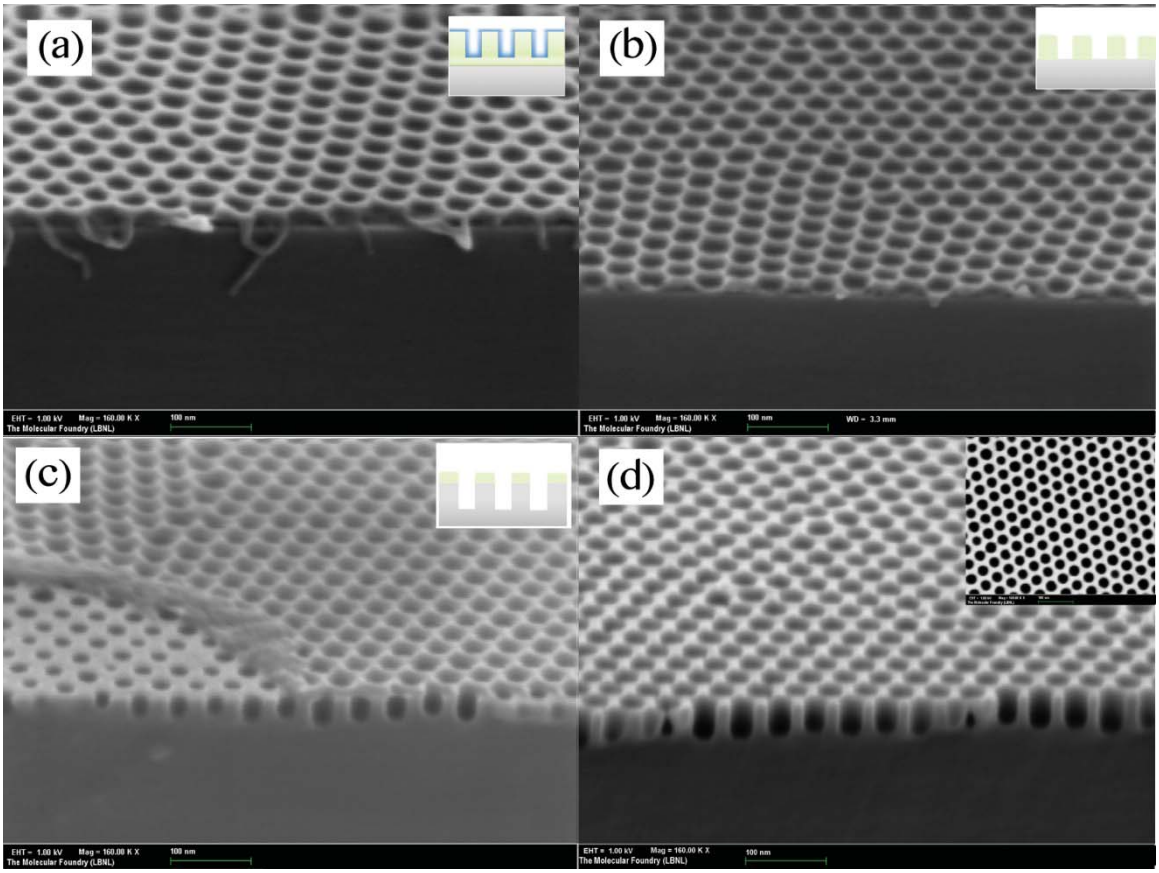

Figure 3.5 SEM images of a PS-*b*-PEO forming cylindrical domains oriented normal to the substrate. SEM was taken at a 60 degree tilt angle (a) block copolymer pattern after solvent annealing and subsequent reconstruction in ethanol, (b) the film after an additional etching of 10 s in RIE (c) transferred pattern in silicon after 10 s of cryo-ICP etching using the BCP mask (d) silicon pattern after 20 s of cryo-ICP etching. *Inset* image in (d) is the plane view of the silicon nano-hole pattern.

3.3.4. Nano-imprint using silicon mold

These samples with silicon nano-trenches (and, also nanopores) were used as a master template for nano-imprint lithography (NIL). The silicon mold was treated with a mold release agent 1H,1H,2H,2H-perfluorooctyltrichlorosilane and then imprinted on a PS resist, assisted by heating the PS to 130 degree Celcius (which is above the glass transition temperature of PS) for 20 min. The PS resist pattern shows a width of 25 nm and pitch of 42nm (Figure 3.6), reflecting a pattern transfer with high fidelity. This mold could also be used to pattern other functional materials, like P3HT as shown in Figure 3.7, and other conducting polymers. Such sub-20 nm patterned P3HT is very interesting for photovoltaic applications, since the diffusion length of excitons is about 10 nm. Such silicon trenches or holes are also very interesting for biosensor[28] and gas sensor applications[29].

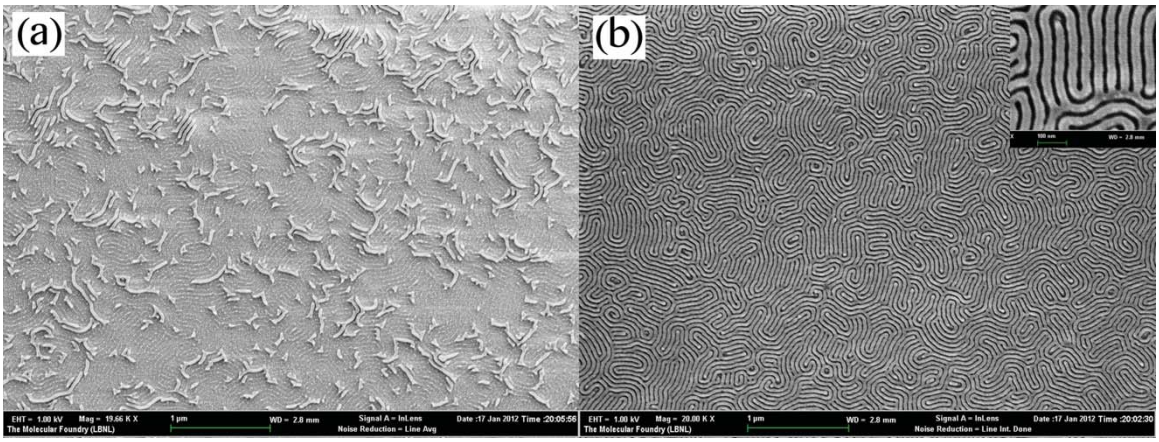

Figure 3.6 SEM images of a PS resist after thermal imprinting using silicon fin as mold. (a) mold without treated with anti-sticking layer, (b) after the mold treated with FAS anti-sticking layer.

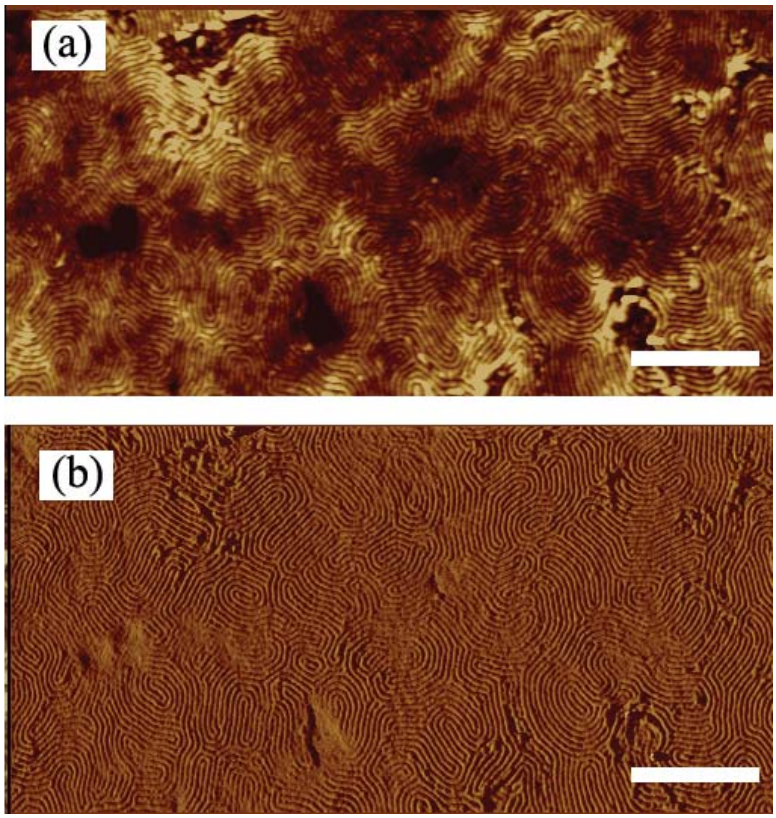

Figure 3.7 SFM images of P3HT after thermal imprinting using silicon fin as a mold. (a) height image, (b) phase image. Scale bar 1um.

3.4. Conclusions

In conclusion, we have shown that a simple reconstruction of BCPs can provide etching contrast and allows the patterning of BCP masks for subsequent pattern transfer into the underlying substrate. A highly selective cyro-ICP etching recipe was used to etch the silicon with a polymer:silicon selectivity of up to 1:10. Densely packed, sub-15 nm, 5:1 Si nano-trenches were fabricated. These nano-trench patterns were used as a nano-imprint master to pattern polymeric materials. Oriented silicon nano-trenches were created using graphoepitaxy directed self-assembly. The methodology was shown to be general and was used to pattern silicon holes from a patterned surface-perpendicular cylinder forming PS-*b*-PEO block copolymer.

3.5. References

(1) Bang, J.; Jeong, U.; Ryu, D. Y.; Russell, T. P.; Hawker, C. J. *Adv Mater* **2009**, *21*, 4769–4792.

(2) Bates, F. S.; Fredrickson, G. H. *Physics Today* **1999**, *52*, 32–38.

(3) Park, S.; Lee, D. H.; Xu, J.; Kim, B.; Hong, S. W.; Jeong, U.; Xu, T.; Russell, T. P. *Science* **2009**, *323*, 1030–1033.

(4) Liu, C.-C.; Nealey, P. F.; Ting, Y.-H.; Wendt, A. E. *J. Vac. Sci. Technol. B* **2007**, *25*, 1963–1968.

(5) Tanaka, T.; Morigami, M.; Atoda, N. *Japanese Journal of Applied Physics* **1993**, *32*, 6059–6064.

(6) Mansky, P.; Chaikin, P.; Thomas, E. L. *Journal of Materials Science* **1995**, *30*, 1987–1992.

(7) Park, M.; Harrison, C.; Chaikin, P. M.; Register, R. A.; Adamson, D. H. *Science* **1997**, *276*, 1401–1404.

(8) Chai, J.; Buriak, J. M. *ACS nano* **2008**, *2*, 489–501.

(9) Chai, J.; Wang, D.; Fan, X. N.; Buriak, J. M. *Nat. Nanotechnol.* **2007**, *2*, 500–506.

(10) Peng, Q.; Tseng, Y.-C.; Darling, S. B.; Elam, J. W. *ACS nano* **2011**, *5*, 4600–4606.

(11) Peng, Q.; Tseng, Y.-C.; Darling, S. B.; Elam, J. W. *Adv Mater* **2010**, *22*, 5129–5133.

(12) Tseng, Y.-C.; Peng, Q.; Ocola, L. E.; Elam, J. W.; Darling, S. B. *J. Phys. Chem. C* **2011**, *115*, 17725–17729.

(13) Park, S.; Kim, B.; Wang, J. Y.; Russell, T. P. *Adv Mater* **2008**, *20*, 681–685.

(14) Xu, J.; Hong, S. W.; Gu, W.; Lee, K. Y.; Kuo, D. S.; Xiao, S.; Russell, T. P. *Adv Mater* **2011**, *23*, 5755–5761.

(15) Lammertink, R. G. H.; Hempenius, M. A.; Van den Enk, J. E.; Chan, V. Z. H.; Thomas, E. L.; Vancso, G. J. *Adv Mater* **1999**, *12*, 98–103.

(16) Cheng, J.; Ross, C.; Chan, V.; Thomas, E.; Lammertink, R.; Vancso, G. *Adv Mater* **2001**, *13*, 1174–1178.

(17) Cheng, J. Y.; Ross, C. A.; Thomas, E. L.; Smith, H. I.; Vancso, G. J. *Appl. Phys.*

Lett. **2002**, *81*, 3657–3659.

(18) Jung, Y. S.; Ross, C. A. *Nano Lett.* **2007**, *7*, 2046–2050.

(19) Jung, Y. S.; Ross, C. A. *Small* **2009**, *5*, 1654–1659.

(20) Jung, Y. S.; Jung, W.; Ross, C. A. *Nano Lett.* **2008**, *8*, 2975–2981.

(21) Jung, Y. S.; Chang, J. B.; Verploegen, E.; Berggren, K. K.; Ross, C. A. *Nano Lett.* **2010**, *10*, 1000–1005.

(22) Farrell, R. A.; Petkov, N.; Shaw, M. T.; Djara, V.; Holmes, J. D.; Morris, M. A. *Macromolecules* **2010**, *43*, 8651–8655.

(23) Borah, D.; Shaw, M. T.; Rasappa, S.; Farrell, R. A.; O'Mahony, C.; Faulkner, C. M.; Bosea, M.; Gleeson, P.; Holmes, J. D.; Morris, M. A. *J Phys D Appl Phys* **2011**, *44*, 4012.

(24) Xu, T.; Stevens, J.; Villa, J. A.; Goldbach, J. T.; Guarini, K. W.; Black, C. T.; Hawker, C. J.; Russell, T. P. *Advanced Functional Materials* **2003**, *13*, 698–702.

(25) Brandrup, J. I.; Immergut, E. H.; Grulke, E. A.; Grulke, A. *Polymer Handbook*; 4 ed.; Wiely: New York, 1999.

(26) Liu, Z.; Wu, Y.; Harteneck, B.; Olynick, D. *Nanotechnology* **2012**, *24*, 015305.

(27) Park, S.-M.; Berry, B. C.; Dobisz, E.; Kim, H.-C. *Soft Matter* **2009**, *5*, 957–961.

(28) Jane, A.; Dronov, R.; Hodges, A.; Voelcker, N. H. *Trends Biotechnol* **2009**, *27*, 230–239.

(29) Stewart, M.; Buriak, J. *Adv Mater* **2000**, *12*, 859–869.

CHAPTER 4

SELF-ASSEMBLED BCP MICRODOMAINS FOR BIT PATTERNED MEDIA APPLICATIONS

4.1. Introduction

According to Moore's law, the transistor density on an integrated circuit doubles every 18 months, and thus there is a continuing need for higher resolution lithography[1]. Traditional optical lithography will soon hit its resolution limits due to diffraction problems. Several lithographic techniques, like e-beam lithography[2], nanoimprint lithography[3,4] and block copolymer (BCP) lithography[5-15], have risen as promising candidates for the fabricate on of the next-generation devices. E-beam lithography can provide sub-30 nm patterns, but is limited by low through-put and high fabrication costs. Nano-imprint lithography is viable for mass production of devices, but requires the fabrication of a costly master template[3,4]. BCP lithography, however, provides a fast, size-tunable, and cost-effective way to fabricate arrays of nanoscopic elements that is non-disruptive and easily integrated into current fabrication processes.

During the past decades, the directed self-assembly (DSA) of BCPs has been extensively investigated. BCPs consist of two different polymer chains covalently bonded together at one end can self-assemble to highly ordered arrays of nanoscopic spherical, cylindrical, and lamellar domains, depending on the volume fraction of the components, f, and the segmental interaction parameter, χ, between the components. More recently,

near-perfect arrays of cylindrical microdomains, only 3 nm in diameter, over macroscopic areas have been achieved using the DSA of BCPs on faceted substrate[5]. Single grains of ordered patterns can be extended over large areas by introducing chemical or topological modifications to the surface of the substrate to affect the DSA of BCPs[7,16].

One of the key steps to incorporate BCP patterns into nano-fabrication processes is by pattern transfer[17]. Organic block copolymers, consisting mainly of carbon and hydrogen, are susceptible to degradation during reactive ion etching (RIE), limiting their use as etching masks. Silicon oxide, which consists of heavier elements, is more resistant to reactive ion etching, thus making it an ideal etch mask candidate. Other groups have reported using self-assembled silicon-containing BCP film to create silicon oxide dot or lines. Jung *et al.* [18-21] have demonstrated the fabrication of silicon oxide pillars from hexagonally packed spherical polydimethylsiloxane (PDMS) domains in a polystyrene (PS) matrix using a PS- b-PDMS BCP. Upon exposure to oxygen plasma, the PDMS microdomains are oxidized to silicon oxides. Xiao *et al.*[22] have reported highly ordered silicon oxide dots by the DSA of PS-*b*-PDMS using chemically patterned substrates. Hirai *et al.* [23,24] have reported the DSA of polyhedral oligomeric silsesquioxanes (POSS) containing BCPs to generate a silicon oxide nano-mesh. Russell and coworkers have reported the backfilling of PDMS into reconstructed polystyrene-*block*-poly(4-vinylpyridine) (PS-*b*-P4VP) BCP templates to make silicon oxide dots.[13]

The aforementioned work shows that silicon oxide pillars can be created from self-assembled BCP templates, but control over the size of the pillars without altering the domain spacing has not been reported. In order to increase the domain size without

altering the morphology, the chain lengths of both blocks have to be increased while maintaining the same ratio. Increasing the total molecular weight of the BCP not only results in an increase of the domain size, but also an increase in the pitch. In strongly segregated melts, the characteristic microdomain spacing $L_0 \sim N^{2/3}$, where N is the total number of segments in the BCP[25]. These competing effects present a problem for mask etch applications where a large feature size and a small pitch is desired. For example, the data storage industry is constantly striving to increase the size of magnetic domains in their hard drives while minimizing the pitch distance, as this would enhance signal-to-noise ratio and, possibly, storage capacity. Here, we present a new method to obtain silicon oxide pillars with tunable sizes to achieve high density and large area coverage of silicon oxide pillars with tunable domain size with a fixed pitch.

4.2. Experimental

4.2.1. Materials and sample preparation

Diblock copolymer of PS-*b*-P2VP and PS-*b*-P4VP with overall molecular weight 15.2 kg/mol, 19.5 kg/mol, 24.2 kg/mol, 77 kg/mol were purchased from polymer source, Inc. and used without further purification. The volume fractions of PVP block are 21.1%, 17.9%, 21.5% and 27.3% respectively. To obtain uniform thin films with thickness of 30nm, the BCPs were dissolved in THF and toluene (volume fraction 7/3) to form 0.6% wt solution. Then BCP solutions were spin coated onto the DLC substrate provided by Western Digital Inc.

4.2.2. Etching mask preparation

The BCP thin films were treated in THF vapor by SVA process inside a close jar with volume of ~ 250ml. The SVA processes take 30 minutes to 2 hours depend on different molecular weight. The BCP thin films were then immersed in ethanol to reconstruct the film to form porous template. A brief 10 sec, 75 watts oxygen/argon (130 mtorr, 9/1 ratio) RIE etching was used to enlarge the pore size. Then 0.1% PDMS in heptane, a cross solvent for PDMS and PS, was spin coated on the porous template. After that, the BCP template with coated PDMS was annealed at 60 degree for 30 minutes in a thermal oven in air. The film is then etched RIE etcher in CF_4 for 5 sec at 50 watts, followed by 30 sec oxygen/argon (130 mtorr, 9/1 ratio) plasma. For the pattern transfer process, 75 watts oxygen/argon (130 mtorr, 9/1 ratio) plasma with different etching time is used to demonstrate the pattern transfer process.

4.2.3. Characterization

The nanoscale morphology of BCP thin films and silicon pillar masks were imaged using a Hitachi S-4800 SEM with a field emission source at 20 kV and current of 10u A and Nanoscope 3 SFM using soft tapping mode.

The area coverage information of silicon oxide pillar was characterized using Image-Pro Plus software. The size was counted using the “measure” function in the software.

The nanoscale morphology of the BCP thin films and silicon pillar masks were imaged using a Hitachi S-4800 SEM with a field emission source at 20 kV and current of

10 μA and Nanoscope 3 SFM using soft tapping mode. The film thickness was measured by ellipsometry using a J. A. Wollam Co. ellipsometer.

The area coverage information of silicon oxide pillar was characterized using Image-Pro Plus software. The size was counted using the "measure" function in the software.

4.3. Results and discussion

4.3.1. Porous BCP template fabrication

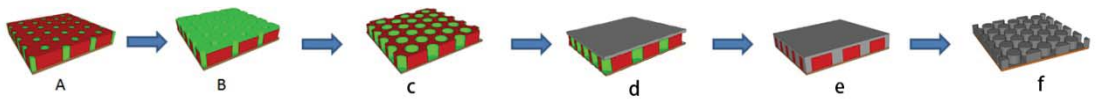

Schematic 4.1 Schematic procedure to make size tunable silicon oxide pillar by using block copolymer template

Schematic 4.1 shows the schematic process of fabricating silicon oxide pillar patterns with tunable domain sizes. A PS-*b*-P4VP 24k (Polymer Source) was spin-coated onto a silicon wafer and solvent annealed in tetrahydrofuran (THF), to self-assemble the BCP into hexagonally packed PVP cylindrical domains normal to substrate surrounded by a PS matrix (Schematic 4.1a). The film is treated with ethanol, which selectively dissolved the PVP domains to reconstruct the film. As the solvent dries, the PVP domains collapse on to the sidewalls and top surface of the PS matrix, creating pores in the film (Schematic 4.1b)[26]. To increase the domain size of the silicon oxide pillars without affecting the pitch, an oxygen/argon RIE was used to enlarge diameter of the pores in the BCP template (Schematic 4.1c). We take advantage of the isotropic property of RIE to

enlarge the average pore diameter in the BCP thin film. Linear PDMS (10,000 cSt kinematic viscosity, Gelest) solution in heptane is spin-coated onto the porous films surface (Schematic 4.1d) and baked at 60 °C for 10 min to promote capillary force driven diffusion of PDMS into the pores (Schematic 4.1e). The film is briefly exposed to tetrafluoromethane (CF_4) plasma etching to remove the excess of PDMS on the surface of the film. Then oxygen/ argon RIE is used to remove the PS matrix and oxidize PDMS into silicon oxide (Schematic 4.1f).

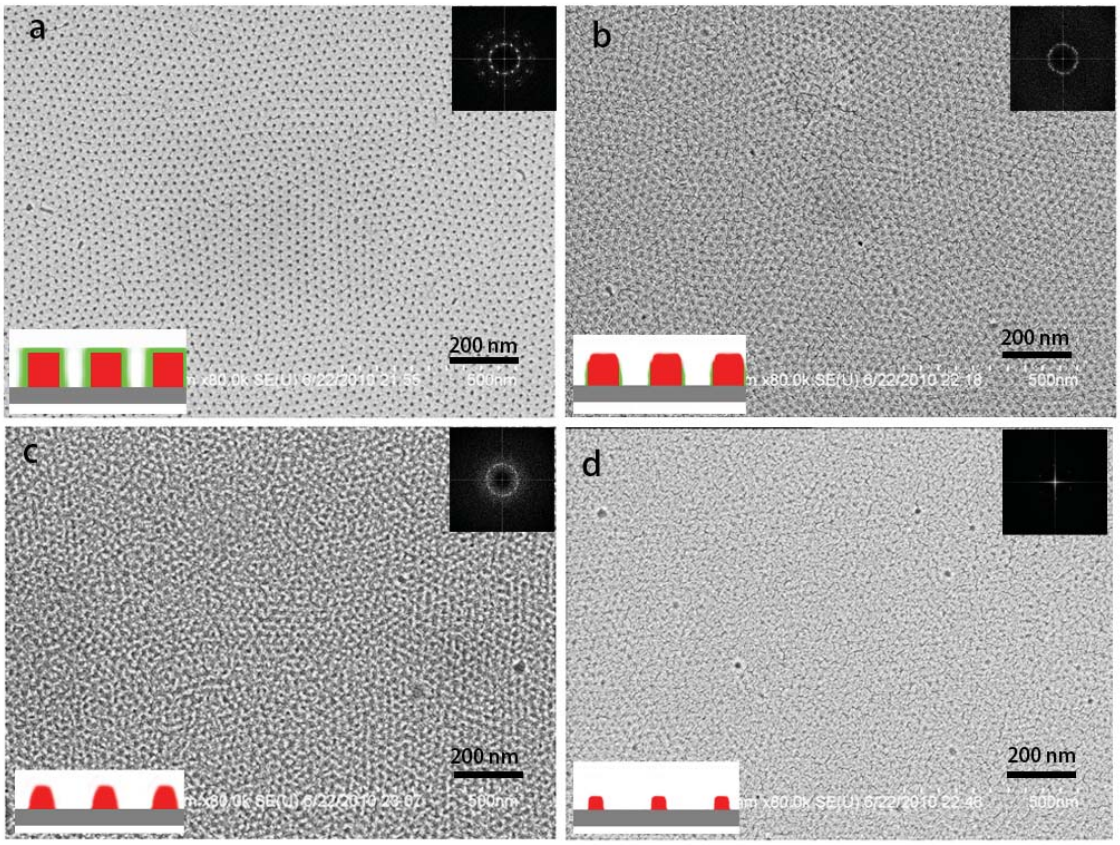

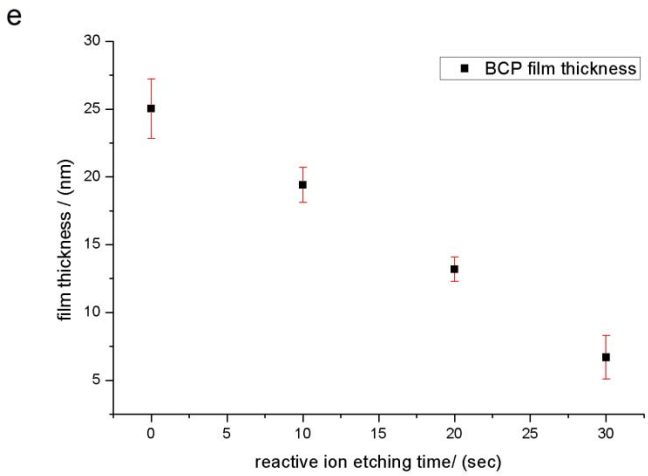

Figure 4.1 SEM image of PS-*b*-P4VP 24k polymer template with different amount of oxygen/argon plasma etching, all of these etching are at 75W. a) 0 seconds etching, b) 10 seconds etching, c) 20 seconds etching, d) 30 seconds etching. Inserted cartoon is cross section view of the pore pattern, e) plot of film thickness with reactive ion etching time.

To understand how the pore size is affected by the etching time, BCP porous templates were treated with oxygen/argon RIE under different exposure times and were examined by scanning electron microscopy (SEM). Figure 4.1 shows PS-*b*-P4VP (Mn = 24 000) porous templates after different etching exposure times. Before the oxygen/argon etching, the BCP film shows a porous structure with an average pore cross-sectional area of 38.5 ± 8.9 nm^2 or an average pillar diameter of 7.0 ± 1.0 nm. After 10 s of oxygen/argon RIE, the pores have average pore cross-sectional area of 153.9 ± 28.9 nm^2, or an average pillar diameter of 14.0 ± 1.1 nm. (Figure 4.1b), which is double the pore size of the unetched film. The isotropic nature of RIE etches away part of PVP in the pore sidewalls, increasing the average pore size in the film. After 20 s of oxygen/argon RIE, the pore size appears to be larger, but an average pore size cannot be determined as the pore structure is not clear on the SEM image (Figure 4.1c). After 30 s of oxygen/argon RIE, no pore pattern is observed in the SEM image (Figure 4.1d). The disappearance of

the porous structure in the film is related to a decrease in the film thickness. Increasing the RIE exposure time increases the pore size but decreases the film thickness. Ellipsometry was used to measure the BCP film thickness. The plot presented in (Figure 4.1e) shows a linear decrease in film thickness with increasing RIE exposure time. The etching rate estimated from this plot for a porous PS-*b*-P4VP film is 6.2 ± 0.6 Å/s under 75 W oxygen/argon (130 mTorr, 9/1 flow ratio). After 30 s of RIE exposure time, 74% of the film is etched away, which is why no pore pattern is observed in the SEM image. The pitch in the porous structure of the BCP templates was found to be independent of the RIE exposure time. The average pitch calculated from the Fourier transform of the SEM images, inset Figure 4.1a–c, was approximately 24.3 ± 2.2 nm for all the images. These results show that the pore diameter in a BCP template can be increased by RIE without affecting the pitch distance.

4.3.2. Silicon oxides pillar etch mask fabrication

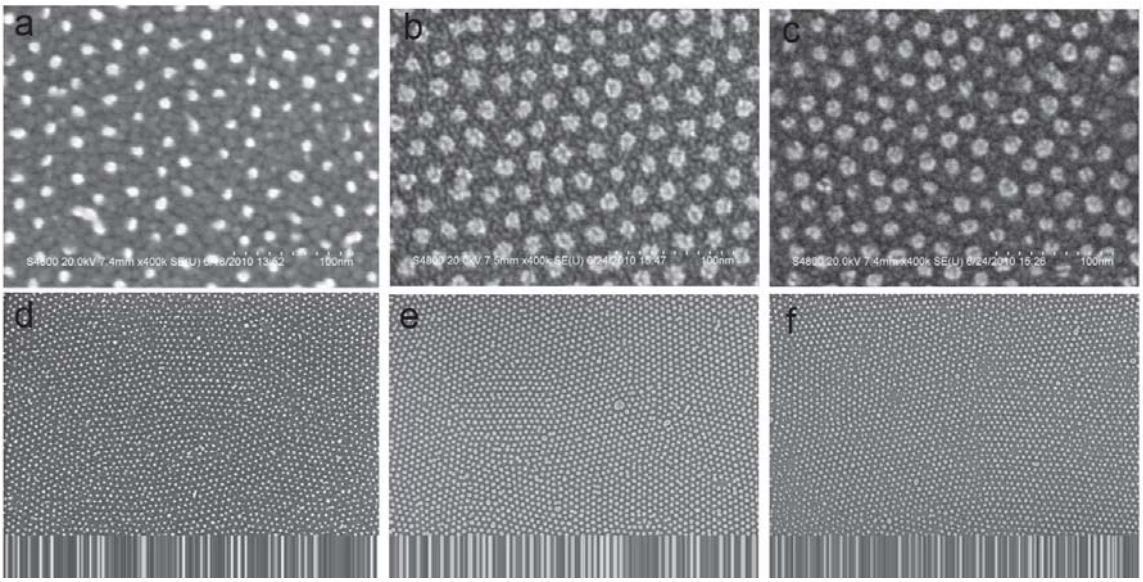

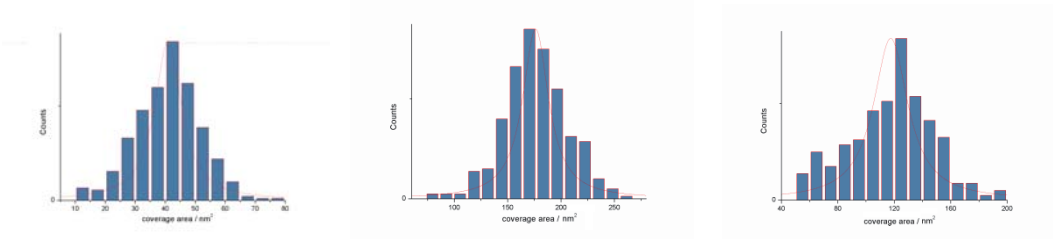

Figure 4.2 SEM image silicon pillar from PS-*b*-P4VP 24k with different amount of Ar/O_2 plasma etching time. a) and e) 0 seconds etching. b) and e) 10 seconds etching. c) and f)20 seconds etching. The first row is high magnification. The lower row is low magnification.

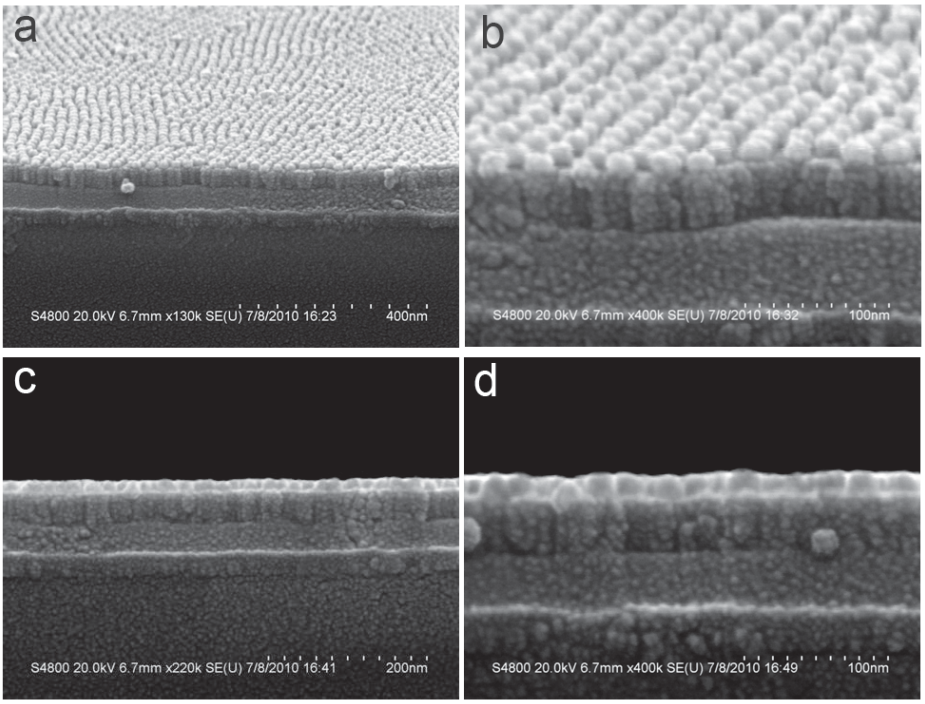

Figure 4.3 Cross section SEM image of silicon pillar from PS-*b*-P4VP 24k. a) low magnification of 75 degree tilted view. b) high magnification of 75 degree tilted view. c) low magnification of 90 degree tilted view. d) high magnification of 90 degree tilted view

The silicon oxide pillar pattern is the reversed pattern of the porous BCP template. Figure 4.2 shows the SEM images of the silicon oxide pillars made from the BCP templates. Silicon oxide pillars were not observed from the 30 s etched BCP template; therefore, the SEM image for this sample was not included in Figure 4.2. The silicon

oxide pillar patterns are exactly reversed from the pore patterns observed on the BCP templates. The silicon oxide pillar pattern made from the unetched BCP template shows an average pillar coverage area of only 40.9 ± 10.9 nm^2, or an average pillar diameter of 7.2 ± 1.4 nm (Figure 4.2 a,d). If the BCP porous template is etched for 10 s in oxygen/argon RIE, the average pillar coverage area increases to 176.2 ± 29.5 nm2, or an average pillar diameter of 15.0 ± 1.2 nm (Figure 4.2 b,e). This represents a 303% increase of the pillar coverage area when compared to the pattern transfer with the unetched template. On the other hand, increasing the RIE exposure time of the BCP mask to 20 s decreases the silicon oxide pillar coverage area to 117.5 ± 27.5 nm^2, or pillar diameter of 12.2 ± 1.4 nm (Figure 4.2 c,f). Pillar size reduction can be attributed to the decrease in the film thickness of the template after RIE. Tilt-view SEM cross-section images are used to characterize the profile of the silicon oxide pillars (Figure 4.3). An average pillar height of 14.0 ± 1.0 nm was measured from the images. It can be seen that the pillars have a cylindrical shape and extend down to the surface of substrate. The silicon oxide pillars obtained from the porous template show high fidelity to the negative porous BCP templates, maintaining a pitch of approximately 24.3 ± 2.2 nm and varying the feature size only by 5%, further confirming the viability of the proposed method.

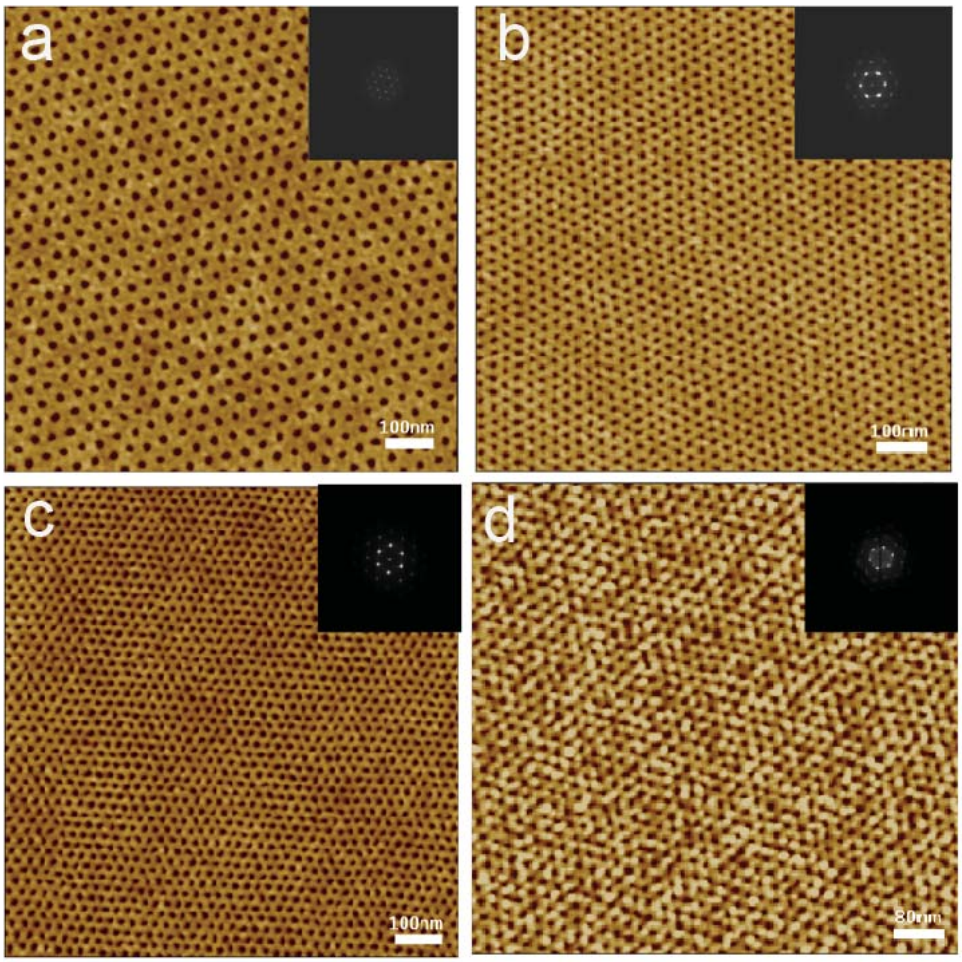

Figure 4.4 The SFM height image of block copolymer porous template. a) reconstructed surface of PS-*b*-P2VP 77k. b) reconstructed surface of PS-*b*-P4VP 24K. c) reconstructed surface of PS-*b*-P2VP 20K. d) reconstructed surface of PS-*b*-P4VP 15K

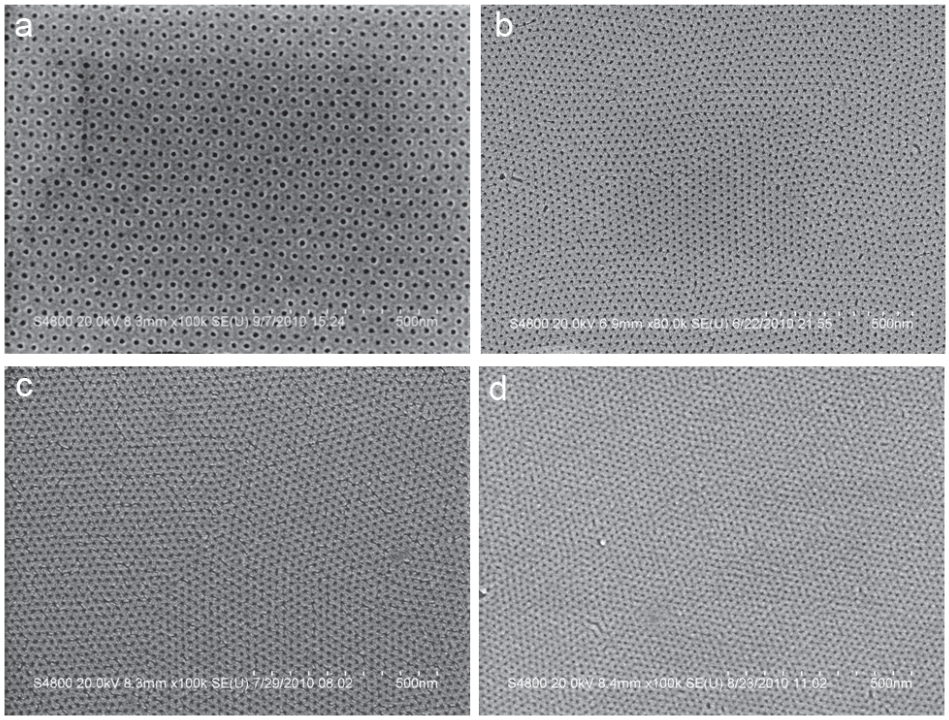

Figure 4.5 The SEM image of block copolymer porous template. a) Reconstructed surface of PS-*b*-P2VP 77k, b) reconstructed surface of PS-*b*-P4VP 24k, c) reconstructed surface of PS-*b*-P2VP 20K, d) reconstructed surface of PS-*b*-P4VP 15K

Table 4.1: Area density information of silicon oxide pillar

Polymer name Molecular weight kg/mol	PS-*b*-P2VP 77	PS-*b*-P4VP 24	PS-*b*-P2VP 20	PS-*b*-P4VP 15
Volume fraction of minor domain	27%	21%	18%	21%
Pitch distance (nm)	32.9	24.3	19.5	17.0
Area density (Tera dots/ inch^2)	0.5	1.0	1.5	2.0

Control of the silicon oxide pillar pitch can be obtained by changing the molecular weight of the polymer blocks in the BCP template. Four different molecular weights of cylindrical forming PS-*b*-PVP were used to prepare the reconstructed porous templates, resulting in BCP films with different pore size and domain spacing (refer to Table 4.1). All the unetched BCP porous films were examined by scanning force microscopy (SFM) in the height mode (Figure 4.4) and SEM (Figure 4.5). The average pitches and areal densities are listed in Table 4.1. As the molecular weight of the BCP increases, the average pitch in the films increases from 17.0 to 32.9 nm. Access to a wider range of pitches can be obtained by further modifying the molecular weight of the BCP. Silicon oxide pillars were obtained from the porous BCP films with different molecular weights (Figure 4.6~7). 10 s of RIE was applied to the BCP porous templates to enlarge the pore size and sample preparation proceeded as previously described (refer to Schematic 4.1). The pitch from the BCP template was maintained after transfer to silicon oxide pillars. Areal densities of silicon oxide pillars as high as 2 Tera dots/inch^2 were obtained. These results show that by changing the molecular weight of BCP, the pitch of the silicon oxide pillar patterns can be controlled. Moreover, combined with control over feature size in the BCP template by RIE, control over both the pitch and feature size of the silicon oxide pillar patterns can be obtained.

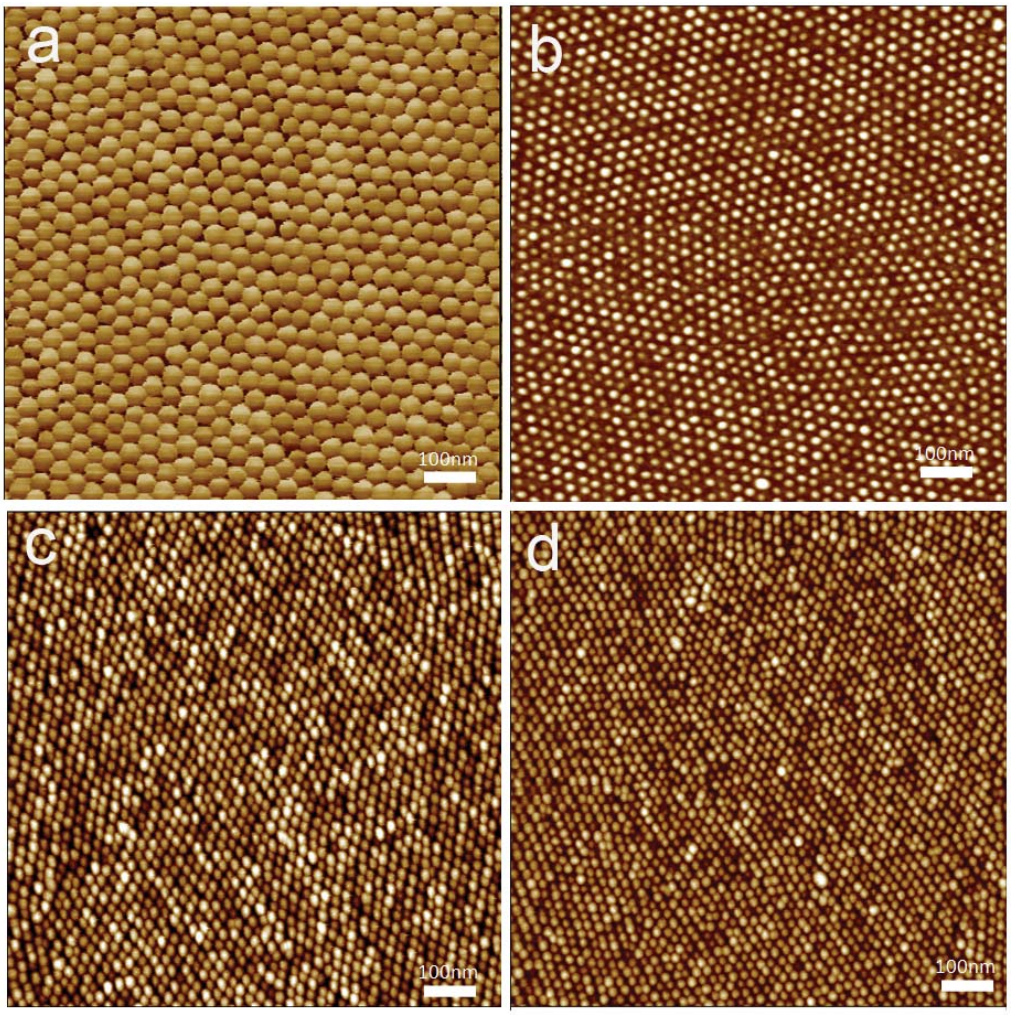

Figure 4.6 The SFM height image of silicon pillar from block copolymer template. a) silicon pillar from PS-*b*-P2VP 77k template, b) silicon pillar from PS-*b*-P4VP 24k template, c) silicon pillar from PS-*b*-P2VP 20K template, d) silicon pillar from PS-*b*-P4VP 15K template.

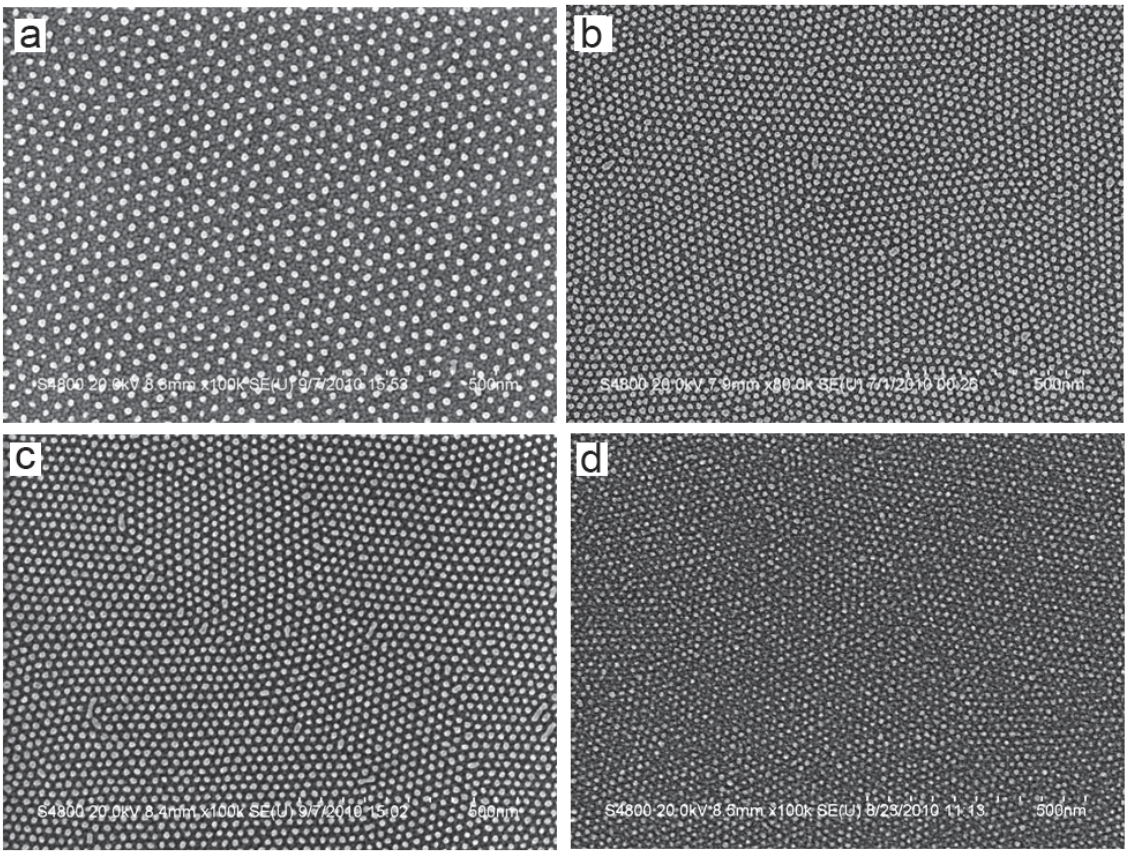

Figure 4.7 The SEM height image of silicon pillar from block copolymer porous template. a) silicon pillar from PS-*b*-P2VP 77k template, b) silicon pillar from PS-*b*-P4VP 24k template, c) silicon pillar from PS-*b*-P2VP 20K template, d) silicon pillar from PS-*b*-P4VP 15K template.

4.3.3. Pattern transfer from silicon oxide pillars to carbon layer

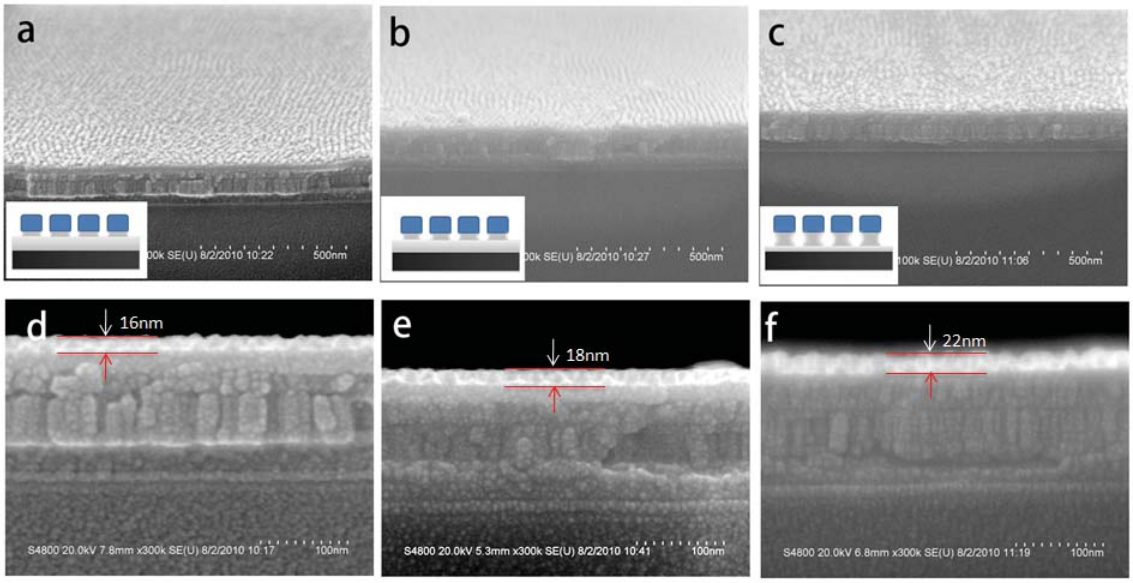

Figure 4.8 SEM cross section of Silicon pillar on media substrate with different amount of etching time. a) and d) after 20 seconds oxygen plasma etching. b) and e) after 40 seconds oxygen plasma etching. c) and f) after 70 seconds oxygen plasma etching. a) b) and c) samples are tilted for 75 degree. d), e), and f) samples are tilted for 90 degree. Inserted images schematic drawing of those pillar patterns.

Table 4.2: Height information of silicon oxide pillars for different etch times.

RIE exposure time (seconds)	0	20	40	70	100
Height of pillar (nm)	14	16	18	22	n/a

Silicon oxide pillars are an ideal etch mask in applications involving pattern transfer. Figure 4.8 shows SEM images of samples where silicon oxide pillar masks are used to transfer patterns into an underlying diamond-like carbon (DLC) layer. The same procedure described in Schematic 4.1 is used to generate silicon oxide pillar on DLC

layer. Pattern transfer under different oxygen/ argon RIE exposure times is demonstrated. The SEM cross-sectional images show that the height of pillar patterns increases from 14 nm to 22 nm by increasing the RIE exposure time (refer to Table 4.2). An undercutting is observed in the pattern transfer when the etching time is increased to 100 s, due to the isotropic nature of RIE. Better directionality could be achieved by inductively coupled plasma (ICP) RIE.

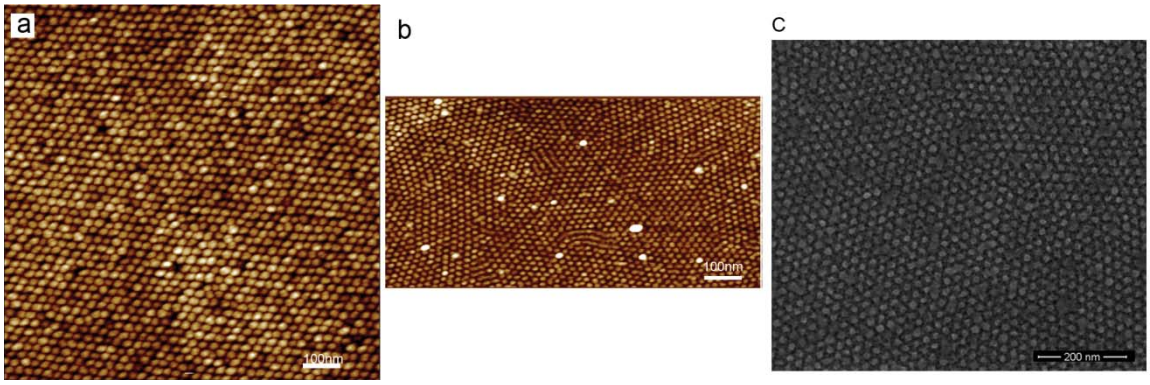

Figure 4.9 a)SFM height image of gold pillar made from porous block copolymer template, b) SFM height image, c) SEM image of Pt pillar made from porous block copolymer template

Finally, we used precursors other than PDMS to make metal nanodots, demonstrating the generality of the strategy in this work. Typically, metal nanodots templated from self-assembled BCPs require one of the blocks to coordinate with the metal salts to form a metal complex[14]. Here, a metal salt precursor solution is spin-coated onto the porous template, baked and subsequently etched to make metal nano-dots. Figure 4.9a shows gold nanodots made from back filling chloroauric acid precursor dissolved in ethanol. Platinum nanodots were made from spin-coating sodium tetrachloroplatinate (II) hydrate in hexane (Figure 4.9b,c). Depending on the application, different metal precursors can used. For example, a magnetic metal precursor, like a

cobalt salt, can be backfilled to make magnetic nanodots. This methodology provides a general and flexible approach to a high density of functional metal nanodots.

4.4. Conclusions

In summary, we have demonstrated a method to make silicon oxide pillars with tunable feature sizes and pitches. By using RIE, the feature size of silicon oxide pillars can be tuned without affecting the pitch. Areal densities up to 2 teradots/inch^2 of silicon oxide pillars were achieved along with the pattern transfer of silicon oxide pillar to DLC. This method can be extended to generate a range of different metal nanodots, including gold, platinum or chromium.

4.5. References

[1] G. E. Moore, **1965**.

[2] A. E. Grigorescu, C. W. Hagen, *Nanotechnology* **2009**, *20*, DOI 10.1088/0957-4484/20/29/292001.

[3] L. J. Guo, *Adv Mater* **2007**, *19*, 495.

[4] H. Schift, *J. Vac. Sci. Technol. B* **2008**, *26*, 458.

[5] S. Park, D. H. Lee, J. Xu, B. Kim, S. W. Hong, U. Jeong, T. Xu, T. P. Russell, *Science* **2009**, *323*, 1030.

[6] R. Ruiz, H. Kang, F. A. Detcheverry, E. Dobisz, D. S. Kercher, T. R. Albrecht, J. J. de Pablo, P. F. Nealey, *Science* **2008**, *321*, 936.

[7] I. Bita, J. K. W. Yang, Y. S. Jung, C. A. Ross, E. L. Thomas, K. K. Berggren, *Science* **2008**, *321*, 939.

[8] S. Park, B. Kim, A. Cirpan, T. P. Russell, *Small* **2009**, *5*, 1343.

[9] S. Park, O. Yavuzcetin, B. Kim, M. T. Tuominen, T. P. Russell, *Small* **2009**, *5*, 1064.

[10] S. Park, B. Kim, J. Xu, T. Hofmann, B. M. Ocko, T. P. Russell, *Macromolecules*

2009, *42*, 1278.

[11] S. Park, B. Kim, O. Yavuzcetin, M. T. Tuominen, T. P. Russell, *ACS nano* **2008**, *2*, 1363.

[12] S. Park, J.-Y. Wang, B. Kim, J. Xu, T. P. Russell, *ACS nano* **2008**, *2*, 766.

[13] S. Park, B. Kim, J. Y. Wang, T. P. Russell, *Adv Mater* **2008**, *20*, 681.

[14] S. Park, J.-Y. Wang, B. Kim, T. P. Russell, *Nano Lett.* **2008**, *8*, 1667.

[15] S. Park, J. Y. Wang, B. Kim, W. Chen, T. P. Russell, *Macromolecules* **2007**, *40*, 9059.

[16] R. Ruiz, J. K. Bosworth, C. T. Black, *Phys. Rev. B* **2008**, *77*, DOI 10.1103/PhysRevB.77.054204.

[17] Gu, X.; Gunkel, I.; Russell, T. P. *Phil. Trans. R. Soc. A* **2013**, **371**, 20120306,

[18] Y. S. Jung, C. A. Ross, *Nano Lett.* **2007**, *7*, 2046.

[19] Y. S. Jung, J. B. Chang, E. Verploegen, K. K. Berggren, C. A. Ross, *Nano Lett.* **2010**, *10*, 1000.

[20] Y. S. Jung, C. A. Ross, *Small* **2009**, *5*, 1654.

[21] Y. S. Jung, C. A. Ross, *Adv Mater* **2009**, *21*, 2540.

[22] S. G. Xiao, X. M. Yang, S. J. Park, D. Weller, T. P. Russell, *Adv Mater* **2009**, *21*, 2516.

[23] T. Hirai, M. Leolukman, C.-C. Liu, E. Han, Y. J. Kim, Y. Ishida, T. Hayakawa, M.-A. Kakimoto, P. F. Nealey, P. Gopalan, *Adv Mater* **2009**, *21*, 4334.

[24] T. Hirai, M. Leolukman, S. Jin, R. Goseki, Y. Ishida, M.-A. Kakimoto, T. Hayakawa, M. Ree, P. Gopalan, *Macromolecules* **2009**, *42*, 8835.

[25] F. S. Bates, G. H. Fredrickson, *Annual Review of Physical Chemistry* **1990**, *41*, 525.

[26] T. Xu, J. Stevens, J. A. Villa, J. T. Goldbach, K. W. Guarini, C. T. Black, C. J. Hawker, T. P. Russell, *Advanced Functional Materials* **2003**, *13*, 698.

CHAPTER 5

FUTURE DIRECTIONS

5.1. Future directions

Ever since the first application of BCP lithography for patterning of nanostructures in 1997, enormous progress has been made in this area. BCP lithography has now established itself as a viable strategy for patterning nanostructures. The areal density of BCP microdomains has been improved by a factor of 25 to 10 teradots per $inch^2$, and a resolution as small as 3 nm was achieved[1]. Precise control over orientation and lateral ordering of BCP domains was achieved by using both neutral brush layers and DSA. Recently, the DSA of BCPs has been recognized as a promising route for future patterning technologies in the International Technology Roadmap for Semiconductors (ITRS)[2]. BCP lithography not only finds its application in the silicon conductor industry[3], but also shows a variety of other potential applications, such as bit-patterned media applications[4], antireflective coatings[5], patterning graphene transistors[6], biosensors [7] or surface-enhanced Raman spectroscopy (SERS)[8]. Overall, BCP lithography has now proved to be a powerful nanoscale patterning technique along with other patterning techniques. There are still, though, many challenges ahead that need to be addressed before BCP lithography can be integrated into industrial processes.

First, in order to advance BCP lithography to the sub-10nm regime, new materials with high Flory–Huggins interaction parameter χ and high etch resistance need to be designed and synthesized. Reducing the molecular weight of the BCP is a typical means to increase the resolution of BCP lithography. However, χN, the incompatibility between

the blocks, is required to be larger than 10.5 in order to maintain a microphase-separated structure according to mean-field theory. This limits low-χ BCPs such as PS-*b*-PMMA ($\chi \sim 0.043$) to form ordered structures with minimal periods of 20 nm. In addition, a large unfavourable interaction between two blocks reduces the interfacial thickness between the different blocks, thus reducing the line-edge roughness of the BCP. Equally important is that the etch resistance of the mask needs to be improved. Reducing the size of the mask reduces the thickness of the mask at the same time, since both quantities scale with the period of the BCP domains. Therefore, an etching recipe needs to be developed that provides a high selectivity between the polymer mask and the material to which the pattern is being transferred. A sub-10 nm dry-etching pattern transfer remains a challenge owing to a significantly slower diffusion of gas ions that are confined to nanoscopic space.

The defect density in ordered BCP patterns must not exceed 0.01 defects cm−2 at the resist level for all device types according to ITRS[2], which requires BCPs to phase separate and to reduce defects within a reasonable amount of annealing time. Understanding the origin of the formation of defects and methods to annihilate defects in BCP thin films is important. Real-time scanning force microcopy or electron microdcopy will be a better fit to understand defect annihilation compared to X-ray scattering.

Second, complex integrated circuit (IC) structures, such as bends and joints, still remain a challenge for BCP lithography. However, progress has been made using the DSA of BCPs on either topography or chemistry contrast. For example, BCPs blended with homopolymers were shown to form a sharp bend structure [9]; the assembly of complex PS-*b*-PDMS patterns has been directed using HSQ pillars, which were patterned

by e-beam lithography[10]. Using BCP lithography to generate even more complex three-dimensional structures has not yet been extensively explored. Intel recently introduced the 'tri-gate transistor technology', taking device fabrication into three dimensions. The use of BCPs that consist of multiple blocks has the potential to create complex three-dimensional structures[11].

Although there are still challenges to be overcome before the incorporation of BCPs into the semiconductor manufacturing process, tremendous progress has been made in the past decades. Continued research holds promise for an exciting future for the DSA of BCPs in two- and three-dimensional configurations.

5.2. References

(1) Park, S.; Lee, D. H.; Xu, J.; Kim, B.; Hong, S. W.; Jeong, U.; Xu, T.; Russell, T. P. *Science* **2009**, *323*, 1030–1033.

(2) ITRS. **2011**.

(3) Black, C. T.; Ruiz, R.; Breyta, G.; Cheng, J. Y.; Colburn, M. E.; Guarini, K. W.; Kim, H. C.; Zhang, Y. *IBM J. Res. Dev.* **2007**, *51*, 605–633.

(4) Ross, C. A.; Cheng, J. Y. *MRS Bulletin* **2008**, *33*, 838–845.

(5) Päivänranta, B.; Sahoo, P. K.; Tocce, E.; Auzelyte, V.; Ekinci, Y.; Solak, H. H.; Liu, C.-C.; Stuen, K. O.; Nealey, P. F.; David, C. *ACS nano* **2011**, *5*, 1860–1864.

(6) Bai, J.; Zhong, X.; Jiang, S.; Huang, Y.; Duan, X. *Nat. Nanotechnol.* **2010**, *5*, 190–194.

(7) Jung, Y. S.; Jung, W.; Tuller, H. L.; Ross, C. A. *Nano Lett.* **2008**, *8*, 3776–3780.

(8) Lu, J.; Chamberlin, D.; Rider, D. A.; Liu, M.; Manners, I.; Russell, T. P. *Nanotechnology* **2006**, *17*, 5792–5797.

(9) Stoykovich, M. P.; Muller, M.; Kim, S. O.; Solak, H. H.; Edwards, E. W.; de Pablo, J. J.; Nealey, P. F. *Science* **2005**, *308*, 1442–1446.

(10) Tavakkoli K G, A.; Gotrik, K. W.; Hannon, A. F.; Alexander Katz, A.; Ross, C.

A.; Berggren, K. K. *Science* **2012**, *336*, 1294–1298.

(11) Bates, F. S.; Hillmyer, M. A.; Lodge, T. P.; Bates, C. M.; Delaney, K. T.; Fredrickson, G. H. *Science* **2012**, *336*, 434–440.

BIBLIOGRAPHY

Albalak, R. J.; Capel, M. S.; Thomas, E. L. *Polymer* **1998**, *39*, 1647–1656.

Albert, J. N. L.; Bogart, T. D.; Lewis, R. L.; Beers, K. L.; Fasolka, M. J.; Hutchison, J. B.; Vogt, B. D.; Epps, T. H. *Nano Lett.* **2011**, *11*, 1351–1357.

Albert, J. N. L.; Young, W.-S.; Lewis, R. L., III; Bogart, T. D.; Smith, J. R.; Epps, T. H., III. *ACS nano* **2012**, *6*, 459–466.

Bai, J.; Zhong, X.; Jiang, S.; Huang, Y.; Duan, X. *Nat. Nanotechnol.* **2010**, *5*, 190–194.

Bang, J.; Jeong, U.; Ryu, D. Y.; Russell, T. P.; Hawker, C. J. *Adv Mater* **2009**, *21*, 4769–4792.

Bates, C. M.; Seshimo, T.; Maher, M. J.; Durand, W. J.; Cushen, J. D.; Dean, L. M.; Blachut, G.; Ellison, C. J.; Willson, C. G. *Science* **2012**, *338*, 775–779.

Bates, F. S.; Fredrickson, G. H. *Annual Review of Physical Chemistry* **1990**, *41*, 525–557.

Bates, F. S.; Fredrickson, G. H. *Physics Today* **1999**, *52*, 32–38.

Bates, F. S.; Hillmyer, M. A.; Lodge, T. P.; Bates, C. M.; Delaney, K. T.; Fredrickson, G. H. *Science* **2012**, *336*, 434–440.

Berry, B. C.; Bosse, A. W.; Douglas, J. F.; Jones, R. L.; Karim, A. *Nano Lett.* **2007**, *7*, 2789–2794.

Bita, I.; Yang, J. K. W.; Jung, Y. S.; Ross, C. A.; Thomas, E. L.; Berggren, K. K. *Science* **2008**, *321*, 939–943.

Black, C. T.; Ruiz, R.; Breyta, G.; Cheng, J. Y.; Colburn, M. E.; Guarini, K. W.; Kim, H. C.; Zhang, Y. *IBM J. Res. Dev.* **2007**, *51*, 605–633.

Borah, D.; Shaw, M. T.; Rasappa, S.; Farrell, R. A.; O'Mahony, C.; Faulkner, C. M.; Bosea, M.; Gleeson, P.; Holmes, J. D.; Morris, M. A. *J Phys D Appl Phys* **2011**, *44*, 4012.

Bosworth, J. K.; Paik, M. Y.; Ruiz, R.; Schwartz, E. L.; Huang, J. Q.; Ko, A. W.; Smilgies, D.-M.; Black, C. T.; Ober, C. K. *ACS nano* **2008**, *2*, 1396–1402.

Brandrup, J. I.; Immergut, E. H.; Grulke, E. A.; Grulke, A. *Polymer Handbook*; 4 ed.; Wiely: New York, 1999.

Castelletto, V.; Hamley, I. W. *Current Opinion in Solid State and Materials Science* **2004**, *8*, 426–438.

Cavicchi, K. A.; Berthiaume, K. J.; Russell, T. P. *Polymer* **2005**, *46*, 11635–11639.

Cavicchi, K. A.; Russell, T. P. *Macromolecules* **2007**, *40*, 1181–1186.

Chai, J.; Buriak, J. M. *ACS nano* **2008**, *2*, 489–501.

Chai, J.; Wang, D.; Fan, X. N.; Buriak, J. M. *Nat. Nanotechnol.* **2007**, *2*, 500–506.

Cheng, J. Y.; Mayes, A. M.; Ross, C. A. *Nature Materials* **2004**, *3*, 823–828.

Cheng, J. Y.; Ross, C. A.; Thomas, E. L.; Smith, H. I.; Vancso, G. J. *Appl. Phys. Lett.* **2002**, *81*, 3657–3659.

Cheng, J.; Ross, C.; Chan, V.; Thomas, E.; Lammertink, R.; Vancso, G. *Adv Mater* **2001**, *13*, 1174–1178.

Chourou, S. T.; Sarje, A.; Li, X. S.; Chan, E. R.; Hexemer, A. *J Appl Cryst* **2013**, 1–15.

Cochran, E. W.; Morse, D. C.; Bates, F. S. *Macromolecules* **2003**, *36*, 782–792.

Dai, K. H.; Kramer, E. J. *Polymer* **1994**, *35*, 157–161.

Di, Z.; Posselt, D.; Smilgies, D.-M.; Li, R.; Rauscher, M.; Potemkin, I. I.; Papadakis, C. M. *Macromolecules* **2012**, *45*, 5185–5195.

Di, Z.; Posselt, D.; Smilgies, D.-M.; Papadakis, C. M. *Macromolecules* **2010**, *43*, 418–427.

Farrell, R. A.; Petkov, N.; Shaw, M. T.; Djara, V.; Holmes, J. D.; Morris, M. A. *Macromolecules* **2010**, *43*, 8651–8655.

Fox, T. G.; Loshaek, S. *J. Polym. Sci.* **1955**, *15*, 371–390.

Gotrik, K. W.; Hannon, A. F.; Son, J. G.; Keller, B.; Alexander-Katz, A.; Ross, C. A. *ACS nano* **2012**, *6*, 8052–8059.

Grigorescu, A. E.; Hagen, C. W. *Nanotechnology* **2009**, *20*.

Gu, W.; Hong, S. W.; Russell, T. P. *ACS nano* **2012**, *6*, 10250–10257.

Gu, W.; Huh, J.; Hong, S. W.; Sveinbjornsson, B. R.; Park, C.; Grubbs, R. H.; Russell, T. P. *ACS nano* **2013**, *7*, 2551–2558.

Gu, X.; Dorsey, P.; Russell, T. P. *Adv Mater* **2012**, *24*, 5505–5511.

Gu, X.; Gunkel, I.; Russell, T. P. *Phil. Trans. R. Soc. A* **2013**, **371**, 20120306.

Gu, X.; Liu, Z.; Gunkel, I.; Chourou, S. T.; Hong, S. W.; Olynick, D. L.; Russell, T. P. *Adv Mater* **2012**, *24*, 5688–5694.

Guo, L. J. *Adv Mater* **2007**, *19*, 495–513.

Hamley, I. W. *Prog. Polym. Sci.* **2009**, *34*, 1161–1210.

Hashimoto, T.; Bodycomb, J.; Funaki, Y.; Kimishima, K. *Macromolecules* **1999**, *32*, 952–954.

Hawker, C. J.; Russell, T. P. *MRS Bulletin* **2005**, *30*, 952–966.

Helfand, E. *Macromolecules* **1975**, *8*, 552–556.

Helfand, E.; TAGAMI, Y. *The Journal of chemical physics* **1972**, *56*, 3592–3601.

Helfand, E.; Wasserman, Z. R. *Macromolecules* **1976**, *9*, 879–888.

Hirai, T.; Leolukman, M.; Jin, S.; Goseki, R.; Ishida, Y.; Kakimoto, M.-A.; Hayakawa, T.; Ree, M.; Gopalan, P. *Macromolecules* **2009**, *42*, 8835–8843.

Hirai, T.; Leolukman, M.; Liu, C.-C.; Han, E.; Kim, Y. J.; Ishida, Y.; Hayakawa, T.; Kakimoto, M.-A.; Nealey, P. F.; Gopalan, P. *Adv Mater* **2009**, *21*, 4334–4338.

Hong, S. W.; Gu, X.; Huh, J.; Xiao, S.; Russell, T. P. *ACS nano* **2011**, *5*, 2855–2860.

Hong, S. W.; Huh, J.; Gu, X.; Lee, D. H.; Jo, W. H.; Park, S.; Xu, T.; Russell, T. P. *Proceedings of the National Academy of Sciences* **2012**, *109*, 1402–1406.

Horvat, A.; Knoll, A.; Krausch, G.; Tsarkova, L.; Lyakhova, K. S.; Sevink, G. J. A.; Zvelindovsky, A. V.; Magerle, R. *Macromolecules* **2007**, *40*, 6930–6939.

Ilavsky, J. *J Appl Crystallogr* **2012**, *45*, 324–328.

ITRS. **2011**.

Jackson, E. A.; Hillmyer, M. A. *ACS nano* **2010**, *4*, 3548–3553.

Jane, A.; Dronov, R.; Hodges, A.; Voelcker, N. H. *Trends Biotechnol* **2009**, *27*, 230–239.

Jeong, J. W.; Park, W. I.; Kim, M.-J.; Ross, C. A.; Jung, Y. S. *Nano Lett.* **2011**, *11*, 4095–4101.

Jung, Y. S.; Chang, J. B.; Verploegen, E.; Berggren, K. K.; Ross, C. A. *Nano Lett.* **2010**, *10*, 1000–1005.

Jung, Y. S.; Jung, W.; Ross, C. A. *Nano Lett.* **2008**, *8*, 2975–2981.

Jung, Y. S.; Jung, W.; Tuller, H. L.; Ross, C. A. *Nano Lett.* **2008**, *8*, 3776–3780.

Jung, Y. S.; Ross, C. A. *Adv Mater* **2009**, *21*, 2540–2545.

Jung, Y. S.; Ross, C. A. *Nano Lett.* **2007**, *7*, 2046–2050.

Jung, Y. S.; Ross, C. A. *Small* **2009**, *5*, 1654–1659.

Kennemur, J. G.; Hillmyer, M. A.; Bates, F. S. *Macromolecules* **2012**, *45*, 7228–7236.

Kim, E.; Ahn, H.; Park, S.; Lee, H.; Lee, M.; Lee, S.; Kim, T.; Kwak, E.-A.; Lee, J. H.; Lei, X.; Huh, J.; Bang, J.; Lee, B.; Ryu, D. Y. *ACS nano* **2013**, *7*, 1952–1960.

Kim, G.; Libera, M. *Macromolecules* **1998**, *31*, 2569–2577.

Kim, G.; Libera, M. *Macromolecules* **1998**, *31*, 2670–2672.

Kim, S. H.; Misner, M. J.; Russell, T. P. *Adv Mater* **2008**, *20*, 4851–4856.

Kim, S. H.; Misner, M. J.; Xu, T.; Kimura, M.; Russell, T. P. *Adv Mater* **2004**, *16*, 226–231.

Kim, S. H.; Misner, M. J.; Yang, L.; Gang, O.; Ocko, B. M.; Russell, T. P. *Macromolecules* **2006**, *39*, 8473–8479.

Kim, S. O.; Solak, H. H.; Stoykovich, M. P.; Ferrier, N. J.; de Pablo, J. J.; Nealey, P. F. *Nature* **2003**, *424*, 411–414.

Knoll, A.; Horvat, A.; Lyakhova, K.; Krausch, G.; Sevink, G.; Zvelindovsky, A.; Magerle, R. *Physical Review Letters* **2002**, *89*, 035501.

Knoll, A.; Lyakhova, K. S.; Horvat, A.; Krausch, G.; Sevink, G. J. A.; Zvelindovsky, A. V.; Magerle, R. *Nature Materials* **2004**, *3*, 886–891.

Lai, C.; Russel, W. B.; Register, R. A. *Macromolecules* **2002**, *35*, 4044–4049.

Lammertink, R. G. H.; Hempenius, M. A.; Van den Enk, J. E.; Chan, V. Z. H.; Thomas, E. L.; Vancso, G. J. *Adv Mater* **1999**, *12*, 98–103.

Lammertink, R.; Hempenius, M.; van den Enk, J.; Chan, V.; Thomas, E.; Vancso, G. *Adv Mater* **2000**, *12*, 98–103.

Leibler, L. *Macromolecules* **1980**, *13*, 1602–1617.

Lin, Z. Q.; Kim, D. H.; Wu, X. D.; Boosahda, L.; Stone, D.; LaRose, L.; Russell, T. P. *Adv Mater* **2002**, *14*, 1373–1376.

Liu, C.-C.; Nealey, P. F.; Ting, Y.-H.; Wendt, A. E. *J. Vac. Sci. Technol. B* **2007**, *25*, 1963–1968.

Liu, Z.; Wu, Y.; Harteneck, B.; Olynick, D. *Nanotechnology* **2012**, *24*, 015305.

Lodge, T. P.; Hanley, K. J.; Pudil, B.; Alahapperuma, V. *Macromolecules* **2003**, *36*, 816–822.

Lodge, T. P.; Pan, C.; Jin, X.; Liu, Z.; Zhao, J.; Maurer, W. W.; Bates, F. S. *J. Polym. Sci. B Polym. Phys.* **1995**, *33*, 2289–2293.

Lu, J.; Chamberlin, D.; Rider, D. A.; Liu, M.; Manners, I.; Russell, T. P. *Nanotechnology* **2006**, *17*, 5792–5797.

Mansky, P.; Chaikin, P.; Thomas, E. L. *Journal of Materials Science* **1995**, *30*, 1987–1992.

Mansky, P.; Liu, Y.; Huang, E.; Russell, T. P.; Hawker, C. *Science* **1997**, *275*, 1458–1460.

Matsen, M. W.; Bates, F. S. *Macromolecules* **1996**, *29*, 1091–1098.

Matsen, M. W.; Schick, M. *Physical Review Letters* **1994**, *72*, 2660.

Meier, D. J. *Journal of Polymer Science Part C-Polymer Symposium* **1969**, 81–98.

Miyake, G. M.; Piunova, V. A.; Weitekamp, R. A.; Grubbs, R. H. *Angew. Chem.-Int. Edit.* **2012**, *51*, 11246–11248.

Moore, G. E. **1965**.

Mori, K.; Hasegawa, H.; Hashimoto, T. *Polymer* **2001**, *42*, 3009–3021.

Mori, K.; Okawara, A.; Hashimoto, T. *The Journal of chemical physics* **1996**, *104*, 7765.

Morkved, T. L.; Lu, M.; Urbas, A. M.; Ehrichs, E. E.; Jaeger, H. M.; Mansky, P.; Russell, T. P. *Science* **1996**, *273*, 931–933.

Paik, M. Y.; Bosworth, J. K.; Smilges, D. M.; Schwartz, E. L.; Andre, X.; Ober, C. K. *Macromolecules* **2010**, *43*, 4253–4260.

Päivänranta, B.; Sahoo, P. K.; Tocce, E.; Auzelyte, V.; Ekinci, Y.; Solak, H. H.; Liu, C.-C.; Stuen, K. O.; Nealey, P. F.; David, C. *ACS nano* **2011**, *5*, 1860–1864.

Papadakis, C. M.; Di, Z.; Posselt, D.; Smilgies, D.-M. *Langmuir* **2008**, *24*, 13815–13818.

Park, M.; Harrison, C.; Chaikin, P. M.; Register, R. A.; Adamson, D. H. *Science* **1997**, *276*, 1401–1404.

Park, S.-M.; Berry, B. C.; Dobisz, E.; Kim, H.-C. *Soft Matter* **2009**, *5*, 957–961.

Park, S.; Kim, B.; Cirpan, A.; Russell, T. P. *Small* **2009**, *5*, 1343–1348.

Park, S.; Kim, B.; Wang, J. Y.; Russell, T. P. *Adv Mater* **2008**, *20*, 681–685.

Park, S.; Kim, B.; Xu, J.; Hofmann, T.; Ocko, B. M.; Russell, T. P. *Macromolecules* **2009**, *42*, 1278–1284.

Park, S.; Kim, B.; Yavuzcetin, O.; Tuominen, M. T.; Russell, T. P. *ACS nano* **2008**, *2*, 1363–1370.

Park, S.; Lee, D. H.; Xu, J.; Kim, B.; Hong, S. W.; Jeong, U.; Xu, T.; Russell, T. P. *Science* **2009**, *323*, 1030–1033.

Park, S.; Wang, J. Y.; Kim, B.; Chen, W.; Russell, T. P. *Macromolecules* **2007**, *40*, 9059–9063.

Park, S.; Wang, J.-Y.; Kim, B.; Russell, T. P. *Nano Lett.* **2008**, *8*, 1667–1672.

Park, S.; Wang, J.-Y.; Kim, B.; Xu, J.; Russell, T. P. *ACS nano* **2008**, *2*, 766–772.

Park, S.; Yavuzcetin, O.; Kim, B.; Tuominen, M. T.; Russell, T. P. *Small* **2009**, *5*, 1064–1069.

Park, W. I.; Kim, K.; Jang, H.-I.; Jeong, J. W.; Kim, J. M.; Choi, J.; Park, J. H.; Jung, Y. S. *Small* **2012**, *8*, 3762–3768.

Peng, Q.; Tseng, Y.-C.; Darling, S. B.; Elam, J. W. *ACS nano* **2011**, *5*, 4600–4606.

Peng, Q.; Tseng, Y.-C.; Darling, S. B.; Elam, J. W. *Adv Mater* **2010**, *22*, 5129–5133.

Ren, Y.; Lodge, T. P.; Hillmyer, M. A. *Macromolecules* **2000**, *33*, 866–876.

Rockford, L.; Liu, Y.; Mansky, P.; Russell, T.; Yoon, M.; Mochrie, S. *Physical Review Letters* **1999**, *82*, 2602–2605.

Ross, C. A.; Cheng, J. Y. *MRS Bulletin* **2008**, *33*, 838–845.

Ruiz, R.; Bosworth, J. K.; Black, C. T. *Phys. Rev. B* **2008**, *77*.

Ruiz, R.; Kang, H.; Detcheverry, F. A.; Dobisz, E.; Kercher, D. S.; Albrecht, T. R.; de Pablo, J. J.; Nealey, P. F. *Science* **2008**, *321*, 936–939.

Russell, T. P.; Hjelm, R. P., Jr; Seeger, P. A. *Macromolecules* **1990**, *23*, 890–893.

Russell, T. P.; Mayes, A. M.; Kunz, M. S. In *Ordering in Macromolecular Systems*; Springer Berlin Heidelberg: Berlin, Heidelberg, 1994; pp. 217–223.

Ryu, D. Y.; Shin, K.; Drockenmuller, E.; Hawker, C. J.; Russell, T. P. *Science* **2005**, *308*, 236–239.

Schift, H. *J. Vac. Sci. Technol. B* **2008**, *26*, 458–480.

Segalman, R. A.; Yokoyama, H.; Kramer, E. J. *Adv Mater* **2001**, *13*, 1152–1155.

Seppala, J. E.; Lewis, R. L., III; Epps, T. H., III. *ACS nano* **2012**, *6*, 9855–9862.

Shibayama, M.; Hashimoto, T.; Hasegawa, H.; Kawai, H. *Macromolecules* **1983**, *16*, 1427–1433.

Shull, K. R. *Macromolecules* **1992**, *25*, 2122–2133.

Sinturel, C.; Vayer, M.; Morris, M.; Hillmyer, M. A. *Macromolecules* **2013**, *46*, 5399–5415.

Smilgies, D.-M.; Busch, P.; Papadakis, C. M.; Posselt, D. *Synchrotron Radiation News* **2002**, *15*, 35–42.

Stafford, C. M.; Russell, T. P.; McCarthy, T. J. *Macromolecules* **1999**, *32*, 7610–7616.

Stewart, M.; Buriak, J. *Adv Mater* **2000**, *12*, 859–869.

Stoykovich, M. P.; Muller, M.; Kim, S. O.; Solak, H. H.; Edwards, E. W.; de Pablo, J. J.; Nealey, P. F. *Science* **2005**, *308*, 1442–1446.

Tanaka, T.; Morigami, M.; Atoda, N. *Japanese Journal of Applied Physics* **1993**, *32*, 6059–6064.

Tang, C.; Lennon, E. M.; Fredrickson, G. H.; Kramer, E. J.; Hawker, C. J. *Science* **2008**, *322*, 429–432.

Tavakkoli K G, A.; Gotrik, K. W.; Hannon, A. F.; Alexander Katz, A.; Ross, C. A.; Berggren, K. K. *Science* **2012**, *336*, 1294–1298.

Thurn-Albrecht, T.; Schotter, J.; Kästle, G. A.; Emley, N.; Shibauchi, T.; Krusin-Elbaum, L.; Guarini, K.; Black, C. T.; Tuominen, M. T.; Russell, T. P. *Science* **2000**, *290*, 2126–2129.

Thurn-Albrecht, T.; Steiner, R.; DeRouchey, J.; Stafford, C. M.; Huang, E.; Bal, M.; Tuominen, M.; Hawker, C. J.; Russell, T. P. *Adv Mater* **2000**, *12*, 787–791.

Tseng, Y.-C.; Peng, Q.; Ocola, L. E.; Elam, J. W.; Darling, S. B. *J. Phys. Chem. C* **2011**, *115*, 17725–17729.

Wang, J. Y.; Chen, W.; Roy, C.; Sievert, J. D.; Russell, T. P. *Macromolecules* **2008**, *41*, 963–969.

Xiao, S. G.; Yang, X. M.; Park, S. J.; Weller, D.; Russell, T. P. *Adv Mater* **2009**, *21*, 2516–2519.

Xu, J.; Hong, S. W.; Gu, W.; Lee, K. Y.; Kuo, D. S.; Xiao, S.; Russell, T. P. *Adv Mater* **2011**, *23*, 5755–5761.

Xu, T.; Stevens, J.; Villa, J. A.; Goldbach, J. T.; Guarini, K. W.; Black, C. T.; Hawker, C. J.; Russell, T. P. *Advanced Functional Materials* **2003**, *13*, 698–702.

Yang, J. K. W.; Jung, Y. S.; Chang, J.-B.; Mickiewicz, R. A.; Alexander Katz, A.; Ross, C. A.; Berggren, K. K. *Nat. Nanotechnol.* **2010**, *5*, 256–260.

Yang, S. Y.; Ryu, I.; Kim, H. Y.; Kim, J. K.; Jang, S. K.; Russell, T. P. *Adv Mater* **2006**, *18*, 709–712.

Yokoyama, H.; Kramer, E. J. *Macromolecules* **1998**, *31*, 7871–7876.

Zalusky, A. S.; Olayo-Valles, R.; Wolf, J. H.; Hillmyer, M. A. *J. Am. Chem. Soc.* **2002**, *124*, 12761–12773.

Zhao, Y.; Sivaniah, E.; Hashimoto, T. *Macromolecules* **2008**, *41*, 9948–9951.